CO_2 SEQUESTRATION IN THE PERMIAN BASIN: EXAMINATION OF ABOVE-GROUND MINERALIZATION AND SUBSURFACE SOLUBILITY TRAPPING CAPACITIES AND EVALUATION OF DAWSONITE KINETICS IN GEOLOGIC SEQUESTRATION

by

Aaron Paul Abel

Submitted in Partial Fulfillment of

the Requirements for the Degree of

Master of Science in Hydrology

New Mexico Institute of Mining and Technology

Socorro, New Mexico

September 2007

ABSTRACT

Anthropogenic CO_2 emissions are widely proposed as a cause of global-scale temperature increases, leading to extensive research efforts on the mitigation of anthropogenic CO_2 emissions through a variety of carbon sequestration options.

The purpose of this study was designed to evaluate two different carbon sequestration options. Sequestration of CO_2 through biomimetically increasing the hydration rate of CO_2 to accelerate the formation of solid carbonate has already been tested and proven (summarized by Bond, Abel and others). Solid carbonate minerals effectively sequester CO_2 indefinitely, but formation of these minerals requires a source of cations, such as seawater or waste brines. Produced waters from the oil and gas industry have been proposed as one possible cation source in this sequestration option that we call "surface mineralization". Additionally, direct subsurface injection of bicarbonate-rich waters (by-product of surface mineralization) was considered. Carbon sequestration capacities were estimated for both the formation of solid carbonate with cations from produced waters (surface mineralization) and the storage of CO_2 in dissolved form within produced waters ("solubility trapping") for a study area comprising the Permian Basin of west Texas and southeastern New Mexico.

Results of the capacity study indicate that cations from produced waters in the Permian Basin could be used to sequester approximately 57 percent (2.97 million metric

tons (Mt) of CO_2) of the Permian Basin's regional CO_2 production (total CO_2 emission of 5.19 Mt), or ~ 20 percent of the total production from the Permian and San Juan Basins combined (15.5 Mt), in the form of solid carbonate minerals. Storage of CO_2 in dissolved form ("solubility trapping") within produced waters provides for a vast amount of CO_2 storage (approximately 30 Mt); however, the total inorganic carbon already present within produced waters significantly decreases the additional sequestration capacity by approximately 200 fold (0.157 Mt of CO_2).

Direct injection of supercritical CO_2 in the Permian Basin provides for a vast storage potential; however, this method may cause significant physio-chemical effects in the reservoir, potentially affecting long-term sequestration capacities as well as short-term engineering operations.

Mineralization reactions in the "fringe" of CO_2 plumes may cause significant changes to porosity and permeability of rock strata, and hence to ultimate CO_2 migration. We hypothesize that mineralization of the plume fringe, specifically that associated with dawsonite formation, may restrict plume migration, and that flow rates, chemical kinetic relationships, and other conditions will determine whether the CO_2 plume will be slowed in its migration or even trapped in place by such mineralization at its fringe.

To test these hypotheses, we studied an ongoing pilot CO_2 injection test (West Pearl Queen Reservoir Pilot Test). Two-dimensional numerical models of CO_2 flow and transport were designed to evaluate possible residence times of separate-phase CO_2 in the injection test. Geochemical simulations of brine-rock interactions have been used to examine mineralization and dissolution effects on the reservoir and adjacent formations.

Results of reactive transport (TRANS) and reaction path modeling (Geochemists Workbench™) of supercritical CO_2 injection into the West Pearl Queen Reservoir indicate an overall dissolution-dominated system with a gradual increase of porosity over the model domain at the CO_2 injection point. A complex system of dissolution and precipitation reactions occur over the model domain with the aluminum carbonate mineral dawsonite providing an important carbon sink associated with feldspar-rich reservoir types. Increases in dawsonite volume fraction of 0.14 over the entire model domain occur over a period of approximately 40,000 years, while the pre-existing minerals anhydrite, albite, potassium feldspar, and dolomite completely dissolve over the same simulation time. In simulations of injected supercritical CO_2, porosity decreases approximately 4 percent from the initial value (0.146 to 0.105) in the target reservoir over ~40,000 years. However, timing of initiation of dawsonite precipitation and associated porosity reduction can not be constrained due to inconsistencies of published mineral kinetic rate constants of the aluminum-providing feldspar minerals. Literature values of kinetic rate constants for aluminosilicate minerals such as potassium feldspar ($KAlSi_3O_8$) and albite ($NaAlSi_3O_8$) vary over 3 to 4 orders of magnitude (e.g. between 1.0×10^{-17} and 1.62×10^{-13} mole/cm^2-seconds for $KAlSi_3O_8$ and between 1.0×10^{-16} and 3.63×10^{-13} mole/cm^2-seconds for $NaAlSi_3O_8$). The range in these kinetic rate constants leads to a range of values for dawsonite precipitation timing from less than 2 years up to approximately 12,000 years in the present study greatly influencing the ultimate fate and transport of CO_2 within the system.

PREFACE

Due to the increasing human population in the world and the continued dependence upon carbon-based energy, carbon dioxide emissions have increased greatly since the onset of the industrial revolution. It is widely accepted throughout the scientific world that anthropogenic CO_2 emissions are directly affecting the global climate. Global average air temperature near the Earth's surface rose 0.74 +/- 0.18 ^{o}C (1.3 +/- 0.32 ^{o}F) during the last century (Brohan et al., 2006). Global models of temperature change referenced by the Intergovernmental Panel on Climate Change (IPCC) predict that global average air temperatures are likely to increase by 1.1 to 6.4 ^{o}C (2.0 to 11.5 ^{o}F) between 1990 and 2100 (IPCC, 2007). An increase in global mean air temperatures will in turn cause other changes including: potential sea level rise due to permafrost, glacial, and ice cap melting; increase in the frequency and intensity of extreme weather events; reduction in agricultural yields due to changes in the amount and pattern of precipitation; and possible species extinction due to ecosystem destruction. Based on large remaining fossil fuel reserves and continued economic development of the world, measures must be implemented to curb anthropogenic CO_2 emissions. Carbon dioxide sequestration methods, whereby CO_2 is set apart from the atmosphere and effectively stored in various carbon sinks, has been a part of many interdisciplinary engineering and geological

research programs over the past ten to fifteen years and is the focus of the current research study.

The primary objective of this study was to determine the effects of two different geologic CO_2 sequestration methods (separate-phase injection of CO_2 versus injection of bicarbonate-rich brine) on the subsurface environment and to provide a template for the selection of future geologic sequestration sites. General physical and chemical changes induced by subsurface CO_2 sequestration were examined. Ultimate effects on reservoir hydrodynamics, storage potential, and mineralization and dissolution processes were studied. The West Pearl Queen micro-pilot injection study located in southeast New Mexico is the site of a case study to examine these effects as a result of the geologic sequestration of CO_2. Research collaborators from New Mexico Tech, Los Alamos National Labs and Sandia National Labs have been involved in this ongoing micro-pilot injection study (Westrich et al., 2002, Krumhansl et al., 2002). Additionally, capacities for the following carbon sequestration options were considered in a carbon-capacity case study: (1) solid carbonate formed with cations from produced waters (surface mineralization); and (2) storage of CO_2 in dissolved form within produced waters ("solubility trapping") within the Permian Basin of west Texas and southeastern New Mexico.

Major objectives of this study include:

- Design and implementation of a case-study analysis of carbon sequestration capacity comparing two sequestration techniques: biomimetically enhanced carbonate precipitation and dissolved CO_2 capacity ("solubility trapping") with direct injection of supercritical CO_2
- Development and parameterization of field-scale simulations of an actual CO_2 pilot injection test

- Formulation of a numerical sensitivity study based on a pilot CO_2 injection test to examine residence times for separate-phase CO_2
- Design and testing of a high-temperature, high-pressure core flooding system to examine short-term reactivity in CO_2 core floods
- Evaluation of reaction paths and ultimate reservoir fate due to mineralization and dissolution reactions induced by bicarbonate-rich brine injection and separate-phase CO_2 injection
- Examination of CO_2 plume trapping through mineralization reactions applied to the West Pearl Queen Reservoir pilot injection
- Investigation of the controlling kinetic and thermodynamic factors concerning dawsonite formation

Objectives were based on the overall study objective to delineate effects on reservoirs induced by subsurface injection of carbon-bearing fluids to mitigate CO_2 emissions within the atmosphere.

Due to the breadth of research conducted within this study, this thesis contains three dominant objectives of the overall study. Research design and results of the carbon sequestration capacity analysis of the Permian Basin of west Texas and southeast New Mexico, the evaluation of reaction paths and ultimate reservoir fate due to reactive processes induced by carbon-bearing fluids, and the examination of CO_2 plume trapping through mineralization reactions applied to the West Pearl Queen Reservoir pilot injection study are included in this thesis.

TABLE OF CONTENTS

LIST OF FIGURES

LIST OF TABLES

Table **Page**

This thesis is accepted on behalf of the
Faculty of the Institute by the following committee:

John L Wilson - Academic Advisor
Advisor

Brian McPherson - RESEARCH ADVISOR

- Research advisor

- Committee Member

Peter Lichtner - Committee Member

- committee Member

Date 9/7/2007

I release this document to the New Mexico Institute of Mining and Technology.

Student's Signature 9/07/07
Date

CHAPTER 1:

INTRODUCTION

Due to increasing evidence that greenhouse gas emissions are linked to currently rising global temperatures, it seems vital that measures be taken to reduce greenhouse gas emissions and develop new technologies and methods to sequester these gases. The primary objective of this study was to evaluate potential carbon sequestration capacities of both above-ground and subsurface mineralization processes. An above-ground carbon mineralization approach (summarized by Bond et al., 1999 and 2001) was considered in the context of a specific region, the Permian Basin of southeast New Mexico and west Texas. Potential carbon sequestration in solid form (as calcium and magnesium carbonates) was estimated, based on produced waters as the source of divalent calcium and magnesium ions.

Physical and chemical changes induced by subsurface supercritical CO_2 injection were studied. Ultimate effects on reservoir hydrodynamics, storage potential, and, specifically, mineralization and dissolution processes were considered. Significant physical and chemical changes may be induced by subsurface injection of any fluid that differs from the resident formation fluid. With regard to the sequestration strategy of supercritical CO_2 injection into depleted oil and gas reservoirs or deep saline aquifers, it is apparent that chemical disequilibrium is an important factor in the evolution of geologic media. Brine in the vicinity of the supercritical CO_2 plume will become

enriched with dissolved CO_2(aq), which may promote various chemical reactions with reservoir minerals. Experimental and model results suggested that rock porosity and permeability would be subject to significant dissolution and/or mineralization effects that can lead to changes in reservoir hydrodynamics. Timing of mineralization and dissolution reactions, as well as the rates of these reactions, are of particular importance for prediction of ultimate plume migration and sequestration.

The Permian Basin of southeast New Mexico and west Texas provides an ideal setting to research and implement various carbon sequestration technologies. Active enhanced oil recovery (EOR) technologies, including CO_2 floods, have operated within the Permian Basin for the past 30 years, providing infrastructure for sequestration testing. Additionally, a vast amount of geologic and geochemical data associated with oil and gas production has been compiled by private industry, state regulatory entities, and research institutions. Because of these advantages, the Permian Basin was selected for a CO_2 sequestration capacity analysis for the novel biomimetic carbonate mineralization technique ("above-ground mineralization").

1.1 PURPOSE

The purpose of this study was three-fold: 1) To investigate potential carbon sequestration capacities of both above-ground and subsurface mineralization processes previously developed (Bond et al., 1999 and 2001) and apply these processes to a case study of the Permian Basin of southeast New Mexico and west Texas, 2) to study reactive processes specific to a CO_2 pilot injection test within a depleted oil and gas reservoir in the Permian Basin, 3) to investigate implications of reservoir property alterations (i.e. changes in porosity and permeability) due to identified reactive processes

and the effects on ultimate CO_2 plume transport.

1.2 HYPOTHESES

This study is based on two major hypotheses. First, we hypothesized that, a process we call "Plume Fringe Mineralization" (PFM) will follow subsurface injection of CO_2 for sequestration. We have defined "Plume Fringe Mineralization" as mineralization that occurs at the boundary between the separate-phase CO_2 plume and resident groundwater where waters are enriched with dissolved CO_2. In these regions of CO_2-enriched waters, minerals such as magnesite, siderite, ankerite, and dawsonite may have the opportunity to form or dissolve if certain geochemical conditions (major cation/anion activities, pH conditions, resident mineralogies) exist. If conditions allow for intense mineralization, then pores will be filled, flow rates will drop, and CO_2 will be stored by a "self-trapping" mechanism. In the opposite end-member case, CO_2-rich waters will dissolve minerals and increase porosity in the fringe region, allowing for enhanced migration of supercritical CO_2 upward into shallower localities. Flow rates, chemical kinetic relationships, reservoir heterogeneity and other conditions will determine whether a CO_2 plume will migrate or be trapped in place by PFM. Within this study we specifically targeted the hydrated sodium aluminum carbonate mineral kinetics of dawsonite ($NAlCO_3(OH)_2$) and the controlling factors of the formation of dawsonite.

The second major hypothesis of this study is that risk-free sequestration by mineralization may be achieved above ground by combining CO_2 with required cations supplied by brines, such as produced waters. The carbon capacity of such above-ground mineralization is dependent upon the divalent cation concentrations of basin brines, the magnitude of ionic strengths in these brines, and the volume of brine produced.

1.3 OBJECTIVES AND TASKS

The first major objective of this study was to examine and compare above-ground mineralization capacities to dissolved CO_2 capacities in subsurface waters, with the Permian Basin as a case study. Based on Permian Basin brine composition and volume data from waters produced with oil and gas, a significant amount of carbon may be stored as carbonate minerals above ground. A secondary carbon sink within this above-ground sequestration option is the storage of CO_2 in aqueous (dissolved) form. Approximately 90 percent of all water produced in the Permian Basin is re-injected into subsurface oil and gas reservoirs or adjacent formations; if these waters are saturated with CO_2 prior to re-injection, a significant amount of CO_2 may be trapped This method of sequestration is known as "solubility trapping." However, this form of sequestration as a by-product of above-ground mineralization provides only a small increase in carbon storage potential. It is important, nevertheless, in order to realize the full sequestration potential of above-ground mineralization, because it provides carbonic species of anthropogenic origin to replace those that were already present in the brines but accounted for part of the precipitated carbonate.

The second major objective was to analyze and quantify reactive processes, especially PFM, associated with direct injection of supercritical CO_2 in a typical sandstone reservoir. Kinetic reaction path modeling and reactive transport modeling techniques were used to examine possible changes in porosity and permeability of the reservoir. Two major tasks were carried out in order to achieve this objective.

The first task included development of geochemical models for evaluation of reaction paths and ultimate reservoir fate due to mineralization and dissolution reactions.

A depleted oil and gas reservoir (southeastern New Mexico West Pearl Queen Reservoir, Shattuck Sandstone Member) undergoing a CO_2 pilot injection study was selected as a representative case example for study. Reservoir mineralogy, brine composition, and supercritical CO_2 injection rates for the West Pearl Queen Reservoir were available through previous and ongoing sequestration research projects at Los Alamos and Sandia National Laboratories. Equilibrium dissolved CO_2 concentrations in brine were calculated based on reservoir thermodynamic conditions (temperature and pressure). Hydrogeochemical kinetic reaction path simulations were designed with dissolved CO_2 concentrations and reservoir mineralogy.

A low-flow reservoir was assumed, with cases of local thermodynamic and chemical equilibrium. Results of these kinetic reaction path and reactive transport simulations indicated marked changes in brine chemistry and reservoir mineralogy. Precipitation of the hydroxyl-aluminum carbonate mineral, dawsonite, greatly influenced porosity within the CO_2 plume fringe. However, dawsonite precipitation timing could not be constrained due to inconsistencies among published values of mineral kinetic rate constants. Furthermore, uncertainties in mineral surface areas provide additional uncertainties in determining absolute precipitation times.

The second major task involved examination of CO_2 plume trapping through PFM, specifically in the context of arkosic sandstone reservoirs. The origin, thermodynamic stability, and likely natural settings of dawsonite were examined. Results of this analysis indicated several possible reservoir settings that promote long separate-phase CO_2 residence times and CO_2 plume trapping. Naturally dawsonite-prone reservoirs include low-temperature (typically less than 130°C) reservoirs with sources of

CO_2.

Common reservoirs of this type include deep magmatic or hydrocarbon-rich sources of CO_2.

Finally, kinetic reaction rate discrepancies among aluminum silicate minerals and dawsonite were investigated. A major goal was to determine the controlling factors for dawsonite formation and to evaluate the need for additional kinetic reaction rate experiments specifically associated with dawsonite.

1.4 IMPLICATIONS

The results of these studies will provide useful information to those who set carbon sequestration policy, as privatized companies and governments continue to move closer to widespread commercial implementation of sequestration. Results from reaction path and reactive transport modeling may be used to predict reservoir reactivity when direct injection of supercritical CO_2 is used as a sequestration technique. The ability to predict reactive processes induced by supercritical CO_2 injection will greatly assist in the selection and design of both pilot tests and commercial-scale deployment of geologic CO_2 sequestration. Prediction of porosity and permeability from reactive transport models can also be used in applications for the oil and gas industry. Preferential permeability control is widely used in enhanced oil recovery (EOR). Depending on mineralization time scales, it may be possible to control permeability through supercritical CO_2 injection in such applications. Environmental risks may also be evaluated through modeling of the continual feedback loop between chemical and physical in the target reservoir and associated seal layers. The evaluation of possible environmental outcomes, such as pH depression in shallower aquifers (Underground

Source of Drinking Water (USDW)), is also of vital importance in carbon-sequestration risk-analysis modeling.

The prediction of specific mineralization zones in sequestration pilot reservoirs may provide information on diagenetic conditions for certain pore-filling minerals. Research on natural analogues for CO_2 injection, such as natural CO_2 reservoirs (e.g., Springerville and Bravo Dome), will benefit from reaction path modeling results. The storage capacity information that was generated in this research may be useful to companies or cooperatives that are making decisions on carbon management, from sequestration to offsets by carbon credits.

CHAPTER 2:

SEQUESTRATION CAPACITY ANALYSES

This study focused on both the geologic sequestration and enhanced mineralization of CO_2 emissions from anthropogenic sources, specifically from electric power plants. Before the details of carbon sequestration are discussed, it is important to understand the background to sequestration, in terms of anthropogenic CO_2 emissions and global warming.

2.1 GLOBAL WARMING AND ANTHROPOGENIC GREENHOUSE GASES

It is widely accepted that CO_2 is a major contributor to the current rise in the mean global temperature. What is more interesting is the amount of CO_2 that is emitted by human activities. Figure 2-1-1 depicts the increase in total global CO_2 emissions from fossil fuels in a time series plot from the year 1750 until the year 2002, and the increase in atmospheric CO_2 concentration in parts per million (ppm_v) through the same time series (Keeling and Whorf, 2003). At the onset of the industrial revolution (~1850), emissions due to fossil fuels were very low and essentially constant. As the need for energy increased, so did emissions from the combustion of fossil fuels.

Over the last century, both CO_2 emissions and atmospheric CO_2 concentrations have increased at an exponential rate.

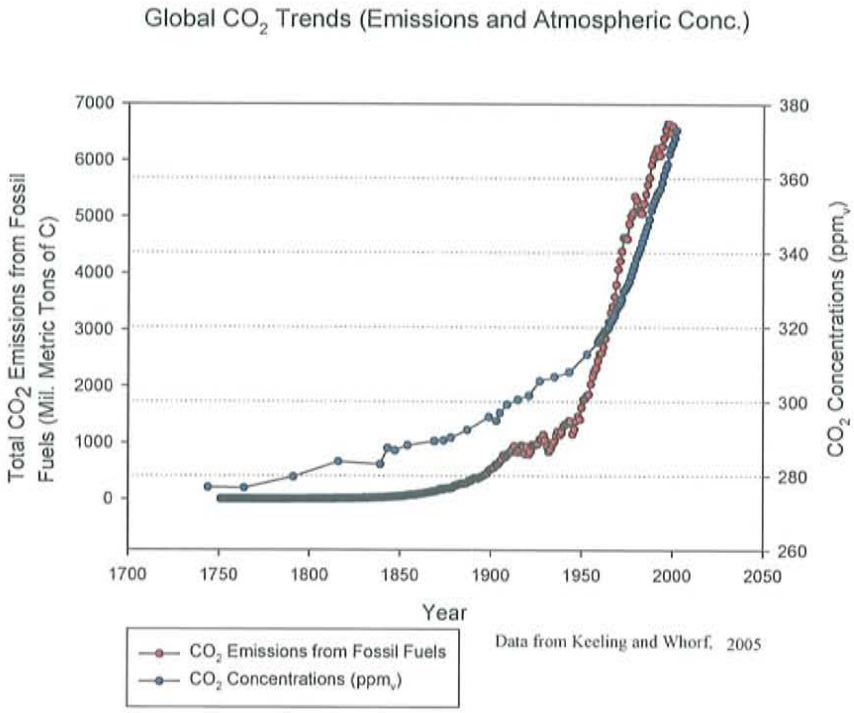

Figure 2-1-1: Total CO_2 emissions from fossil fuels in relation to atmospheric CO_2 concentrations (ppm_v) derived from in-situ air samples collected at Mauna Loa Observatory, Hawaii, and ice core data.

Another important relationship in this system is the strong correlation between atmospheric CO_2 concentration and the change in the mean global temperature (Global Temperature Anomaly, Jones and Moberg, 2003). Figure 2-1-2 illustrates the correlation between the rise in the atmospheric concentration of CO_2 (ppm_v) and that of the global temperature anomaly. All global temperature anomalies were calculated with the mean global temperature between 1961 and 1990 as the standard. It is likely that the rise in CO_2 concentrations within the atmosphere is a contributing factor to the rise in global temperatures.

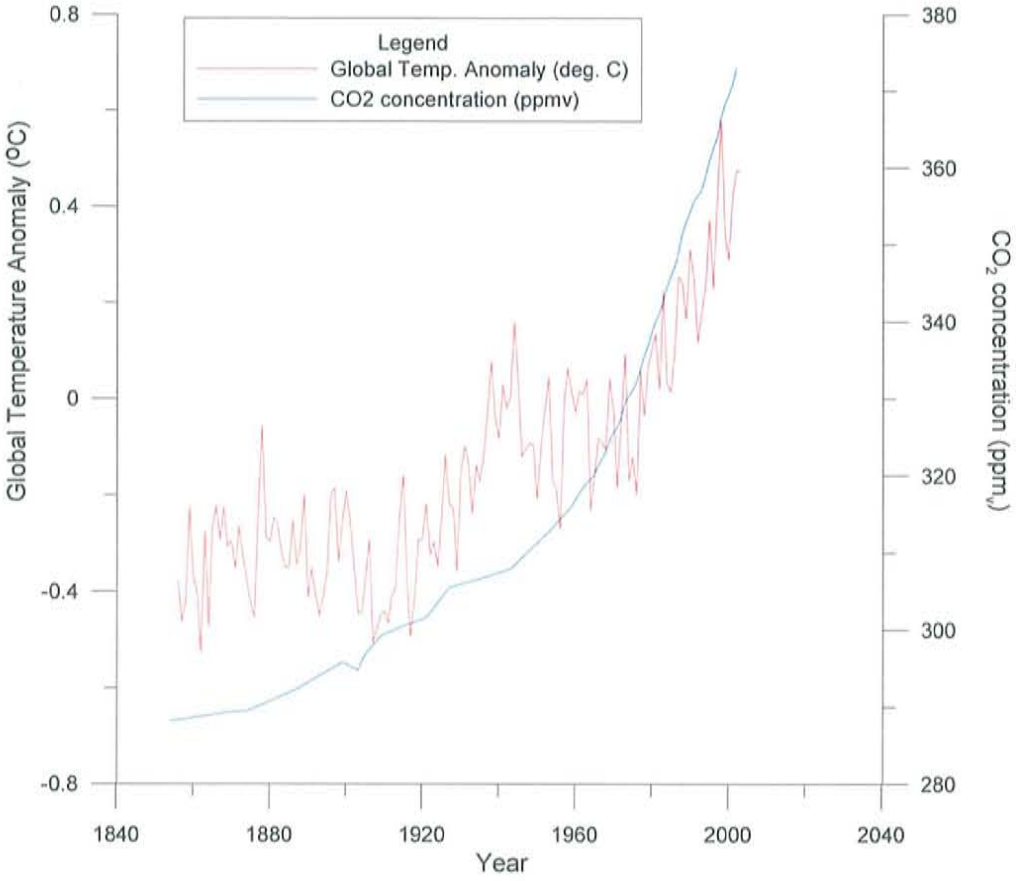

Figure 2-1-2: Global temperature anomaly (^{0}C) correlated to global CO_2 concentrations in ppm_v. Temperature data from Jones and Moberg, 2003.

It is also apparent that the proportion of CO_2 due to the combustion of fossil fuels is quite substantial. The human population is heavily dependent on fossil fuels as a source of energy, and a large-scale transition to alternative renewable energy sources is unlikely in the immediate future. It is interesting to note the rankings of the major carbon emitters throughout the world, shown in Table 2-1-1.

WORLD CARBON EMISSIONS BY REGION, Reference Case (Millions of Metric Tons of Carbon)

	HISTORY		PROJECTIONS		PERCENT CHANGE
REGION/COUNTRY	**1990**	**2001**	**2010**	**2020**	**1990-2020**
United States	1,352	1,559	1,800	2,082	54.00%
Former Soviet Union	1,036	654	825	939	-9.40%
China*	617	832	1,109	1,574	155.00%
Eastern Europe	301	202	213	248	-17.60%
Germany	271	233	232	241	-11.00%
Japan	269	316	334	365	35.70%
United Kingdom	164	153	163	176	7.30%
India	153	250	321	435	184.00%
Canada	129	155	186	196	52.00%
France	102	108	108	122	19.60%
Mexico	84	96	134	207	146.00%
Brazil	68	95	127	180	165.00%
South Korea	64	121	156	193	202.00%
TOTAL DEVELOPING	**1,691**	**2,487**	**3,075**	**4,137**	**145.00%**
TOTAL WORLD	**5,872**	**6,522**	**7,685**	**9,372**	**59.60%**

Source: Based on U.S. Energy Information Administration, International Energy Outlook 2003, p. 191
Note: *According to the Netherlands Environmental Assessment Agency, China's 2006 CO_2 emissions surpassed the United State's by 8 percent (http://www.mnp.nl/en/dossiers/Climatechange/moreinfo/Chinanowno1inCO2emissionsUSAinsecondposition.html, 2007)

Table 2-1-1: World carbon emissions designated by region including both historical data and projections.

The United States is the most prolific contributor of CO_2 emissions to the atmosphere, followed by other industrialized countries such as the former Soviet Union and China. The fifteen-year projections of the above reference case illustrate alarming increases in carbon emissions, especially in the developing economies of India, Mexico, Brazil, and South Korea.

With the continual increase in global population and the corresponding need for additional electricity production, methods to sequester CO_2 effectively are urgently needed.

Sequestration of CO_2 is likely to be implemented most readily for large stationary sources, such as electric power plants and large-scale industrial process plants. Figure 2-1-3 depicts projected CO_2 emissions (millions of metric tons of carbon equivalent) from coal-fired electric power plants located within the United States (United States Energy Information Administration, 2006).

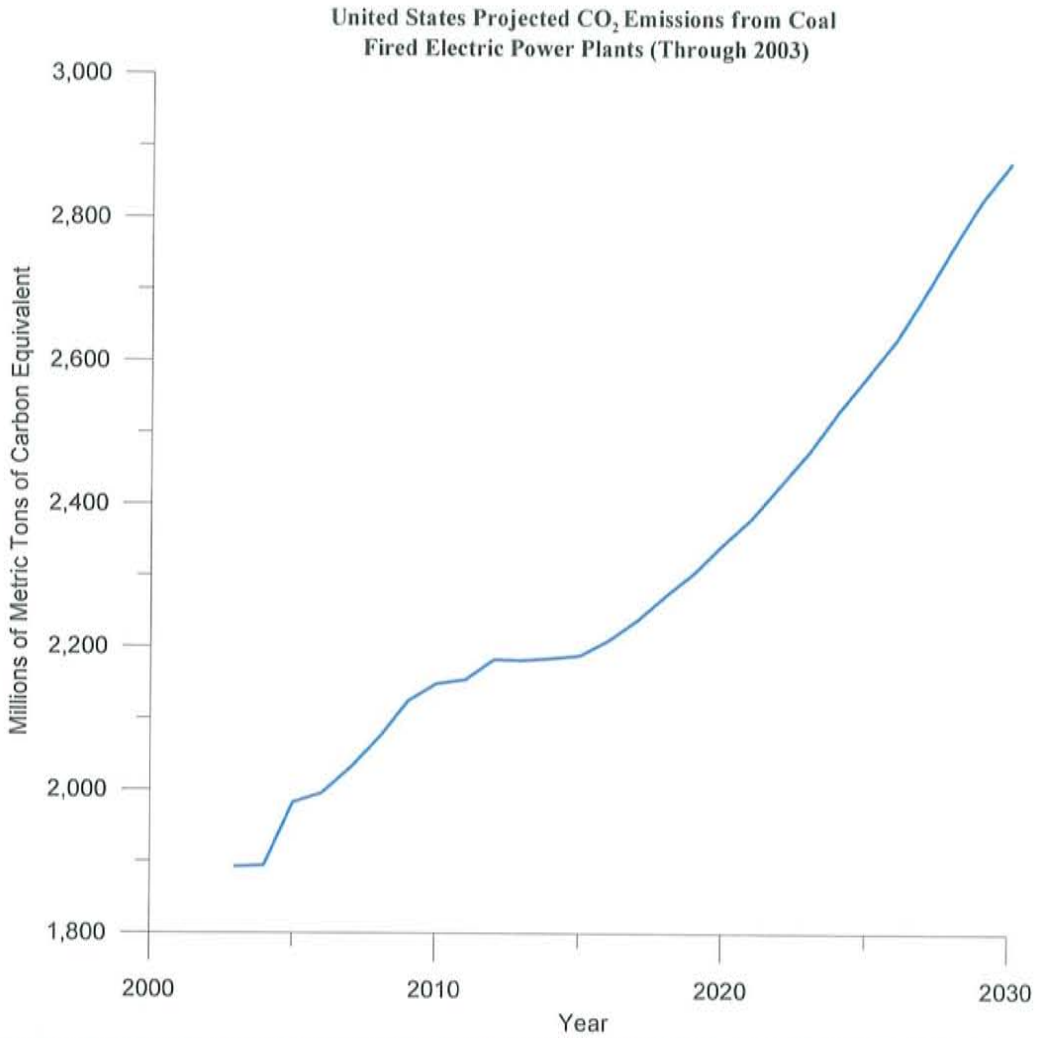

Figure 2-1-3: Projected United States CO_2 emissions associated with coal-fired power plants (United States Energy Information Administration, 2006).

Separation technology has been developed to remove CO_2 from natural gas, but is prohibitively expensive on the scale needed to remove CO_2 from the flue gases from power plants. Extensive research has progressed in the past ten years both to reduce CO_2 removal costs and to develop sequestration technologies.

2.2 OBJECTIVE

Currently, research on many methods of carbon sequestration is growing, including ocean sequestration, enhancement of the natural terrestrial cycle, and mineralization (Bond et al., 2001, Benner et al., 2001, Guthrie et al., 2000). The main focus of this research concerns three different approaches to the sequestration of carbon: (1) sequestration via mineralization above ground, (2) geologic sequestration of bicarbonate-rich brine, and (3) geologic sequestration of supercritical CO_2. Above-ground mineralization of solid carbonates provides an extremely secure storage method for CO_2. To obtain solid carbonates, two main conditions must apply: (1) carbonate ions must persist, and (2) a source of counter-ions or cations must be available. One method to provide carbonate ions is the utilization of CO_2 gas from the waste streams of electric power plants. Conversion of the CO_2 gas into an aqueous carbonate solution is possible in the presence of a suitable source of cations, if reaction rates are increased and pH is controlled. Bond and coworkers at NMT have developed a novel biomimetic procedure to enhance the hydration kinetics of gaseous CO_2 (Bond et al., 1999, 2001).

Biomimetics is an interdisciplinary field that combines biology, biochemistry, inorganic chemistry, and materials science. The premise behind any biomimetic technique is to use a natural biological system as a model to develop synthetic systems. Examples of such model systems include photosynthesis and biomineralization. Many

examples of biomimetic techniques can be found, for example, in the food and brewing industry. In the context of sequestration, use of cations from suitable sources, coupled with biomimetically enhanced hydration of CO_2, gives the opportunity to precipitate solid carbonate (Bond et al., 1999, 2001, Liu et al., 2005). Suitable cation sources include produced waters, for which representative compositions have been identified and precipitation studies have been performed (Bond et al., 2002, Liu et al., 2005).

Other possibilities for carbon sequestration include subsurface injection of bicarbonate-rich water. Evaluation of chemical and physical processes that occur within the target reservoir as a result of bicarbonate-rich water injection must be examined. Long-term injection could potentially cause engineering problems if reservoirs show increased dissolution or mineralization. Carbon storage potential must also be assessed for the selection of suitable sites.

The amount of CO_2 that can be stored in a given reservoir or mineralized through a specific mineralization technique is called the "sequestration capacity." In this study we have evaluated CO_2 sequestration capacities of geologic sequestration via direct injection of separate-phase CO_2, above-ground mineralization of solid-form carbonate minerals with produced waters as a counter-ion source, and subsurface solubility trapping (dissolved CO_2 trapped in re-injected produced waters).

2.3 PREMISE

Throughout the millennia, the earth has undergone various glacial and interglacial episodes. During interglacial episodes the earth's atmosphere becomes inundated with global greenhouse gases (GHGs), mainly CO_2, while glacial periods represent periods of relatively low atmospheric CO_2 concentrations. During transition periods from

interglacial to glacial periods, the carbon cycle of the earth must invert from relatively low carbon storage to high carbon storage. Inspection of the geologic record reveals interglacial periods as being dominated by carbonate-rich minerals such as carbonate muds and limestones. These types of minerals have survived unchanged throughout geologic time, and are still forming today with the building of reefs throughout the world. The main process behind the formation of carbonate sediments is biomineralization.

The premise behind Dr. Gillian Bond's biomimetic technique is to mimic natural biomineralization to produce solid carbonate with the CO_2 produced by electric power plants as the source of carbon. Inspection of the equilibria and kinetic chemistry of the carbonic species shows the necessary steps to form carbonate ions (from which to form solid carbonate) from CO_2 gas. This chemistry can be described with the following equations.

$$CO_{2(g)} \rightleftharpoons CO_{2(aq)} \quad K_H = 10^{-3.02} \quad (P = 1\ bar,\ T = 25^{o}C) \qquad \text{Eq. 2-3-1}$$

In this gas dissolution reaction, gaseous CO_2 forms aqueous CO_2, which associates with water molecules to form carbonic acid, H_2CO_3. Even though $CO_{2(aq)}$ is approximately 250 times more abundant than H_2CO_3, it is convenient to represent CO_2 in solution in terms of its hydration (Appelo and Postma, 1993):

$$(1)\ CO_{2(aq)} + H_2O \rightleftharpoons H_2CO_3 \qquad \text{Eq. 2-3-2}$$

H_2CO_3 or carbonic acid then dissociates in water to produce first bicarbonate ions, HCO_3^-, and then carbonate ions, CO_3^{2-}.

$$(2)\ H_2CO_3 \rightleftharpoons H^+ + HCO_3^- \quad K_1 = 10^{-6.3} \qquad \text{Eq. 2-3-3}$$

(3) $HCO_3^- \rightleftharpoons H^+ + CO_3^{2-}\ K_1 = 10^{-10.3}$ Eq. 2-3-4

Once carbonate ions predominate in the solution and suitable counter-ions are present, such as calcium or magnesium, solid carbonate minerals such as calcite and magnesite can readily be formed. The fundamental limiting factor in this precipitation process is the reaction rates for these reactions. The dissolution of gaseous CO_2 to form aqueous CO_2 is regarded as a rapid reaction (Keene, 1993). The hydration of aqueous CO_2 (reaction 1) is the rate-limiting step within this series of reaction steps. This hydration step is slow compared to most other reactions. The rate constant of the hydration of H_2CO_3 is approximately 10^4 kg mol^{-1} s^{-1}, whereas diffusion-controlled reaction rate constants are on the order of 10^{10} kg mol^{-1} s^{-1}, (Keene, 1993). Subsequent dissociation reactions of carbonic acid into bicarbonate ions (reaction 2) and of bicarbonate ions into carbonate ions (reaction 3) are diffusion-controlled. The term "diffusion controlled" denotes that the reaction is controlled by the rates at which the reactants are supplied to, and the products are taken away from, the reaction area. Aqueous CO_2 will also react with hydroxyl ions if solution pH is high.

(4) $H_2CO_3 + OH^- \rightleftharpoons HCO_3^- + H_2O$ Eq. 2-3-5

In solutions of pH less than ~8.0, reaction 4 is negligible due to lack of hydroxyl ions in solution. Between pH values of ~8.0 and 10.0, bicarbonate ions are formed both by a combination of reactions 2 and 3 and by reaction 4. In solution pH greater than 10.0, reaction 4 dominates; hence, one could produce bicarbonate ions by increasing the pH of the solution to induce reaction 4, but this would produce caustic solutions and, possibly, environmental hazards with regulatory consequences.

In solutions at less extreme pH, where the hydration of CO_2 controls the rate at which one can produce carbonate ions, alternative measures, such as biomimetic techniques, are needed to catalyze this reaction step.

The biomimetic technique that Bond and coworkers have devised calls for a zinc metalloenzyme, carbonic anhydrase (CA), to catalyze the hydration of CO_2 in solution. CA is found in practically all living things from animals to algae and bacteria (Bond, 1999, Medina et al., 2000). This enzyme is one of the fastest known, giving near-perfect efficiency in the catalysis process (Stryer, 1988). Each molecule of the carbonic anhydrase isozyme from human erythrocytes, HCA II, can hydrate ~1.0×10^6 molecules of CO_2 per second (Ren and Lindskog, 1992). The speed and efficiency of this enzyme replace the slow hydration reaction of CO_2 (reaction 1) as well as the (much faster) dissociation of carbonic acid to bicarbonate ions (reaction 2) with a single enzyme-facilitated reaction that starts with aqueous CO_2 and water and yields bicarbonate ions and protons. The rate of this enzyme-facilitated reaction approaches the limit of diffusion-controlled transport, whereby the reaction is actually limited by the rates at which unhydrated CO_2 molecules reach the enzyme molecules and bicarbonate ions are removed from the reaction region (Pocker et al, 1977).

A laboratory-scale precipitation reactor was designed and tested at New Mexico Tech, in which a fast bovine carbonic anhydrase (BCA II) is used. Synthetic calcium-rich ($CaCl_2$) brines, as well as brines simulating the natural brines from deep saline reservoirs and produced waters (i.e. West Pearl Queen Reservoir, southeast New Mexico), were used to determine direct carbonate precipitation efficiency (Bond et al., 2004) for the biomimetic method. It was shown that, with this biomimetic method to

accelerate CO_2 hydration, the formation of bicarbonate-rich solutions on the order of 0.01 molal HCO_3^- (West Pearl Queen Reservoir brine solution) is possible (Bond et al., 2004). Two carbon sequestration options have been proposed for these bicarbonate-rich solutions: direct precipitation of carbonate minerals or "above-ground mineralization," and aqueous "solubility trapping" of carbon ($CO_{2(aq)}$, CO_3^{2-}, and HCO_3^-) in solution.

2.3.1 ABOVE-GROUND MINERALIZATION

Above-ground mineralization via biomimetic techniques offers several advantages over geologic sequestration techniques. One of the most fundamental advantages of this technique is that CO_2 gas does not have to be concentrated or transported to injection sites, as required for the most part in geologic sequestration options. Above-ground mineralization techniques would be designed for implementation at a point-source CO_2 emitter, such as a coal-fired power plant. Flue gases from the facility would be used as the carbon source with biomimetic reactors located at the on-site facility or in close proximity. The counter-ion source (brine solution) would be transported to the biomimetic reactor, or oil and/or gas wells supplying brine (production water) as a byproduct would be located close to the biomimetic reactor. An environmentally benign mineralization product (solid carbonate minerals) would then be precipitated on-site, with the remaining brine byproduct being recycled within the loop and finally being disposed of via direct subsurface injection, as with produced water in the oil and gas industry. Licensing and regulatory control for biomimetic above-ground mineralization techniques would likely be minimal in comparison to geologic sequestration options. In addition, it is unlikely that long-term monitoring would be necessary.

One question that arises concerns the costs associated with biomimetic catalysts. HCA II (human carbonic anhydrase II), however, has been successfully produced by bacterial overexpression, which affords the possibility of economic production (Bond et al., 2001). HCA II is the fastest known isozyme of carbonic anhydrase. Furthermore, tests have been performed (Medina et al., 2000), which suggest that it will perform well in actual service conditions. A variety of other enzymes are now produced on an industrial scale at modest cost. The enzymes used in certain detergents, for example, range in price from a little under $1 to around $3 per kg (Bond et al., 2004). Thus, costs associated with the large-scale production of the enzyme catalyst are expected to become more economical, and are not likely to be a barrier to implementation of the approach. Research is presently in progress to develop economical pH control based on the use of existing waste products such as fly ash.

2.3.2 SUBSURFACE SOLUBILITY TRAPPING

Subsurface solubility trapping is defined as the capture ("trapping") of CO_2 in solution by the dissolution of CO_2 into a solution (brine, produced waters, oil, gas, etc.) (Bachu and Adams, 2003). Based on this concept, another option arising from the biomimetic carbon sequestration approach is geologic sequestration of bicarbonate-rich brines in deep saline reservoirs and depleted oil and gas reservoirs.

The capacities of these types of carbon sinks are important to determine based on the above-ground mineralization sequestration method discussed previously. Bicarbonate- and carbonate-rich brine remaining from above-ground mineralization activities described in the previous section also have carbon capacity. This option would be ideal since brine solutions or produced waters are already reinjected for disposal

purposes and for secondary recovery of oil and gas. For instance, approximately 90 percent of the water produced from oil and gas operations within the Permian Basin of west Texas and southeastern New Mexico is injected into producing intervals for secondary recovery (i.e. waterflooding) or for disposal via injection into alternate deep subsurface reservoirs. Injection of bicarbonate-rich produced waters may therefore be ideal in regions such as the Permian Basin, primarily because the infrastructure of production and injection wells is already installed and active.

One attractive feature of this approach to carbon sequestration is that monitoring costs and regulatory certification requirements will again be significantly reduced compared to direct separate-phase CO_2 injection. Another attribute of the injection of bicarbonate-rich brine is that this form of carbon is much less likely either to escape (as CO_2 gas) or to reduce the pH of its environment than either separate-phase CO_2 or the acidic solutions of aqueous CO_2 that form adjacent to a plume of supercritical CO_2. The injection of bicarbonate-rich brine into subsurface reservoirs offers two possible routes to carbon storage: it may lead to permanent carbon sequestration through mineral precipitation within the reservoir, depending on local mineral assemblages and resident brine compositions, or the carbon may remain in solution in the brine. A detailed account of CO_2 solubility and the primary variables affecting CO_2 solubility in produced waters and deep saline aquifers is provided in Section 2.4.3.

2.4 PERMIAN BASIN CASE STUDY

The Permian Basin of western Texas and southeastern New Mexico was selected as an ideal basin in which to conduct a case study to determine conservative capacity

estimates of both above-ground mineralization and subsurface dissolved carbon (as bicarbonate) associated with biomimetic sequestration techniques. The following factors make the Permian Basin an ideal geologic basin for a capacity analysis:

- Large areal extent (approximately 23,000 square miles)
- Diverse geologic units with wide range of reservoir characteristics
- Numerous oil and gas production reservoirs with enhanced oil recovery (EOR) technologies in use
- Extensive infrastructure currently in operation including CO_2 pipelines and several electric-power generation plants

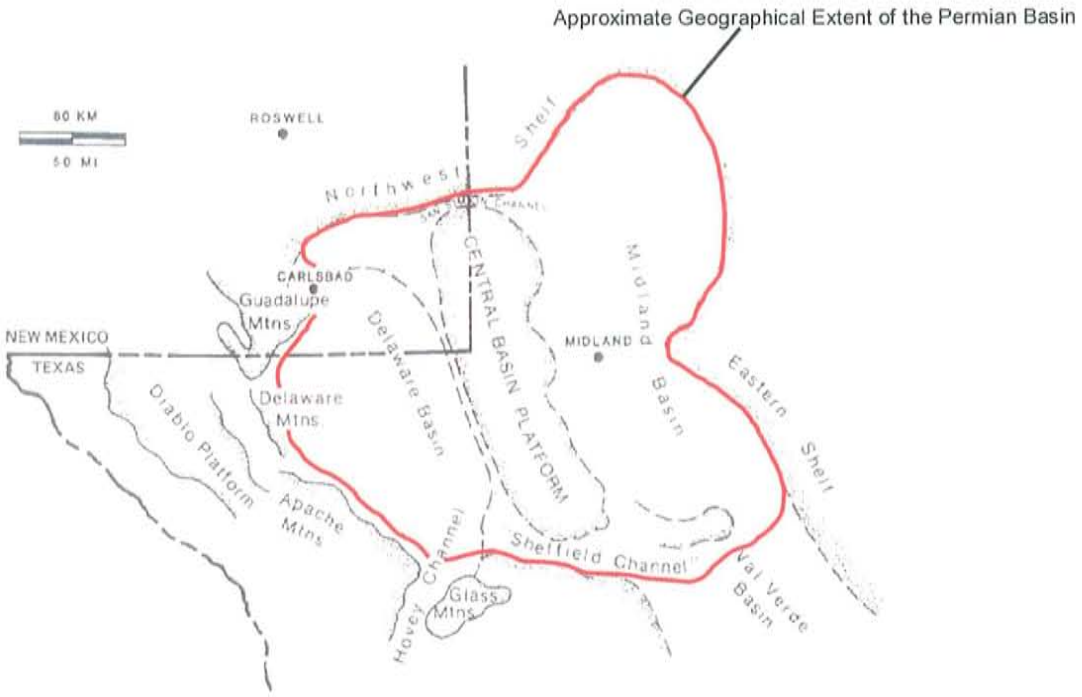

Figure 2-4-1: Geographical extent of the Permian Basin of southeast New Mexico and west Texas. Figure adapted from Ward et al. (1986)

Due to the large oil and gas reservoirs of the Permian Basin, an enormous amount of data associated with EOR operations, production information, and reservoir geology has been compiled by oil and gas producers. The development of CO_2 EOR in the

Permian Basin was actually initiated in 1974 when two of the very first large-scale carbon dioxide injection pilot projects commenced in the basin. Initially, CO_2 EOR projects in the basin utilized CO_2 separated from natural gas that was captured at gas plants, compressed, and sent to project sites via pipelines constructed specifically for delivering CO_2 to EOR pilot sites. After a period of observation and confirmation of the CO_2 EOR process, three new pipelines from three natural CO_2 sources (McElmo Dome, Colorado; Sheep Mountain, Colorado; and Bravo Dome, New Mexico) were initiated in the early 1980s. The construction of CO_2 transfer pipelines resulted in thousands of miles of pipeline infrastructure throughout the basin, and dramatically accelerated the use of CO_2 EOR in the mid-1980s. Today, the Permian Basin has one of the most developed pipeline infrastructures in the world. Figure 2-4-2 below depicts the current CO_2 pipeline infrastructure within the Permian Basin. Currently, approximately twelve major CO_2 pipelines, totaling thousands of pipeline miles, operate within the basin. Additionally, six electric power plants (Harrington, Nichols, Tolk, Holley Avenue, Cunningham, and Maddox) operate within the Permian Basin, or near it.

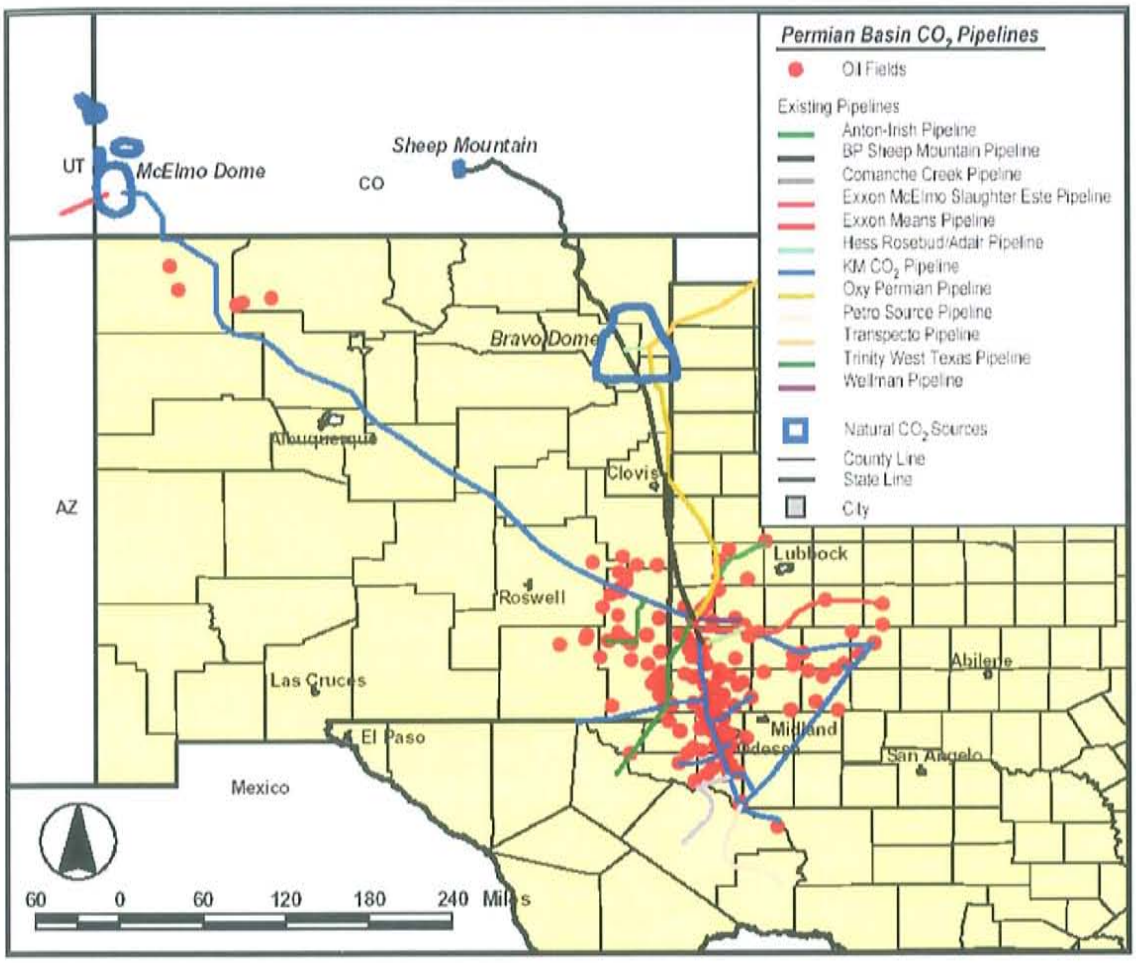

Figure 2-4-2: Permian Basin major CO_2 pipeline map (United States Department of Energy, 2006).

Altogether, these electric power plants emit approximately 5.19 million metric tonnes (Mt) of CO_2 into the atmosphere on an annual basis (Bureau of Economic Geology, 2002).

Based on the in-place infrastructure associated with previous CO_2 EOR projects and the large amount of geologic data associated with oil and gas production within the region over the past 30 years, the Permian Basin provides an excellent setting for a comprehensive case study in CO_2 sequestration capacity analyses.

2.4.1 DATA COLLECTION

Several sources of information were drawn upon to compile needed data to estimate CO_2 capacity associated with above-ground mineralization and subsurface solubility trapping using produced waters of the Permian Basin. Production water databases from the New Mexico Oil Conservation Division (NMOCD), the Petroleum Technology Transfer Council (PTTC) Southwest Region, New Mexico Office of the State Engineer (NMOSE), the United States Geological Survey (USGS), and the Texas Railroad Commission (TRRC) were obtained and screened for applicable data associated with the Permian Basin of southeast New Mexico and west Texas. Data such as oil/gas well location, brine composition (cation/anion concentration, total dissolved solids (TDS), and pH), total depth of well, oil/gas production pool, brine production rate (barrels produced), and secondary reinjection volumes were compiled for the Permian Basin. Total volumes of produced water for both southeast New Mexico and west Texas Permian Basin for 2002 were obtained, as well as the volumes of produced waters reinjected for secondary oil and gas recovery.

More than 17,000 produced water records were obtained for this carbon sequestration capacity study for both southeast New Mexico and west Texas, specific to the Permian Basin.

Figure 2-4-3 depicts plotted oil and gas well locations for the Permian Basin of west Texas and southeast New Mexico, as well as the six electric power plants that operate within the Permian Basin or close by. It should also be noted that three other large CO_2-emitting electric power plants are situated near CO_2 pipeline infrastructure that connect into the Permian Basin CO_2 pipeline network. The San Juan, Four Corners, and

Navajo facilities are three of the largest CO_2-emitting electric power plants in the southwest United States. These facilities are situated relatively near the large natural CO_2 source located in Southwest Colorado (McElmo Dome) and the Kinder Morgan CO_2 pipeline that connects McElmo Dome with the Permian Basin and traverses the state of New Mexico from northwest to southeast. It is reasonably feasible that infrastructure including CO_2 pipelines and pressure lift stations could be installed to connect the CO_2 sources of these three electric power plants into the Permian Basin CO_2-source infrastructure.

Additionally, Figure 2-4-3 depicts the total amounts of produced water generated during 2002 from the oil and gas industry in the Permian Basin of west Texas (approximately 247 billion liters) and the Permian Basin of southeast New Mexico (approximately 70.3 billion liters). A total of approximately 317 billion liters of produced water is generated as part of oil and gas production activities in the Permian Basin.

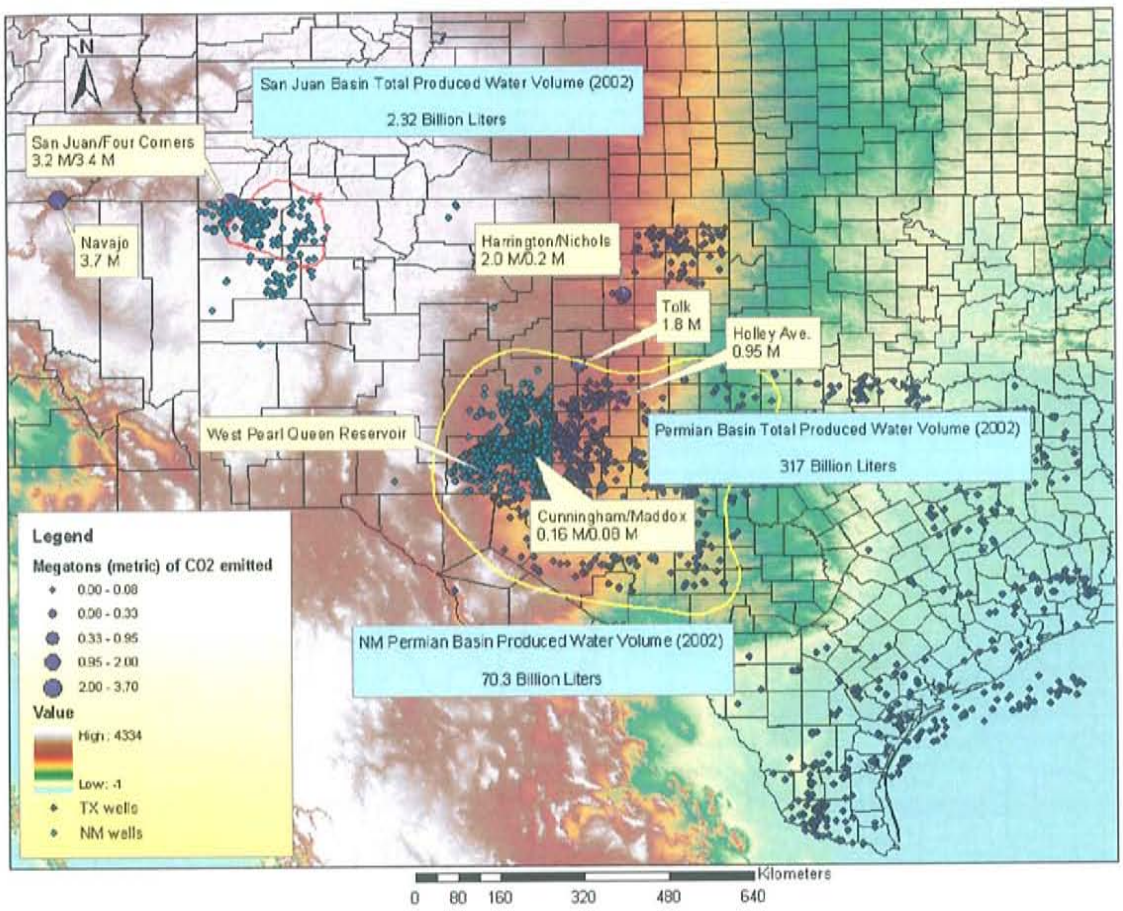

Figure 2-4-3: Permian Basin produced water data (production water volumes) (Bureau of Economic Geology, 2002).

From these produced waters large amounts of dissolved solids in the form of the divalent cations, calcium (Ca^{2+}) and magnesium (Mg^{2+}), could be utilized in the aforementioned biomimetic above-ground mineralization technique to immobilize CO_2 in the form of carbonate minerals (calcium carbonate ($CaCO_3$) and magnesium carbonate ($MgCO_3$)). Based on the analyses of produced water obtained through the available database sources, Figures 2-4-4 and 2-4-5 (below) were generated to depict concentrations of calcium and magnesium ions in the Permian Basin. Calcium concentrations through the Permian Basin range between several mg/L in the far western portions of the basin in New Mexico (Delaware sub-basin) to upwards of approximately

50,000 to 70,000 mg/L in portions of the west-central and north-central Permian Basin (Central Basin Platform).

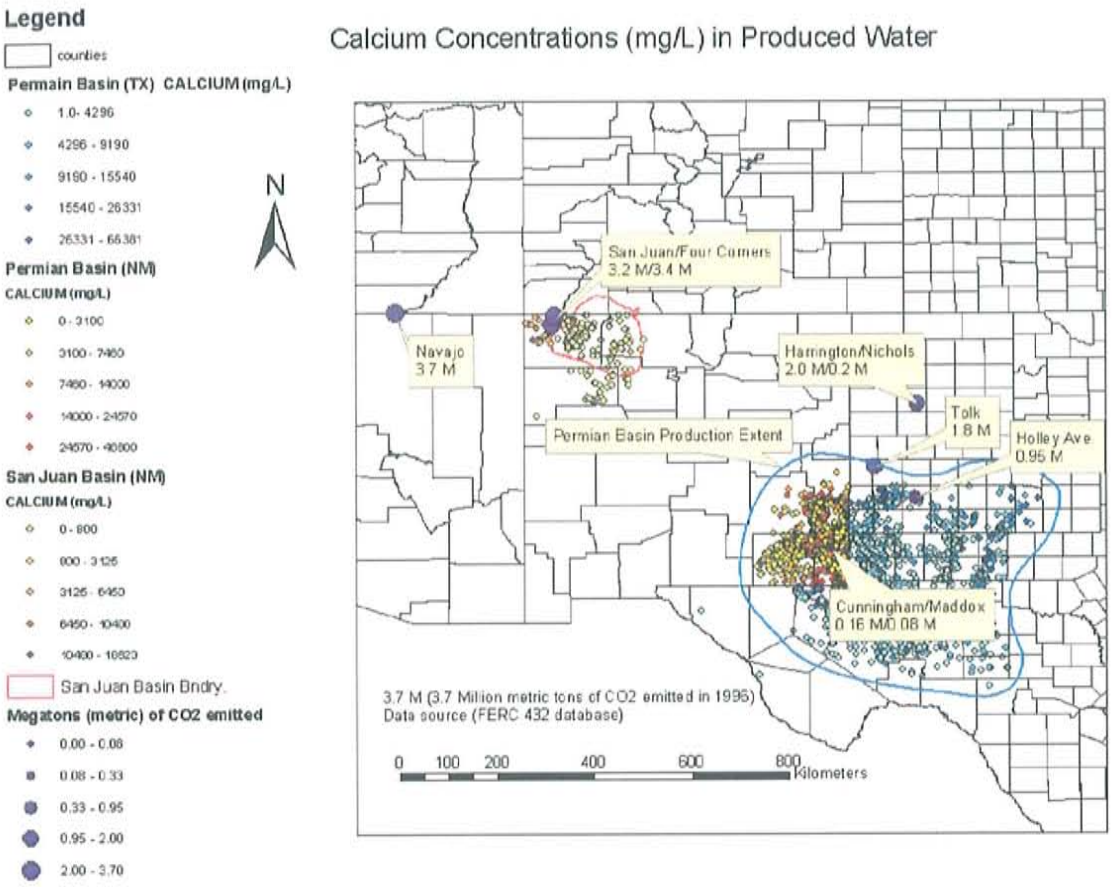

Figure 2-4-4: Permian Basin calcium concentrations in produced water (Bureau of Economic Geology, 2002).

Concentrations of magnesium throughout the Permian Basin are distributed in basin locales similar to calcium concentrations. Magnesium concentrations range between several mg/L in the far western portions of the basin in New Mexico to approximately 28,000 to 38,000 mg/L in portions of the west-central and north-central Permian Basin.

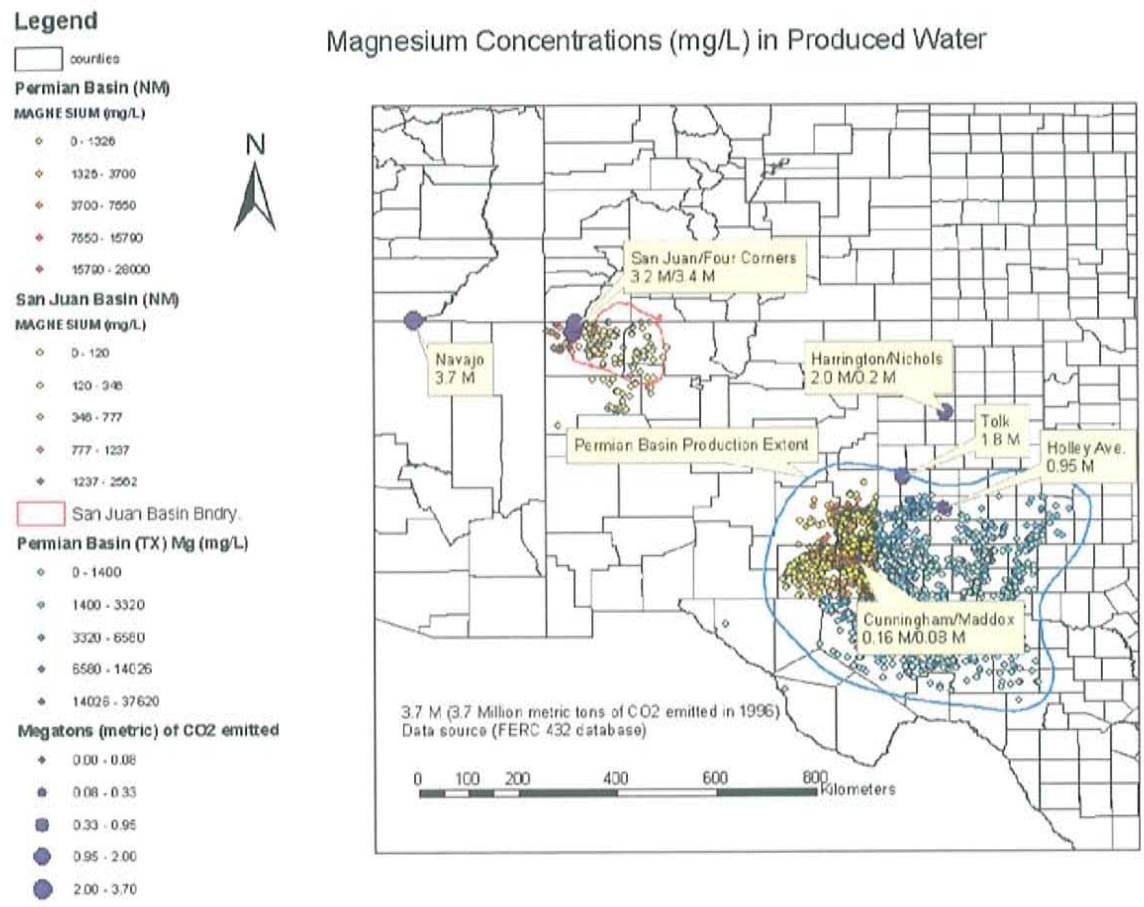

Figure 2-4-5: Permian Basin magnesium concentrations in produced water (Bureau of Economic Geology, 2002)

2.4.2 ABOVE-GROUND MINERALIZATION CAPACITY

The Permian Basin of southeast New Mexico and west Texas provides one of the most ideal settings to research and implement various carbon sequestration technologies. Nine electric power plants could potentially provide in excess of 15.5 Mt of CO_2 to the Permian Basin area. Six of those power plants located in or near the Permian Basin produce a total of 5.19 Mt of CO_2 annually.

As introduced earlier in this chapter, the premise behind this above-ground mineralization technique is based on the use of the biological catalyst carbonic anhydrase

to accelerate the hydration of CO_2 to approach the limit of diffusion-controlled transport. Use of this biomimetic technique to accelerate the hydration of CO_2, in conjunction with a divalent cation source (Ca^{2+} or Mg^{2+}), will provide for the immobilization of carbon in the form of carbonate minerals. Calcium and magnesium ions from produced waters may be utilized as the cation source. Additionally, CO_2 could be gathered from point source emitters (electric power plants, cement manufacturing facilities, etc.), pressurized, and piped to locations close to cation sources (such as oil and gas wells or possibly desalination facilities). Volumes of produced water from the Permian Basin, and available geochemical analyses for these produced waters were used to provide a conservative estimate of the amount of both calcium and magnesium ions they contain. This information was then used to calculate a first-order estimate of the total amount of carbon that could be stored as a result of biomimetic above-ground mineralization. Several important assumptions were made in the process of making these calculations.

- Complex ions of calcium (Ca^{2+}) and magnesium (Mg^{2+}) were neglected.
- Annual mass fluxes of calcium and magnesium ions were calculated based on the annual production of produced water, and calcium and magnesium concentrations.
- Average calcium (5,988 mg/L) and magnesium (1,838 mg/L) concentrations were used in the calculation of the total cation mass for the West Texas Permian Basin.
- All calcium and magnesium produced is utilized during mineralization activities (100 percent efficiency).

Based on these assumptions, a total calcium mass flux of 1.77 billion kilograms (kg) and a total magnesium mass flux of 562 million kg were calculated for 2002. These

totals were converted into an equivalent carbonate mass, revealing that a total carbon mass of 809 million kg or 2.97 Mt of CO_2 could be sequestered in solid carbonate minerals. This would account for more than half of the 5.19 Mt of CO_2 produced annually by the six power plants located within or close to the Permian Basin. As a byproduct of this above-ground mineralization process, large amounts of carbonate minerals would be produced. Possible uses of these carbonate minerals include building materials, road aggregate, carbonate buffering uses, as well as many others.

2.4.3 SUBSURFACE SOLUBILITY TRAPPING

A secondary CO_2 sequestration process that is a possibility within the Permian Basin is subsurface solubility trapping. Bicarbonate- and carbonate-rich brine remaining from above-ground mineralization activities described in the previous section also have carbon capacity. Furthermore, produced water that is not utilized in above-ground mineralization activities could be utilized for additional carbon storage. As discussed previously, this option is quite ideal since brine solutions or produced waters are already reinjected for disposal purposes and for secondary recovery of oil and gas in many oil- and gas-producing basins of the world. For instance, approximately 90 percent of the water produced from oil and gas operations within the Permian Basin of west Texas and southeastern New Mexico is injected, either into producing intervals for secondary recovery (waterflooding) or for disposal via injection into alternate deep subsurface reservoirs.

Understanding the variables affecting CO_2 solubility in water and in solutions with varying total dissolved solids (TDS) is vital to determine carbon capacities of these solutions. Additionally, it is important to understand some of the interactions between

the CO_2 dissolution process and mineral trapping. In the case of produced water that has not been utilized in above-ground mineralization sequestration, it is assumed that CO_2 dissolution occurs relatively rapidly compared to carbonate precipitation. We can then consider solubility trapping as a short-to-medium-term sequestration method (non-reactive sequestration component).

Maximum CO_2 saturation in pure water depends on pressure and temperature. The mole fraction of CO_2 at saturation in fresh water, $x_{w,S}^{CO_2}$, can be calculated according to the Krichevsky-Kasarnovsky equation below (Enick and Klara, 1990):

$$\ln\left(\frac{f_{CO_2}}{x_{w,S}^{CO_2}}\right) = \ln H_{CO_2}^{*} + \frac{\bar{v}_{CO_2}^{\infty}}{RT} P - P_{Sat} \qquad \text{Eq. 2-4-3-1}$$

where f_{CO_2} is the fugacity of pure phase CO_2, $\bar{v}_{CO_2}^{\infty}$ is the molar volume of CO_2 at infinite dilution, T is temperature in K, R = 8.314 (J mol^{-1} K^{-1}) is the universal gas constant, P is the system pressure (mega Pascals (MPa)), P_{Sat} is the saturation pressure (MPa), and $H_{CO_2}^{*}$ is the reference Henry's constant. It should be noted that this equation involves the Poynting correction.

Enick and Klara (1990) used a very large set of data from the literature to develop the following relations for the reference Henry's constant and molar volume of CO_2 at dilution, valid for the temperature range 298-523 K (25-250°C) and the pressure range 3.4 to 72.4 Mpa:

$$H_{CO_2}^{*} = -5032.99 + 30.741113T - 0.052667T^2 + 2.630218 \times 10^{-5} T^3 \qquad \text{Eq. 2-4-3-2}$$

$$\bar{v}_{CO_2}^{\infty} = 1799.36 - 17.8218T = 0.0659297T^2 - 1.05786 \times 10^{-4} T^3 + 6.200275 \times 10^{-8} T^4 \qquad \text{Eq. 2-4-3-3}$$

The fugacity f_{CO_2} of the pure-phase CO_2 is calculated from equations of state (Span and Wagner, 1996). Figure 2-4-6 depicts CO_2 solubility as a function of temperature (T) for several different pressures (P), calculated according to Equations 2-4-3-1 through 2-4-3-3. These ranges of temperature and pressure include conditions typical in various geologic reservoirs (oil and gas reservoirs and deep saline aquifers). As temperatures increase for a given pressure, CO_2 solubility in water initially decreases to a minimum and then, for higher temperatures and pressures, increases to values in some conditions that are higher than the solubility at low temperatures. It should be noted that the minimum solubility is reached for lower and lower temperatures as pressure increases. Additionally, the rate of increase in CO_2 solubility with pressure decreases significantly as the pressure increases.

Produced waters and formation waters of deep aquifers contain dissolved solids, typically on the order of several thousand mg/L (ppm (parts per million), 1 to 5 wt percent of solution) up to around 300,000 mg/L (30 wt percent of solution). The presence of dissolved solids causes a decrease in solubility of light gases such as CO_2, a result of the salting-out effect. Enick and Klara used a large data set of 167 solubility values for the same temperature range of 298-523 K and pressures from 3 to 85 MPa to obtain the following correlation between CO_2 solubility at saturation in saline water, X (in mass fraction), and water salinity S (TDS in weight percent of solution):

$$X_{b,S}^{CO_2} = X_{w,S}^{CO_2}(1.0 - 4.893414 \times 10^{-2} S + 0.1302838 \times 10^{-2} S^2 + 0.1871199 \times 10^{-4} S^3) \quad \text{Eq. 2-4-3-4}$$

This relationship indicates a significant decrease in CO_2 solubility in formation waters as salinity increases.

Figure 2-4-6 illustrates this decrease in CO_2 solubility as a function of salinity (TDS in wt percent of solution) for several different pressures and temperatures based on Equations 2-4-3-1 through 2-4-3-4.

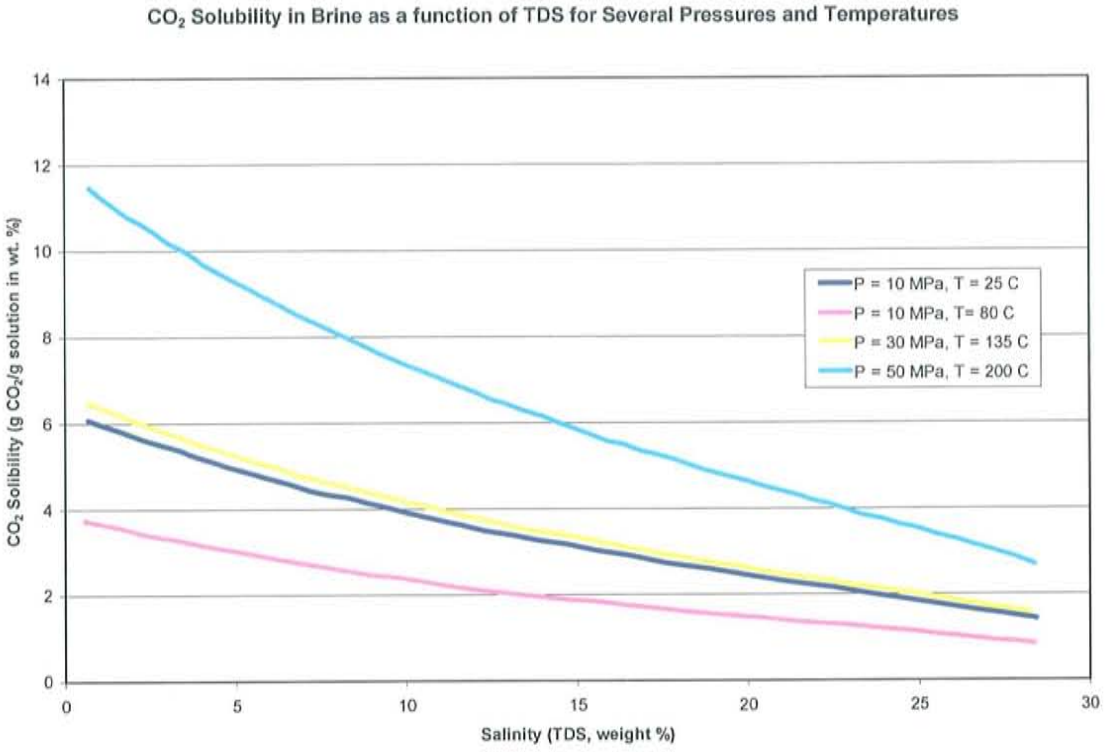

Figure 2-4-6: CO_2 solubility in brine as function of TDS for several pressures and temperatures.

A maximum subsurface solubility trapping estimate based on the volume of produced water re-injected into oil and gas reservoirs and deep saline aquifers of the Permian Basin (90 percent of the total produced water volume (317 billion liters)) and the above CO_2 solubility relationships can be calculated with the following assumptions.

- All produced water that is re-injected is utilized for CO_2 solubility trapping.
- An average total dissolved solid concentration of 106,000 mg/L and an average well depth of the Permian Basin oil and gas wells of 6,700 feet (2.042 kilometers) were calculated from available databases and used for temperature and pressure calculations.

- Average geothermal gradient (30 °C/km) and hydrostatic pressure gradients were used in the calculation of temperature and pressure of produced water.

- All produced water has no initial Total Inorganic Carbon (TIC); therefore, produced water is completely free of initial dissolved carbon ($CO_{2(aq)}$, HCO_3^-, and CO_3^{2-}).

- All solutions (e.g., produced water solutions) reach equilibrium with respect to flue gas.

Based on these assumptions, a total mass of CO_2 sequestered within completely undersaturated produced water of the Permian Basin was calculated to be approximately 30 Mt. A more realistic calculation of CO_2 trapped within undersaturated formation (produced) water can be made by accounting for the dissolved TIC initially within solution. By calculating the TIC in solution using the geochemical speciation model, PHRQPITZ (Fleming and Plummer, 1983), which utilizes the Pitzer Equations (Pitzer, 1979) for solutions with high ionic strengths, one may estimate the difference between the maximum possible TIC in solution and the TIC already in solution. Four different brine/produced water solutions (Solutions 1 through 4) were identified from available data to represent a range of both initial TIC concentrations (17 mg/L to 149 mg/L) and ionic strengths (2.037 mol/kg to 6.51 mol/kg). Distributions of species in water analyses were assumed to be equal to species concentrations in-situ at increased temperature and pressure. Total Inorganic Carbon concentrations of the solutions were calculated after solutions were equilibrated with CO_2 concentrations representative of flue gas associated with electric power plants ($P_{CO2} = 10^{-0.866}$ bars). Differences in the initial and post-equilibrated TIC concentrations were calculated. Table 2-4-1 summarizes the results of the PHRQPITZ equilibration calculations of TIC.

	Soln. 1	Soln. 2	Soln. 3	Soln. 4
pH	6.7	6.5	5.9	6.15
HCO_3^-	195	37	144	238
Ca^{2+}	7,400	11,126	4,880	17,280
Cl-	64,000	161,091	193,000	195,014
Mg^{2+}	675	1,351	8,250	8,651
K^+	1,060	1,323	5,355	2,760
Na+	31,425	88,590	99,107	88,427
SO_4^{2-}	519	950	1,000	550
Ionic Strength	2.037	4.902	6.51	6.296
TIC (initial)	106	17	118	149
TIC (post equilibration)*	269	205	222	248
Change in TIC	163	188	104	99

Notes: All major ion concentrations in mg/L
Ionic Strength in molality (mol/kg)
*Resulted in the equilibration of solution with partial pressure of CO_2 in flue gas ($P_{CO2} = 10^{-0.886}$ bars)

Table 2-4-1: Brine/produced water solutions used for TIC calculations.

Total changes in TIC concentrations between pre-and post-equilibration range between 99 mg/L TIC and 188 mg/L TIC. Based on a TIC capacity of approximately 150 mg/L and the volume of produced water in the Permian Basin that is re-injected (285 billion liters), an annual storage capacity of approximately 0.157 Mt of CO_2 is estimated. Accounting for the resident TIC already in solution decreases the potential CO_2 stored as bicarbonate in solution by a factor of approximately 200. Thus, this storage potential option is effectively negligible.

2.5 CONCLUSIONS AND COMPARISONS

Carbon dioxide sequestration capacities for both a novel biomimetic above-ground mineralization technique and subsurface solubility trapping have been assessed for the Permian Basin of southeast New Mexico and west Texas. Production water data from oil and gas companies and state agencies were utilized as well as empirical relationships for CO_2 solubility, and geochemical models, in order to determine first-

order, conservative estimates of CO_2 sequestration. Capacities for the biomimetic above-ground mineralization technique are for produced waters from the Permian Basin, and the divalent cation mass flux (Ca^{2+} and Mg^{2+}) associated with this produced water is treated as the limiting factor. On this basis, approximately 2.97 Mt of CO_2 can be effectively sequestered annually in immobile carbonate mineral form. This equates to approximately 20 percent of the CO_2 emitted from the nine electric power plants accessible to the Permian Basin infrastructure (including CO_2 pipelines), and approximately 57 percent of the CO_2 emitted from the six of those power plants that are actually located in or close to the Permian Basin.

If the dissolved TIC already present in water is neglected, there would appear to be a vast amount of potential CO_2 storage via subsurface solubility trapping, approximately 30 Mt of CO_2. However, accounting for the TIC present in production and formation water decreases the CO_2 solubility trapping potential by approximately 200-fold (to ~0.157 Mt of CO_2), negligible for practical purposes.

It is generally accepted that continued anthropogenic use of carbon as a fuel will adversely affect the global climate if the related emission of greenhouse gases continues unabated. However, novel techniques of carbon sequestration, such as geologic sequestration techniques and biomimetic sequestration techniques, can provide for mitigation of greenhouse gas emissions.

CHAPTER 3:

EVALUATION OF DAWSONITE AS A MINERAL TRAP IN CO_2 SEQUESTRATION: WEST PEARL QUEEN RESERVOIR CO_2 INJECTION CASE STUDY (PERMIAN BASIN, NEW MEXICO)

3.1 ABSTRACT

The purpose of this study was to evaluate the potential of dawsonite ($NAlCO_3(OH)_2$) as a mineral "trap" for sequestration of CO_2. The West Pearl Queen Reservoir CO_2 pilot injection test (Abel et al., 2004, Pawar et al., 2003, Stauffer et al., 2003), located in southeast New Mexico, was used as a case study example to examine reactive processes associated with CO_2 injection into a sub-arkosic sandstone depleted oil reservoir, specifically as it relates to dawsonite formation. Previous studies emphasizing reactive processes during geologic (subsurface) CO_2 injection parameterized precipitation/dissolution reaction rates with kinetic reaction rate constants of various minerals that vary over several orders of magnitude (Gaus et al, 2003, Xu and Pruess, 2001, Johnson et al, 2001, and Stauffer et al, 2003). Specifically, kinetic rate constants of aluminosilicate minerals, such as potassium feldspar ($KAlSi_3O_8$) and albite ($NaAlSi_3O_8$) vary over 3 to 4 orders of magnitude (i.e. $KAlSi_3O_8$ varied between 1.0×10^{-17} and 1.62×10^{-13} and mole/cm^2-sec.). Furthermore, kinetic rate constants for dawsonite vary between 1.0×10^{-16} and 1.38×10^{-11} mole/cm^2-seconds in these studies. Based on kinetic reaction rate parameterizations from these studies, reaction path and reactive transport models

were developed to investigate the impact of the disparity in kinetic rate constant parameters of these minerals on the reactive process during and after subsurface CO_2 injection in the case of the West Pearl Queen Reservoir pilot injection test. Results indicate that kinetic rate constant disparities greatly influence simulated dawsonite precipitation times and dissolution times of aluminosilicate minerals. Dawsonite precipitation timing varied between less than 2 years and 12,000 years in the case of the West Pearl Queen Reservoir. Uncertainties in mineral kinetics produce great uncertainties in the prediction of CO_2 fate and transport and subsurface mineralization as a result of CO_2 injection in general. It was established that further kinetic reaction rate determination studies, specifically relating to aluminum silicates and dawsonite, were required to constrain reactive transport simulation associated with geologic sequestration of CO_2.

Finally, an evaluation of CO_2 plume trapping propensity by a process we term "plume fringe mineralization" (PFM) was made for the West Pearl Queen Reservoir. First, we describe the conceptual model of CO_2 plume trapping in general terms. Results of reactive transport models of the West Pearl Queen Reservoir pilot injection test indicate that long-term storage (i.e. residence times of greater than 50,000 years) of the separate-phase CO_2 mass is an unlikely scenario due to the low aluminosilicate content of the overlying bounding unit, the Seven Rivers Formation. Implications of this timing study are further discussed in relation to other CO_2 injection scenarios, with specific focus on the possibility of CO_2 plume trapping as a means of long-term sequestration.

3.2 INTRODUCTION

Many CO_2 sequestration studies in recent years have focused on the fate and transport of separate-phase CO_2 in the context of long-term sequestration. Specifically,

direct injection and storage of supercritical CO_2 within deep saline reservoirs and depleted oil and gas reservoirs may have significant side effects. These targets have varying ranges of estimated storage potential. Previous studies by Van der Meer (1993), Law and Bachu (1996), and Weir et al. (1996) emphasized physical processes relating to the flow and transport of supercritical CO_2 within deep saline reservoirs and its impact on storage potential for various types of basin settings. More recent studies have focused on the chemical interactions between CO_2, brine (formation water), and reservoir minerals to evaluate mineralization and dissolution reactions that occur within target reservoirs. Studies by Johnson et al. (2001), Xu and Pruess (2001), Pruess et al. (2003), and Gaus et al. (2003) focused on storage capacities of basin reservoirs, including effects of mineralization and dissolution. Throughout these and other studies concerning subsurface reactive transport of CO_2, parameterizations for kinetic rate constants for active minerals vary over several orders of magnitude. These disparities among the kinetic rate constants produce ambiguities for the precise timing of mineralization and dissolution of certain minerals. The uncertainties associated with brine-mineral-CO_2 systems, specifically with the kinetic rates in the geochemical reactions, pose a significant obstacle for adequate prediction of impacts associated with subsurface injection of CO_2 (Wawersik et al, 2001). Ability to predict timing of mineralization and dissolution is especially important for the possibility of trapping separate-phase CO_2 plumes by mineralization at the plume margin or fringe.

3.3 CONCEPTUAL MODEL

The concept of CO_2 plume trapping can be easily described by examining an actual CO_2 injection scenario through time. Figure 3-3-1 illustrates some important processes that may influence the ultimate flow and transport of separate-phase CO_2.

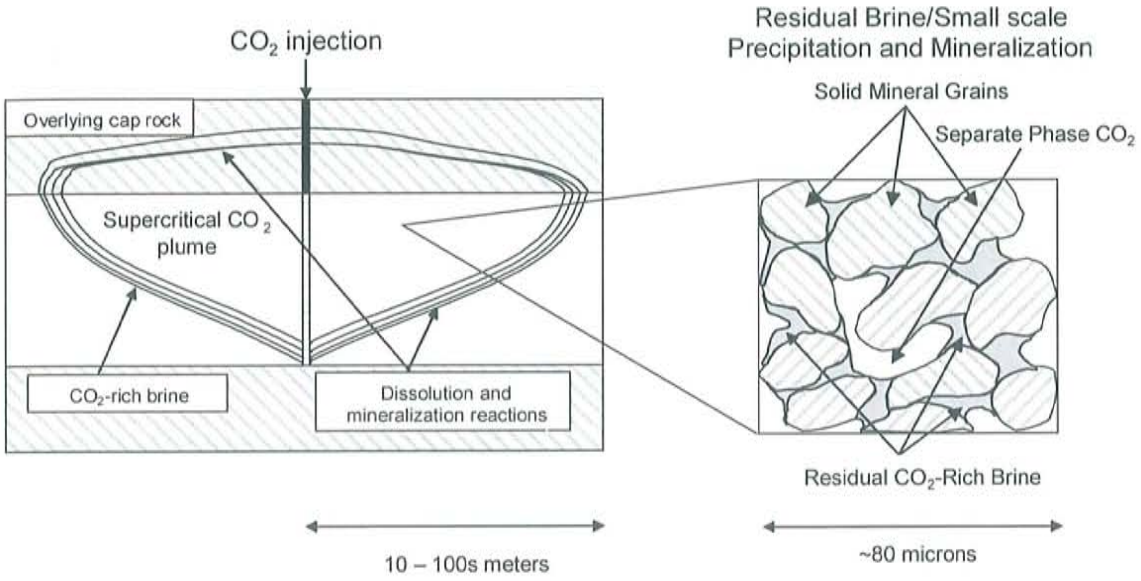

Figure 3-3-1: Conceptual model for CO_2 plume trapping through mineralization.

After supercritical CO_2 is injected within a target reservoir, transport and residence time of CO_2 will depend mainly on permeability (horizontal k_h and vertical k_v) of the target formation and overlying cap rock formation. As supercritical CO_2 migrates upward within the target formation, some of it will dissolve in the resident groundwater or brine. Storing CO_2 in solution is termed "solubility trapping" (Johnson et al., 2001, Gaus et al., 2003, and Bachu and Adams, 2003). Increased CO_2 in solution causes changes in geochemical conditions within these regions, including increased dissolution and mineralization processes (e.g. Johnson et al., 2001, Pruess, 2003). Supercritical CO_2 will dissolve at the plume-groundwater interface, the region we term the plume "fringe." The CO_2 plume front is probably the most reactive portion of the system in carbonate-dominated reservoirs due to reduced pH associated with increased CO_2 in solution. As CO_2 is injected, formation water or brine is displaced by supercritical CO_2. Continued injection will lead to complete displacement, except for an irreducible amount of brine held in place by capillary forces ("irreducible saturation"). Residual brine and

supercritical CO_2 interact to produce CO_2-rich brine, which can then chemically react with surrounding solid grains. Thus, residual CO_2-rich brine can provide another prospect for trapping by mineralization.

In the plume fringe and in areas within the plume with higher brine saturations, CO_2-rich brine may react with reservoir minerals to reduce porosity and permeability. Mineralization at the plume fringe may reduce porosity and permeability enough to form an effective hydrodynamic trap, preventing further migration of separate-phase CO_2. Additionally, pore space alterations within the plume, associated with CO_2-rich brine, may further change the flow dynamics as CO_2 injection progresses. The process of CO_2 plume trapping by fringe mineralization is termed "Plume Fringe Mineralization" (PFM). Major classes of minerals that play a role in this fringe mineralization concept are the carbonate and aluminum silicate classes. Recent modeling and laboratory studies of CO_2 sequestration have confirmed that these classes of minerals are dynamic under conditions of CO_2-rich brine. A laboratory study by Kaszuba et al. (2002) utilized batch experiments with high supercritical CO_2 pressures and high temperatures in arkosic sandstones. Findings suggested magnesite precipitation and albite dissolution over a period of several months. Relevant reactions include

$$Mg^{2+} + CO_2(aq) + H_2O \rightleftharpoons MgCO_3 + 2H^+ \quad , \qquad \text{and} \qquad \text{Eq. 3-3-1}$$

$$NaAlSi_3O_8 + 2H_2O + 4CO_2(aq) \rightleftharpoons Na^+ + Al^{3+} + 3SiO_2(aq) + 4HCO_3^- . \qquad \text{Eq. 3-3-2}$$

Modeling studies performed by Johnson et al. (2003) emphasized reactive transport processes occurring within sandstone strata, including deep saline aquifers and depleted oil reservoirs. Their simulation results also suggested magnesite precipitation along the CO_2 plume/brine interface, in addition to dawsonite precipitation.

3.4 DAWSONITE FORMATION

Dissolution of aluminum silicates provides the aluminum in solution that is necessary for dawsonite to precipitate (Eq. 6-4-1 and Eq. 6-4-2), or

$$NaAlSi_3O_8 + CO_2(aq) + H_2O \rightleftharpoons 3SiO_2(aq) + NaAlCO_3(OH)_2 \ , \qquad \text{Eq. 3-4-1}$$

$$KAlSi_3O_8 + H_2O + CO_2(aq) + Na^+ \rightleftharpoons 3SiO_2(aq) + NaAlCO_3(OH)_2 + K^+ . \qquad \text{Eq. 3-4-2}$$

Several other CO_2 sequestration studies concluded that dawsonite might be a significant precipitate. Reactive transport and chemical kinetic modeling studies by Xu and Pruess (2001), Gaus et al. (2003), and Johnson et al. (2003) provide details of mineralization and dissolution processes within sites of ongoing CO_2 injection. However, the timing of these mineralization and dissolution processes vary greatly among these studies.

Kinetic rate constants for minerals vary over several orders of magnitude within these modeling studies, resulting in ambiguities within the precise timing of secondary mineral formation. At least one study (Johnson et al, 2003) predicts high volume precipitation of dawsonite in CO_2 sequestration targets, making dawsonite a compelling issue. Dawsonite volume fractions were predicted to increase to approximately 0.15 within 20 years in the study by Johnson et al. (2003). However, other modeling studies predict little or no dawsonite, or predict time of precipitation initiation at thousands of years or longer. Additionally, most laboratory studies do not produce dawsonite under reservoir sequestration conditions.

Only one known successful laboratory replication of dawsonite precipitation was documented by Palandri (2004). Other laboratory experiments concerning CO_2 sequestration mineral reactions have not precipitated dawsonite (e.g. Kaszuba et al.

2002). Temperature conditions within the study by Kaszuba et al. (2002) were set very high (~ 200°C), whereas the study in Palandri (2004) used somewhat lower temperatures (~ 50 – 70°C). This temperature contrast provides insight about the stability of dawsonite. The mineral precipitation timing study presented in this study focuses on the timing and stability of dawsonite for the West Pearl Queen Reservoir pilot injection test and how the uncertainties in mineral kinetic reaction rate constants affect predictions of the precipitation/dissolution timing of certain minerals and the ultimate fate and transport of injected CO_2. Temperature effects on dawsonite precipitation are also examined through temperature activity diagrams. While disparities among laboratory and modeling studies make for uncertainty about dawsonite production in CO_2 sequestration target reservoirs, another important issue concerns the conditions under which dawsonite forms naturally.

Dawsonite is categorized as a rare sodium-aluminum-hydroxl carbonate. Occurrences of natural dawsonite are found in several locations throughout the world. Dawsonite was first discovered as a new mineral species in the vicinity of Montreal, Quebec (Harington, 1874). The formation of dawsonite was later related to low-temperature hydrothermal systems where it was formed by the decomposition of feldspars (Palache et al., 1960). Other occurrences and studies have followed since its discovery. One study by Smith and Milton (1966) documents the abundance of dawsonite within the Eocene Green River Formation oil shales of the Piceance Creek Basin in northwestern Colorado. Within these oil shales, dawsonite comprises approximately 25 percent of the mineralogy. The dawsonite crystal habit within these oil shales is primarily characterized by thin sheets or lenses parallel to bedding. It is also

found transverse to the bedding and partially filling fractures at high angles to bedding. Dawsonite crystals are also found naturally in microscopic vugs (Smith and Milton, 1966).

Dawsonite has also been seen to be of authigenic origin (Aikawa et al., 1972, Volkova and Rekshinskaya, 1973) and has been observed in Permian sediments of the Sydney Basin in Australia (Goldberry and Loughnan, 1977). A diagenetic study of the Aldebaran Sandstone within the Denison Trough of Australia finds dawsonite as a widespread pore filling mineral (Baker, 1991). Within this study, dawsonite was observed to form in the marine sandstones exclusively and was characterized by its acicular crystal habit. Dawsonite crystals typically formed bundles, tufts, fans, rosettes, and vermicules. In a study by Baker (1991), the precipitation of dawsonite was suggested to correspond to CO_2-rich fluids associated with hydrocarbons. Dawsonite abundance was high (up to 13.4 percent of bulk rock volume) suggesting that precipitation was primarily controlled by the flux of pore water. One important detail concerning the study of dawsonite occurrence within the Aldebaran Sandstone is the temperature of the reservoir during dawsonite precipitation. Temperatures of the reservoir during precipitation were estimated as being approximately the same as present day reservoir temperatures ($< 100°C$). Another study completed by Baker et al. (1995) found that dawsonite present within the Bowen-Gunnedah-Sydney Basin in eastern Australia most likely formed in a temperature range of $25°C$ to $75°C$. The results of these studies have uncovered useful information regarding dawsonite formation under natural conditions. These results also provide insight regarding how dawsonite precipitation may affect reservoirs during CO_2 injection.

3.5 WEST PEARL QUEEN RESERVOIR CASE STUDY

We selected a CO_2 pilot injection test as a case study to examine processes involved in CO_2 plume trapping through fringe mineralization. The West Pearl Queen Reservoir pilot injection test was selected due to its close proximity to our research facilities here at New Mexico Tech and an ongoing collaboration with researchers at Los Alamos National Laboratory and Sandia National Laboratories, who led the pilot (Pawar et al., 2003) (Stauffer et al., 2003). The reservoir has been highly characterized because of its oil production activities in the last 25 years. The reservoir is located approximately 20 miles west of the town of Hobbs in southeastern New Mexico. The dominant producing interval is the Shattuck Sandstone Member of the Queen Formation (Figure 3-5-1).

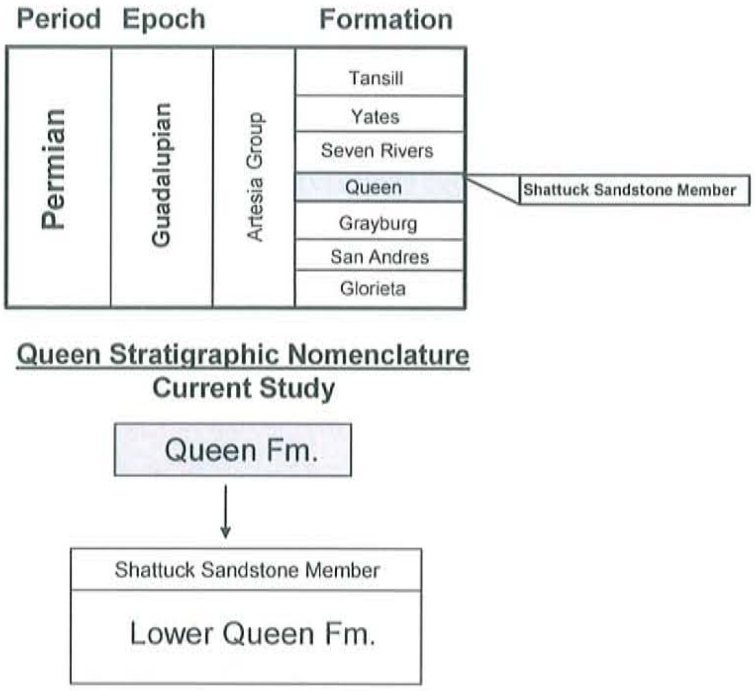

Figure 3-5-1: Stratigraphic section of the Northwest Shelf and equivalent shelf-edge and basin deposits (after Garber et al. 1989) and the Queen stratigraphic nomenclature adopted within this study.

We assembled a summary geologic characterization of the West Pearl Queen Reservoir. Some of the major characteristics of the reservoir pertinent to this study include:

- Extremely underpressured; 5 MPa under typical hydrostatic conditions, no flow conditions, at 1,371 meters depth
- Domal (anticlinal) structural trap
- Arkosic to sub-arkosic sandstone reservoir (approximately 12 m thick)
- Low-permeability, evaporite-rich cap rock unit (Seven Rivers Formation)
- NaCl-dominated brine (180,000 mg/L)
- Reservoir temperature of 45 °C

The CO_2 injection test was performed in December 2002 to February 2003, with approximately 2,100 tons (~1,900 metric tonnes) of supercritical CO_2 injected into the Shattuck Sandstone Member of the Queen Formation. Post-injection activities included a 6-month "soak" period, a CO_2 production (venting) event, and a seismic survey for CO_2 plume delineation. (Appendix A) (Pawar et al., 2003) (Stauffer et al., 2003).

Due to the underpressured nature and static flow conditions of the West Pearl Queen Reservoir, we decided that fully coupled reactive flow and transport simulations would be superfluous. More simple reaction path models were deemed adequate to examine reaction paths and mineral volume fraction changes within the assumed hydrostatic system. Geochemist's Workbench was used with the REACT module (Bethke, 2002) to simulate reaction paths. Associated porosity changes in the reservoir were simulated with TRANS (Lichtner, 2000), given that REACT cannot calculate porosity effects. Reactions were determined for the Shattuck Sandstone Member and the

Seven Rivers Formation (overlying cap-rock unit). Brine compositions for the Shattuck Sandstone Member and the Seven Rivers Formation are summarized in Tables 3-5-1 and 3-5-2, respectively. Bulk mineralogies of subsequent units are listed in Tables 3-5-3 and 3-5-4.

Species	Total concentration (molality)
Al^{3+}	4.1×10^{-10}
$SiO_2(aq)$	2.2×10^{-4}
Na^+	2.39
K^+	5.0×10^{-3}
Mg^{2+}	7.0×10^{-2}
Ca^{2+}	7.6×10^{-2}
Cl^-	2.66
SO_4^{2-}	1.25×10^{-2}
$CO_2(aq)$	1.6×10^{-5}
pH	7.28

Table 3-5-1: Speciation calculation results (Shattuck Sandstone).

Species	Total concentration (molality)
Al^{3+}	4.1×10^{-10}
$SiO_2(aq)$	2.2×10^{-4}
Na^+	2.39
K^+	4.6×10^{-8}
Mg^{2+}	5.5×10^{-3}
Ca^{2+}	0.152
Cl^-	2.68
SO_4^{2-}	1.6×10^{-2}
$CO_2(aq)$	7.3×10^{-7}
pH	7.8

Table 3-5-2: Speciation calculation results (Seven Rivers Formation).

Bulk Mineralogy of the Shattuck Sandstone Member

Percent by volume (% volume)

Albite ($NaAlSi_3O_8$)	0.2
Quartz (SiO_2)	0.57
Calcite ($CaCO_3$)	0.0005
Dolomite ($CaMg(CO_3)_2$)	0.0175
Microcline ($KAlSi_3O_8$)	0.046
Anhydrite ($CaSO_4$)	0.02
Porosity	0.146

Table 3-5-3: Bulk mineralogy of the Shattuck Sandstone Member (Krumhansl et al. (2003) and Westrich et al. (2002)).

Bulk Mineralogy of the Seven River Formation

Percent by volume (% volume)

Quartz (SiO_2)	0.043
Dolomite ($CaMg(CO_3)_2$)	0.19
Microcline ($KAlSi_3O_8$)	0.046
Anhydrite ($CaSO_4$)	0.65
Porosity	0.071

Table 3-5-4: Bulk mineralogy of the Seven Rivers Formation (Brister and Ulmer-Scholle (2003)).

3.5.1 DAWSONITE PRECIPITATION TIMING

A sensitivity modeling analysis was designed to constrain timing of dawsonite formation within the reservoir. Within this analysis, kinetic rate constants were obtained for several different studies and used as the varying parameter. Tables 3-5-5 (a) and 3-5--5 (b) summarize the kinetic rate constants used within each study.

(a)

Study	K-Feldspar (mole/cm^2-s)	Uncertainty	K-Feldspar SSA (cm^2/g)	Albite (mole/cm^2-s)	Uncertainty	Albite SSA (cm^2/g)	Dawsonite (mole/cm^2-s)	Uncertainty	Dawsonite SSA (cm^2/g)
1 [6]	1.62×10^{-13}	27% [6]	711	3.63×10^{-13}	27% [6]	695	1.38×10^{-11}	Not Defined (Set Intermediate (Calcite and Dolomite))	849
2 [6]	1.00×10^{-16}	27% [6]	711	1.00×10^{-16}	27% [6]	695	[4] See Notes Below	Not Defined	849
3 [6]	1.78×10^{-14}	27% [6]	711	[2] See Notes Below	Not Defined	695	1.00×10^{-11}	Not Defined (Set Intermediate (Calcite and Magnesite))	849
4 [3]	1.00×10^{-17}	Not Defined [5]	124	1.00×10^{-16}	Not Defined [5]	248	1.00×10^{-16}	Not Defined [5]	124

(b)

Study	Dolomite-dis (mole/cm^2-s)	Dolomite-dis SSA (cm^2/g)	Quartz (mole/cm^2 s)	Quartz SSA (cm^2/g)	Anhydrite (mole/cm^2-s)	Anhydrite SSA (cm^2/g)
1 [6]	4.17×10^{-12}	635	1.86×10^{-16}	681	1.00×10^{-13}	650
2 [6]	1.60×10^{-14}	635	1.26×10^{-18}	681	1.00×10^{-13}	650
3 [6]	[2] See Notes Below	635	1.04×10^{-18}	681	1.00×10^{-13}	650
4 [3]	1.00×10^{-18}	12,400	1.00×10^{-18}	207	1.00×10^{-13}	41,322

Notes: 1: Gaus et al. (2003)
2: Xu et al. (2002)
3: Johnson et al. (2001)
4: Stauffer et al. (2003)
[2] No data provided (set to study 2 parameter)
[3] Specific Surface Areas were determined from Reactive Surface Areas (cm^{-1}) calculated in Stauffer et al. (2003) (A West Pearl Queen bulk density of 2.42 g/cm^3 was used)
[4] No data provided (set to study 4 parameter)
[5] Parameterized according to batch experiments of the West Pearl Queen Shattuck Sandstone Reservoir
[6] Feldspar reaction rates based on studies conducted by Blum and Stillings (1995), and Stillings and Brantley (1995)
SSA = Specific Surface Area (SSA's in studies 1 through 3 were set equal to SSA's defined in Gaus et al. (2003))

Table 3-5-5 (a) and (b): Summary table of kinetic rate constants and specific surface areas used in current study

For simplicity, specific surface areas of each mineral were set to specific surface areas determined by Gaus et al. (2003) in studies 1 through 3. The specific surface areas for study 4 (Stauffer et al., 2003) were obtained by actual batch reaction experiments with West Pearl Queen Reservoir samples. Thus, specific surface areas from Stauffer et al. (2003) most closely replicate actual specific surface areas of the West Pearl Queen Reservoir. It should be noted that batch experiments might result in very different reactive properties compared to the field because of reworking and disturbance of porous material. Kinetic reaction path models representing each of these studies (studies 1 through 4) were implemented within REACT of Geochemist's Workbench. Appropriate concentrations of CO_2 in the brines of the Shattuck Sandstone and Seven Rivers Formation were obtained by equilibration of the respective formation brines with a CO_2 partial pressure of 50 bars. $CO_{2(aq)}$ concentrations within the brines were initially defined from simulations of the separate-phase CO_2 flow and transport at the reservoir scale with TOUGH2-EOSCO2 (Cole, 1999). Dissolved CO_2 mass fractions were provided as a result of these simulations and were used to determine $CO_{2(aq)}$ concentrations through the following relationship:

$$C_{CO2} = \frac{XCO_2}{GFW}\rho_{mix} \qquad \text{Eq. 3-5-1}$$

where, C_{CO2}, is molar CO_2(aq) concentration, XCO_2 is dissolved CO_2 mass fraction in kg per kg, GFW is the gram formula weight of CO_2(aq) in kg per mole, and ρ_{mix} is the density of the CO_2-water mixture in kg per liter (Cole, 1999). Dissolved CO_2 mass fractions in these simulations were no higher than 0.04 kg CO_2/kg-solution.

Concentrations determined by the conversion of these CO_2 mass fractions were approximately 1 molal CO_2(aq). The resulting CO_2-rich brines for the Shattuck Sandstone and the Seven Rivers Formation are summarized in Table 3-5-6.

Simulated CO_2-rich brines				
Shattuck Sandstone			Seven Rivers Formation	
Species	molality		Species	molality
Al^{3+}	4.10×10^{-10}		Al^{3+}	4.10×10^{-10}
SiO_2(aq)	1.4×10^{-6}		SiO_2(aq)	2.2×10^{-4}
Na^+	2.37		Na^+	2.36
K^+	4.6×10^{-3}		K^+	4.5×10^{-8}
Mg^{2+}	0.128		Mg^{2+}	0.024
Ca^{2+}	0.0722		Ca^{2+}	0.177
Cl^-	2.74		Cl^-	2.73
SO_4^{2-}	0.01		SO_4^{2-}	0.014
CO_2(aq)	1.064		CO_2(aq)	1.064
pH	4.76		pH	4.55

Table 3-5-6: Simulated CO_2-rich brines of the Shattuck Sandstone and the Seven Rivers Formation.

Figures 3-5-2 through 3-5-5 illustrate the simulated timing of dawsonite precipitation (time at which dawsonite mineral volume equals at least 0.10 cm^3 per unit volume) within the Shattuck Sandstone. Simulated precipitation times of dawsonite formation increase within these figures as illustrated. As kinetic reaction rate constants decrease between study 1 (Gaus et al, 2003) and study 4 (Stauffer et al, 2003), dawsonite precipitation timing increases from less than 2 years in study 1 (Gaus et al, 2003) to approximately 12,000 years in study 4 (Stauffer et al, 2003).

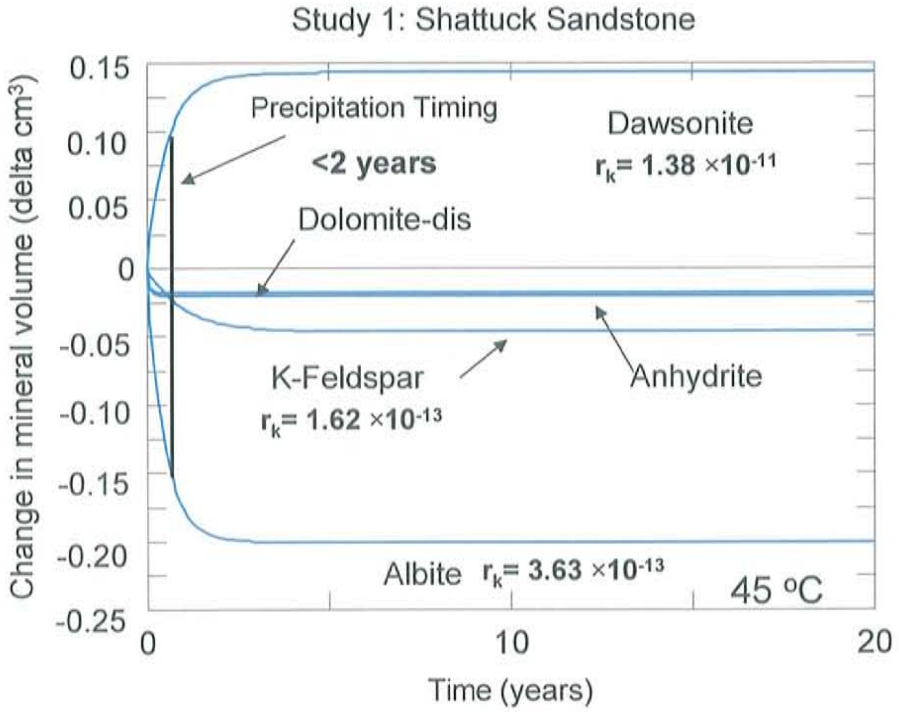

Figure 3-5-2: Dawsonite precipitation in the Shattuck Sandstone (study 1, Gaus et al, 2003). r_k denotes kinetic rate constant used for pertinent minerals, ("Fast" kinetic rate).

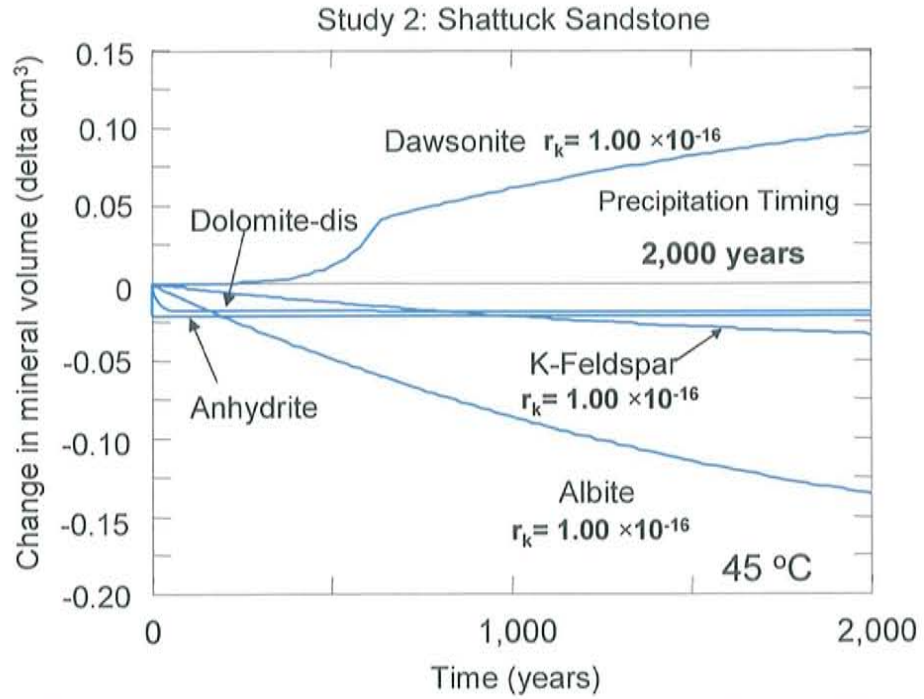

Figure 3-5-3: Dawsonite precipitation in the Shattuck Sandstone (study 2, Xu et al, 2002). r_k denotes kinetic rate constant used for pertinent minerals, ("Moderately fast") kinetic rate.

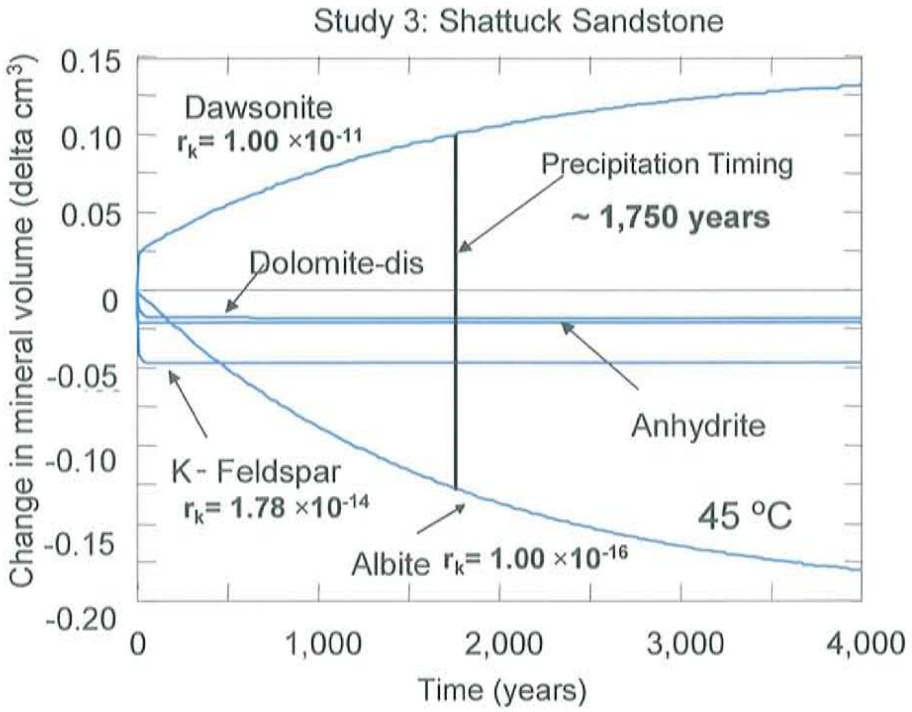

Figure 3-5-4: Dawsonite precipitation in the Shattuck Sandstone (study 3, Johnson et al, 2001). r_k denotes kinetic rate constant used for pertinent minerals, ("Moderately fast") kinetic rate.

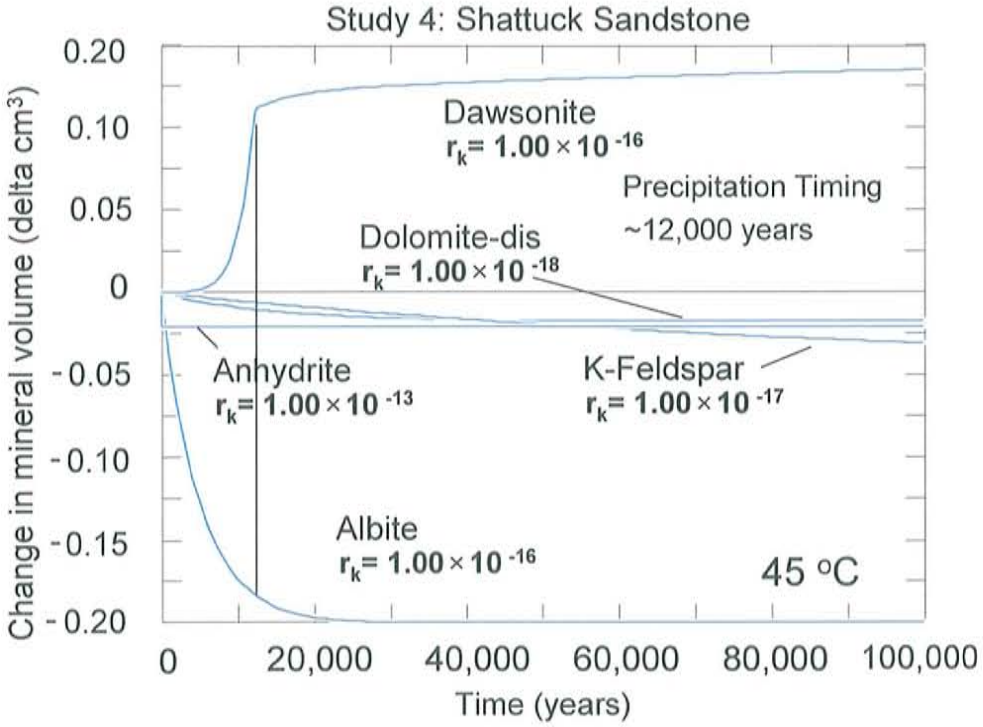

Figure 3-5-5: Dawsonite precipitation in the Shattuck Sandstone (study 4, Stauffer et al, 2003). r_k denotes kinetic rate constant used for pertinent minerals. ("Slow") kinetic rate.

Common to all simulations is the coupled relationship between dawsonite precipitation and aluminum silicate dissolution. As albite and potassium feldspar dissolve, Al^{3+} ions are released into solution. Sodium ions are in abundance due to the brine composition (Na^{+}= 2.37 molal) and carbonate concentrations are high due to the CO_2 in solution. These are ideal conditions for dawsonite precipitation. Timing of dawsonite precipitation, however, is uncertain. Table 3-5-7 summarizes the results of the dawsonite precipitation study conducted within this study.

Study	Dawsonite (mole/cm^2-s)	Albite (mole/cm^2-s)	K-feldspar (mole/cm^2-s)	Precipitation Timing (years)
1	1.38×10^{-11}	3.63×10^{-13}	1.62×10^{-13}	< 2
2	1.00×10^{-16}	1.00×10^{-16}	1.00×10^{-16}	2000
3	1.00×10^{-11}	1.00×10^{-16}	1.78×10^{-14}	1750
4	1.00×10^{-16}	1.00×10^{-16}	1.00×10^{-17}	12,000

Table 3-5-7: Dawsonite precipitation timing summary with kinetic rate constants for selected minerals.

Timing of dawsonite precipitation is highly dependent on the kinetic rate constants of aluminum silicate mineral dissolution (Table 3-5-7). Large kinetic rate constants for dawsonite, albite, and potassium feldspar (study 1) result in a rapid precipitation time of less than 2 years. Rate constants for dissolution of the primary aluminum silicate mineral (albite) that are lower by ~3 orders of magnitude increase dawsonite precipitation timing by ~ 3 orders of magnitude (study 3). Dawsonite precipitation timing is controlled by dissolution of the dominant aluminum silicate within the system.

Interaction between CO_2-rich brine and the cap rock formation provides an opportunity for mineralization to increase the sealing integrity of the reservoir. In the case of the West Pearl Queen Reservoir, however, the Seven Rivers Formation cap rock unit is dominated by anhydrite and dolomite. Reaction path modeling of the Seven Rivers Formation shows an overall dissolution-dominated system, resulting in a net increase in porosity, and ultimate sealing integrity of this cap rock unit degrades through time.

One-dimensional simulations of reactive flow and transport were implemented in TRANS to show the change in porosity due to the mineralization and dissolution reactions presented above. A detailed description of the governing equations associated with TRANS is presented in Appendix B (Lichtner, 2000). The model design for these one-dimensional simulations is depicted in Figure 3-5-6.

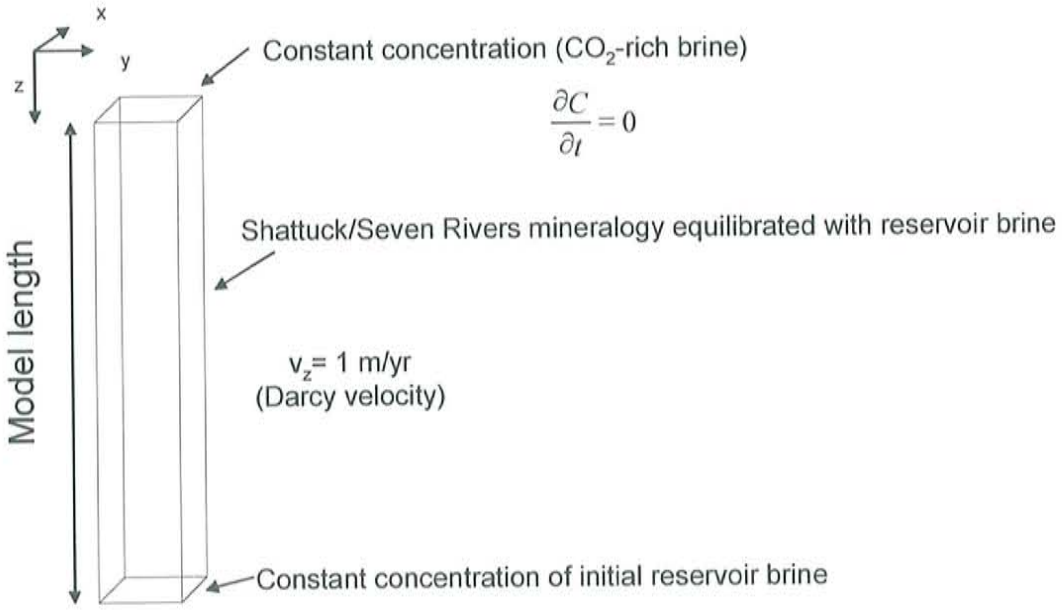

Figure 3-5-6: Schematic of TRANS 1D model design.

A one-dimensional domain was designed where the mineralogy of the Shattuck Sandstone and Seven Rivers Formation was defined along the domain with parameters summarized in Tables 3-5-1 and 3-5-3. Initial reservoir brine compositions used were identical to the reaction-path model brine compositions. Zero-concentration-gradient boundary conditions were established at both ends of the domain, with the top boundary representing CO_2-rich brine and the bottom boundary set to initial reservoir brine compositions. In this model (Figure 3-5-6), multicomponent mass transport of chemical species proceeds from one boundary to the other at a constant velocity in the z-direction of 1 m/yr (3.17×10^{-8} m/s). Specific surface areas and rate constants of the Stauffer et al. (2003) case were used due to matching batch experiments utilized in their study, and will most likely provide the best estimate for reactive time scales.

It should be noted that porosity changes predicted by these one-dimensional reactive transport models are an overestimation of the porosity changes within the actual West Pearl Queen Reservoir. No-flow conditions exist within the reservoir, and hence the implementation of a flow field in these one-dimensional models will overestimate the multicomponent mass transport. The overestimation of multicomponent mass transport is due to the inclusion of advective multicomponent transport. In no-flow conditions, multicomponent mass transport would only take place due to diffusion. An overestimation in this mass transport ultimately results in an exaggerated porosity change for actively precipitating minerals in the system. Evolution of the brine composition and changes in mineralogy are modeled as a function of time and distance along the model domain.

Permeability changes due to changes in porosity are modeled with a phenomenological power law relation of the following form:

$$k = k_o \left(\frac{\phi}{\phi_o} \right)^n \left[\frac{1.001 - \phi_o^2}{1.001 - \phi^2} \right],$$

k = permeability (m^2)

k_o = initial permeability (m^2)

ϕ = porosity (-)

ϕ_o = initial porosity (-)

n = constant equal to 3.

Eq. 3-5-2

The porosity is calculated according to the mineral volume fraction within the TRANS simulation. This power law relation is based on the previous work conducted by Lichtner et al. (1996). Results of simulations with rate constants from the Stauffer et al. (2003) case study are displayed in Figures 3-5-7 through 3-5-14. One-dimensional reactive flow and transport simulations of CO_2-rich brine in the Shattuck Sandstone show a general decrease in porosity over the domain length over 500,000 years (Figure 3-5-7). Permeability decreases approximately 63 percent from 6.2×10^{-14} m^2, initially (pre-simulation), to approximately 2.3×10^{-14} m^2 in the downstream section of the model domain after 250,000 years (Figure 3-5-8).

Results of these one-dimensional reactive transport simulations confirm the reactions predicted within the reaction path modeling previously presented. Dawsonite precipitates at a very slow rate (Figure 3-5-9) while albite (Figure 3-5-10), potassium feldspar (Figure 3-5-11), and anhydrite (Figure 3-5-13) dissolve. Dolomite dissolves within the first portion of the model and then precipitates at the opposite boundary at a time of 500 years (Figure 3-5-12). This dolomite precipitation front propagates through the model at 1,000 and 5,000 years. Dawsonite volume fraction over the model length

(Figure 3-5-9) increases from essentially zero at the start of the simulation to 0.145 at 40,000 years. The precipitation of dawsonite essentially mirrors the dissolution of albite (Figure 3-5-10), due to the coupled behavior between the reactions as seen in the reaction path modeling. Areas where albite dissolution predominates correspond to dawsonite precipitation regions due to increased concentrations of Al^{3+} (Figures 3-5-9 and 3-5-10).

Precipitation and dissolution processes result in a nonuniform porosity distribution across the model domain. The sharp discontinuity in porosity (Figure 3-5-8) that occurs at 500 and 1,000 years in the downstream region is caused by a dolomite precipitation front (Figure 3-5-12) at this location. The small fluctuations in porosity in the downstream region are due to slight precipitation of dolomite and dissolution of anhydrite (Figure 3-5-13).

Solution pH decreases as a function of distance, as the CO_2-rich brine is transported through the domain. Figure 3-5-14 depicts the pH profile at various times. At a time of 1,000 years the pH profile has reached a steady-state value of 4.7.

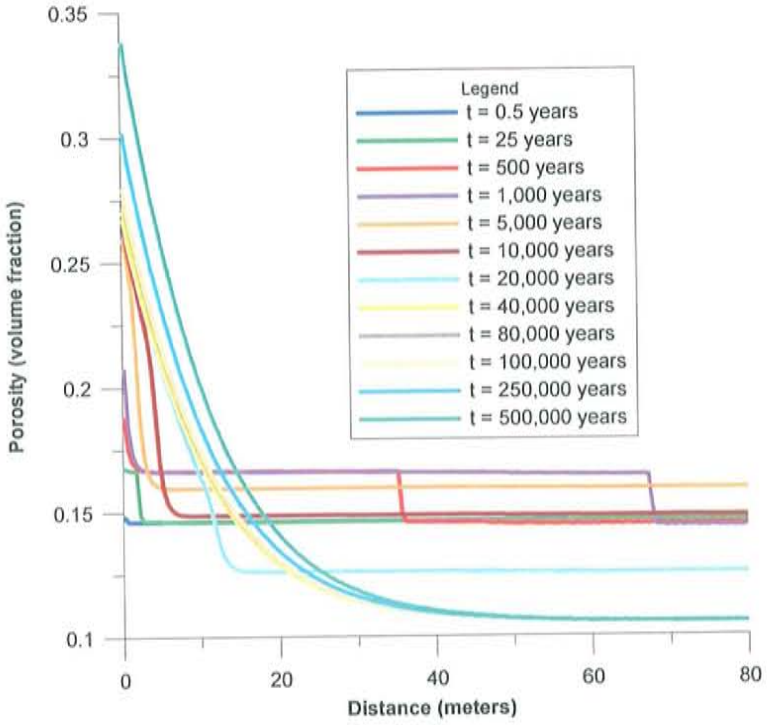

Figure 3-5-7: Porosity versus distance (Shattuck Sandstone, Stauffer case study).

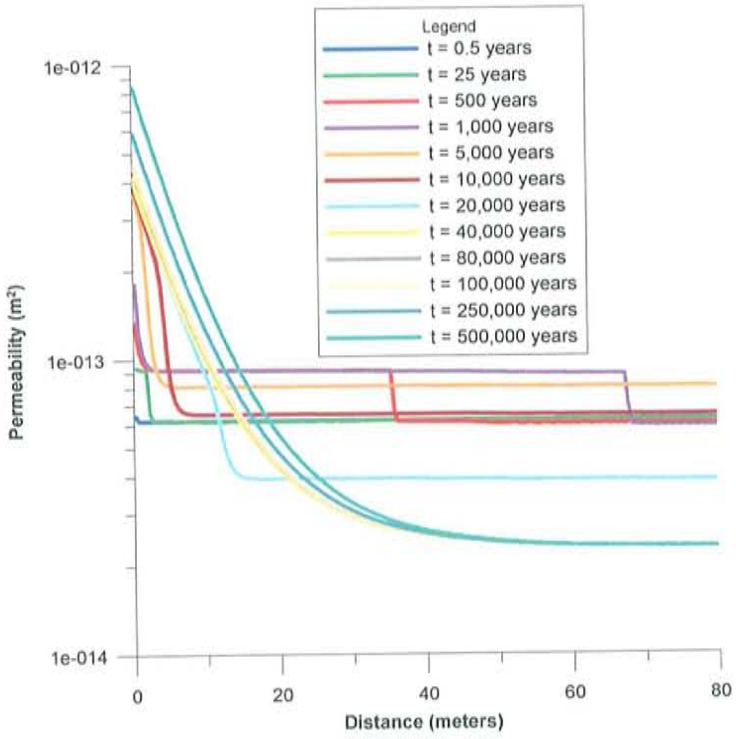

Figure 3-5-8: Permeability versus distance (Shattuck Sandstone, Stauffer case study).

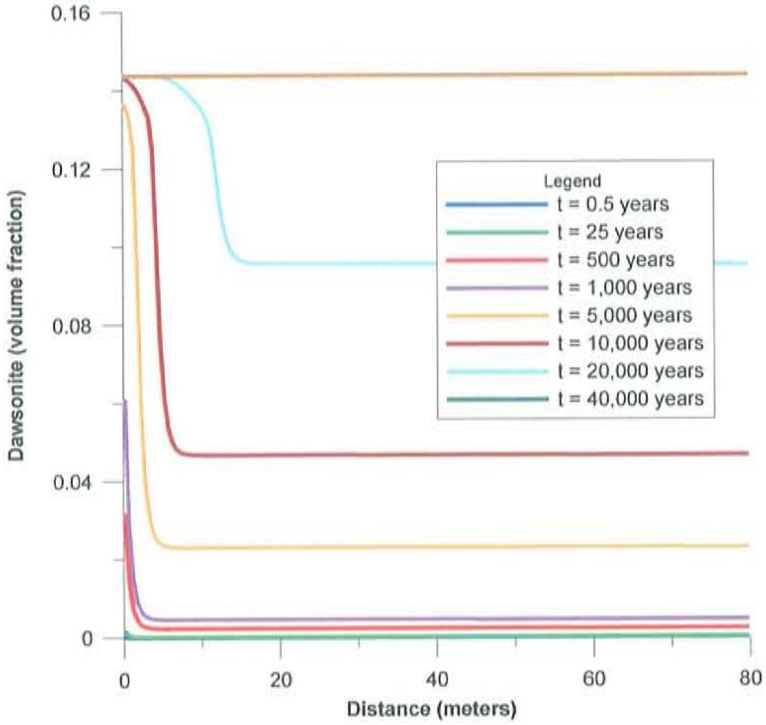

Figure 3-5-9: Dawsonite volume fraction versus distance (Shattuck Sandstone, Stauffer case study).

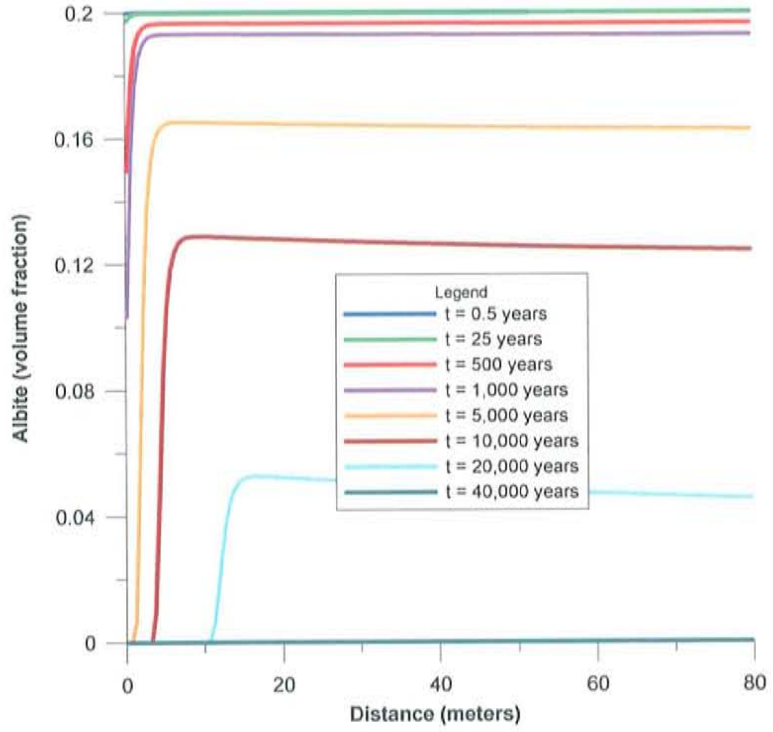

Figure 3-5-10: Albite volume fraction versus distance (Shattuck Sandstone, Stauffer case study).

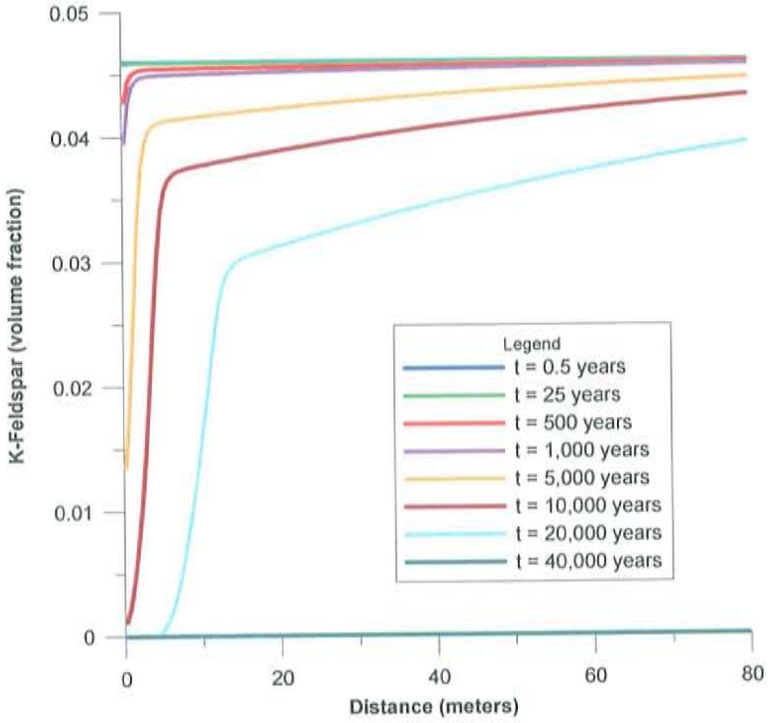

Figure 3-5-11: Potassium feldspar volume fraction versus distance (Shattuck Sandstone, Stauffer case study).

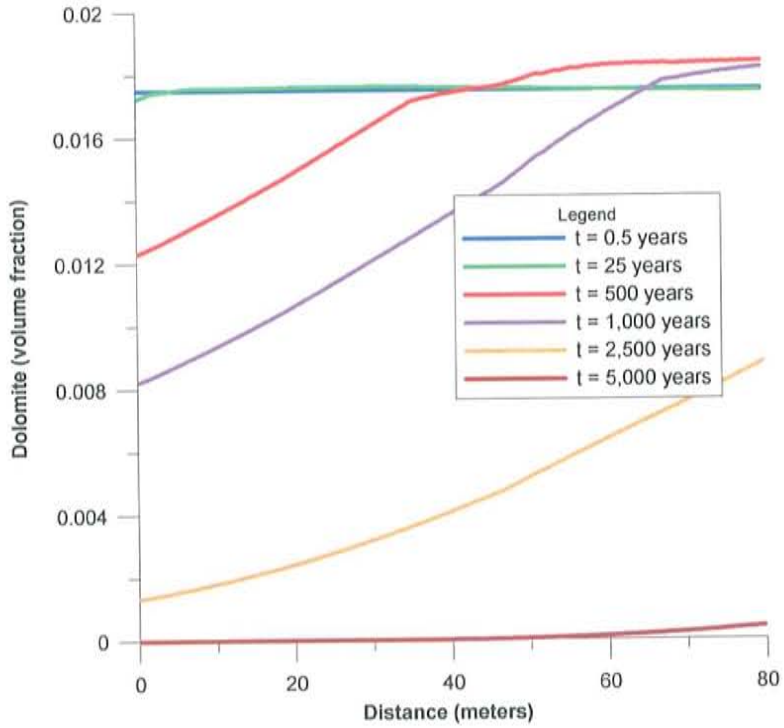

Figure 3-5-12: Dolomite volume fraction versus distance (Shattuck Sandstone, Stauffer case study).

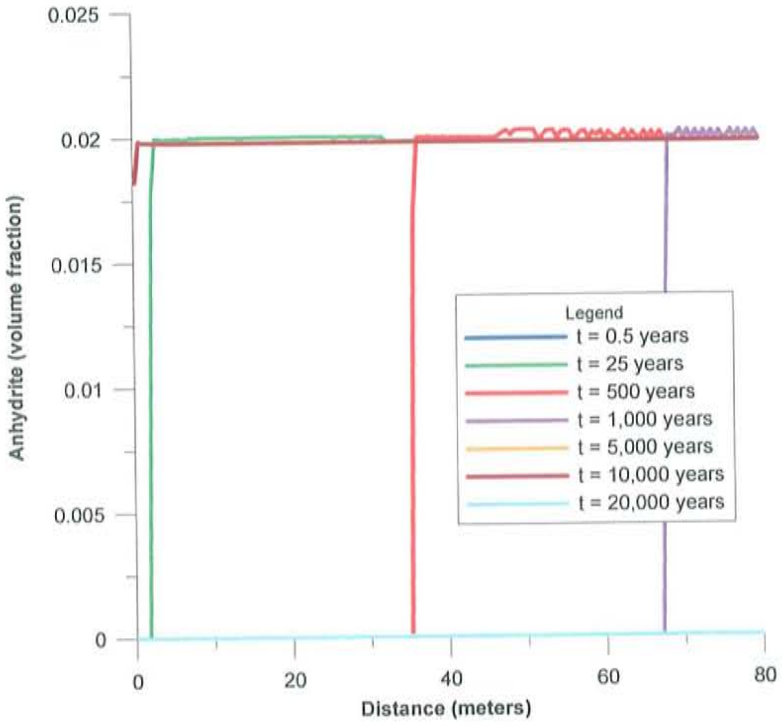

Figure 3-5-13: Anhydrite volume fraction versus distance (Shattuck Sandstone, Stauffer case study).

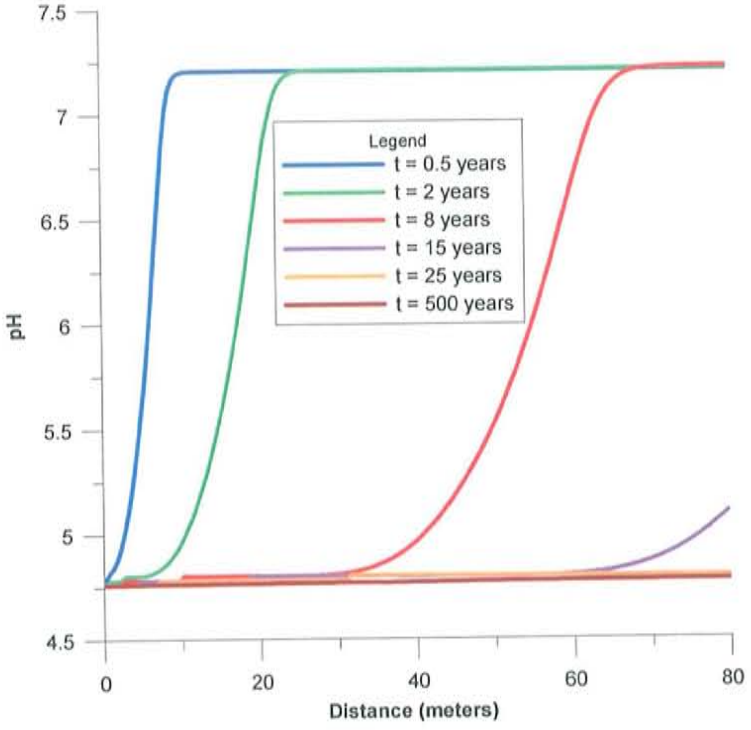

Figure 3-5-14: pH versus distance (Shattuck Sandstone, Stauffer case study).

One-dimensional reactive flow and transport simulations of CO_2-rich brine in the overlying Seven Rivers Formation show an increase in porosity over the domain length over 40,000 years (Figure 3-5-15). Major differences in bulk mineralogies between the Seven Rivers Formation and the Shattuck Sandstone include higher dolomite volume fractions (approximately 2 percent in the Shattuck Sandstone compared to approximately 19 percent in the Seven Rivers Formation). Additionally, the Seven Rivers Formation is dominated by anhydrite with bulk volume fractions of approximately 65 percent. Due to the low pH, CO_2-saturated brine solution and the soluble evaporitic minerals, a dissolution-dominated reactive system is predicted. A dissolution-dominated system is confirmed in the results of the one-dimensional reactive flow and transport simulations of CO_2-rich brine in the Seven Rivers Formation. Porosity increases from approximately 7.1 percent by volume, initially, to approximately 29 percent by volume after 40,000 years (Figure 3-5-15).

Due to this increase in porosity, permeability is predicted to increase approximately 2 orders of magnitude from approximately 3×10^{-15} m^2, initially, to approximately 2×10^{-13} m^2 after 40,000 years, following Equation 3-5-2 (Figure 3-5-16). A small percentage of dawsonite (approximately 2.5 percent volume fraction) is predicted to form over the domain length within the simulation time (Figure 3-5-17) due to the dissolution of potassium feldspar (approximately 4.6 percent volume fraction) over the simulation period (Figure 3-5-18). Slight dissolution of anhydrite occurs over the model domain during the simulation period, whereby approximately 1.0 percent volume fraction of anhydrite is dissolved over the model domain (Figure 3-5-19). Dolomite is predicted to dissolve completely from the system after approximately 20,000 years (Figure 3-5-20),

which is the main dissolution process to increase porosity and permeability of the Seven Rivers Formation.

Solution pH decreases in the Seven Rivers Formation as a function of distance, similarly to the Shattuck Sandstone, as the CO_2-rich brine is transported through the domain. Figure 3-5-21 depicts the pH profile at various times within the Seven River Formation simulation.

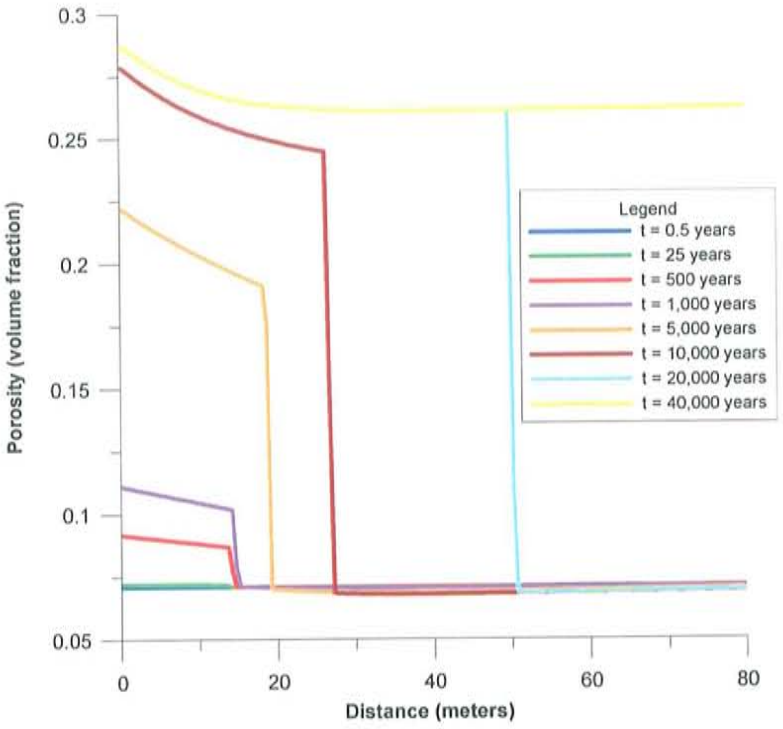

Figure 3-5-15: Porosity versus distance (Seven Rivers Formation, Stauffer case study).

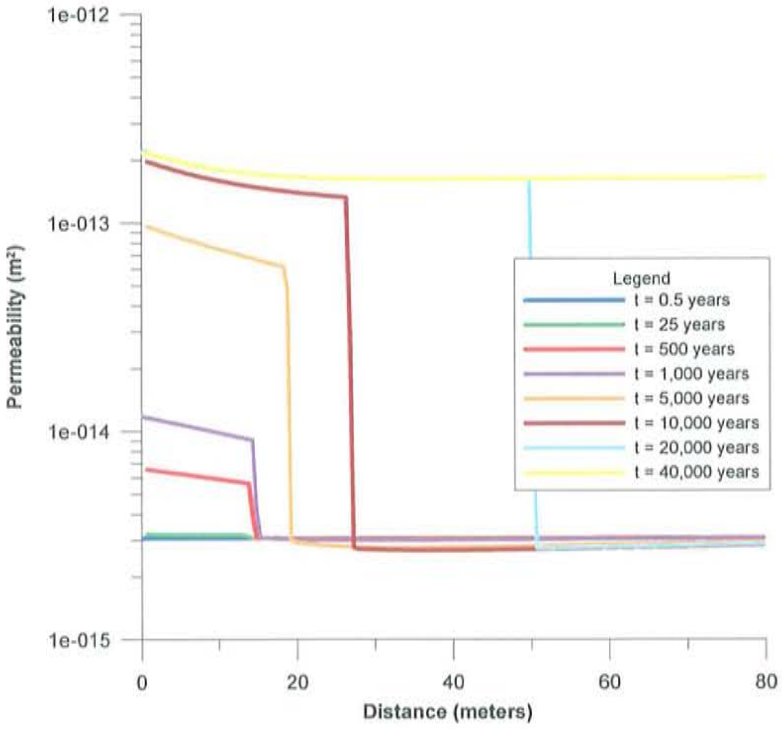

Figure 3-5-16: Permeability versus distance (Seven Rivers Formation, Stauffer case study).

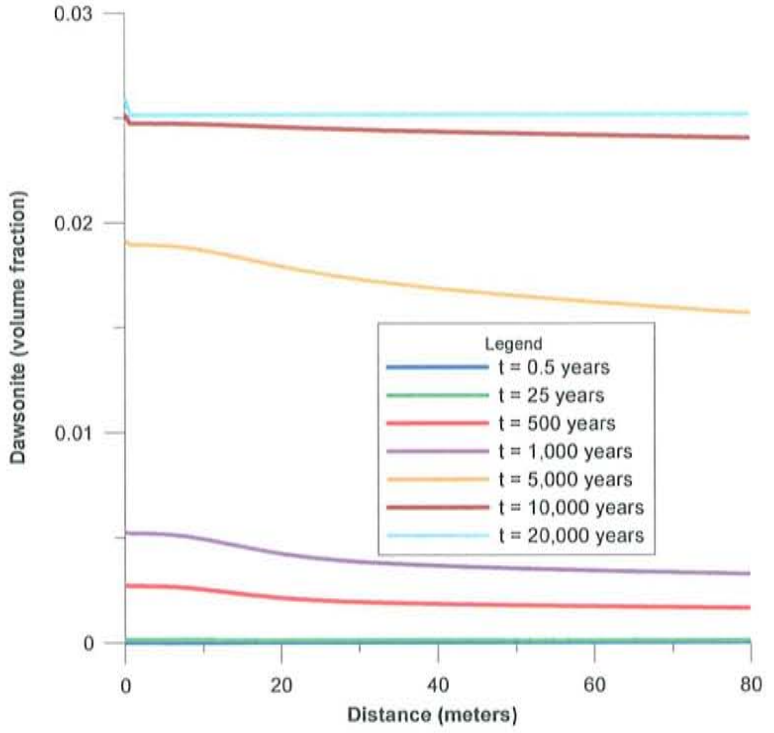

Figure 3-5-17: Dawsonite volume fraction versus distance (Seven Rivers Formation, Stauffer case study).

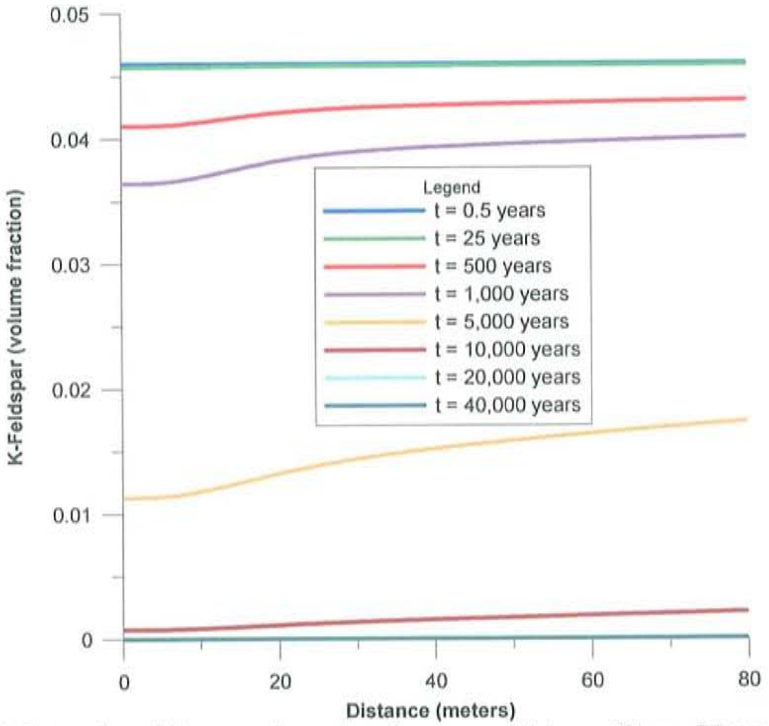

Figure 3-5-18: Potassium feldspar volume fraction versus distance (Seven Rivers Formation, Stauffer case study).

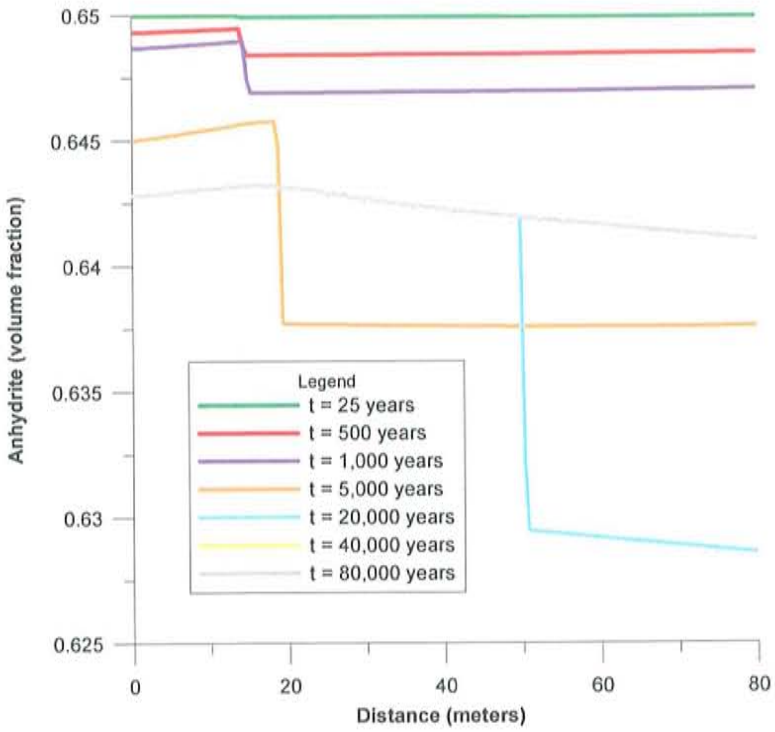

Figure 3-5-19: Anhydrite volume fraction versus distance (Seven Rivers Formation, Stauffer case study).

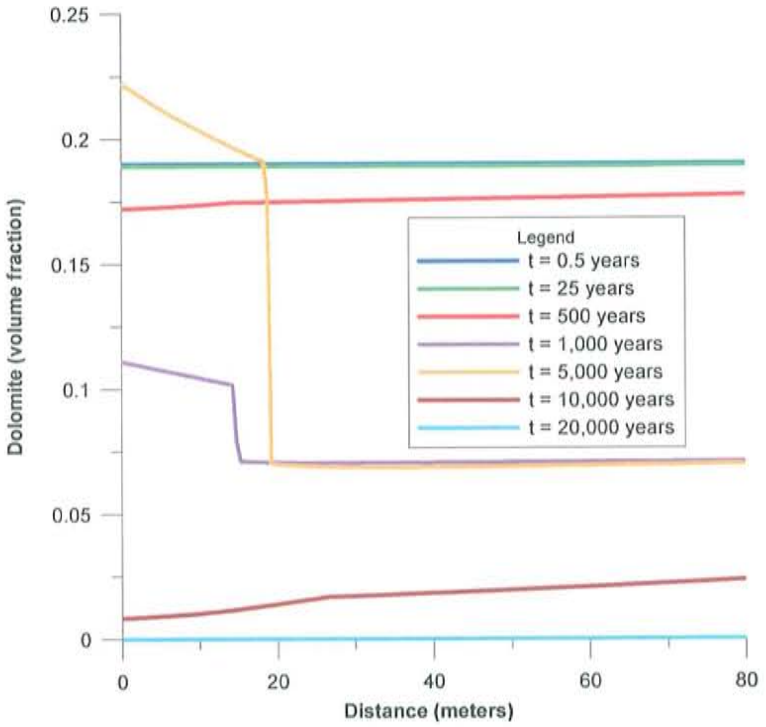

Figure 3-5-20: Dolomite volume fraction versus distance (Seven Rivers Formation, Stauffer case study).

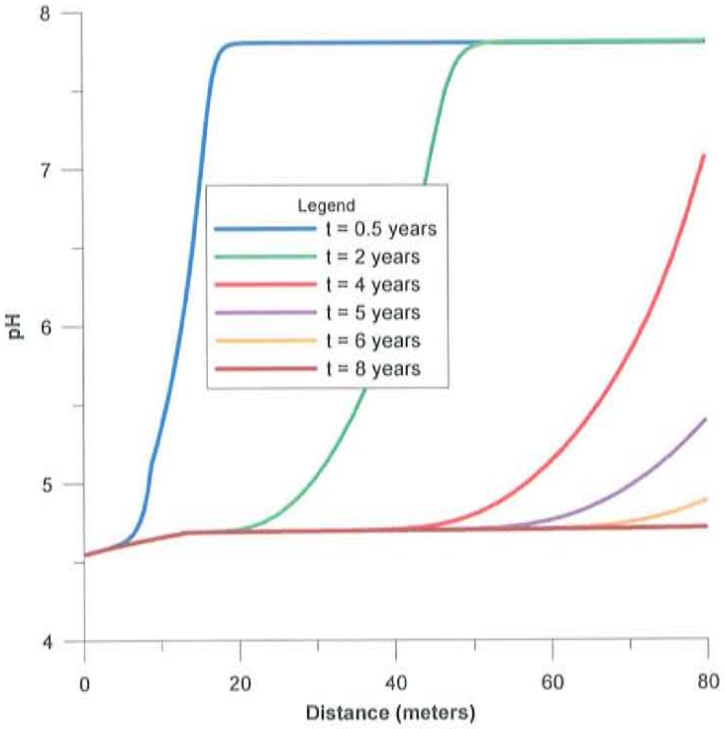

Figure 3-5-21: pH versus distance (Seven Rivers Formation, Stauffer case study).

3.5.2 EFFECT OF TEMPERATURE ON DAWSONITE PRECIPITATION

Further analyses on dawsonite stability were performed to determine if temperature has a significant effect on dawsonite precipitation. Dawsonite activity diagrams were constructed to determine dawsonite stability under various activities of species in solution. Figures 3-5-22 and 3-5-23 depict the dawsonite stability as a function of Al^{3+} and $CO_{2(aq)}$ vs. pH at 45°C.

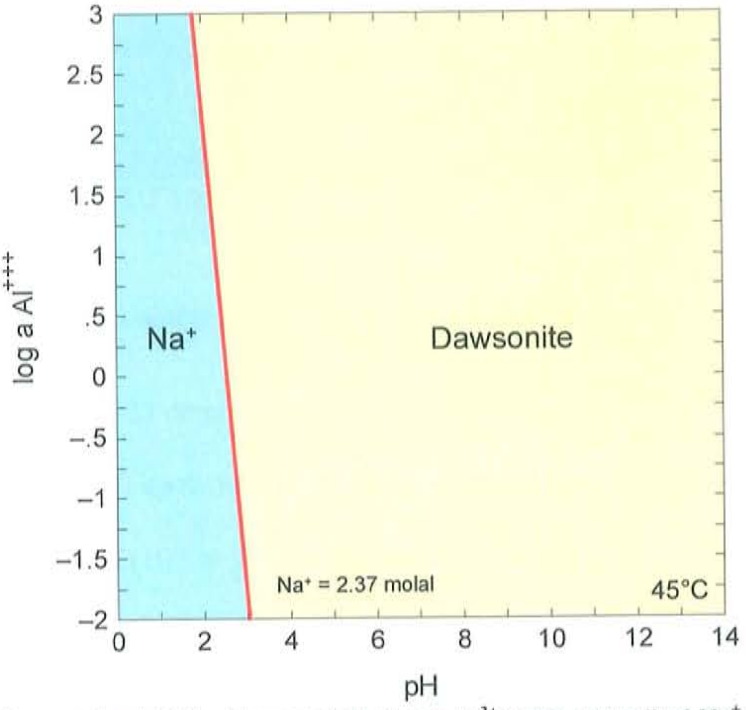

Figure 3-5-22: Dawsonite stability diagram (pH vs. log Al^{3+}) with prescribed Na^+ activity.

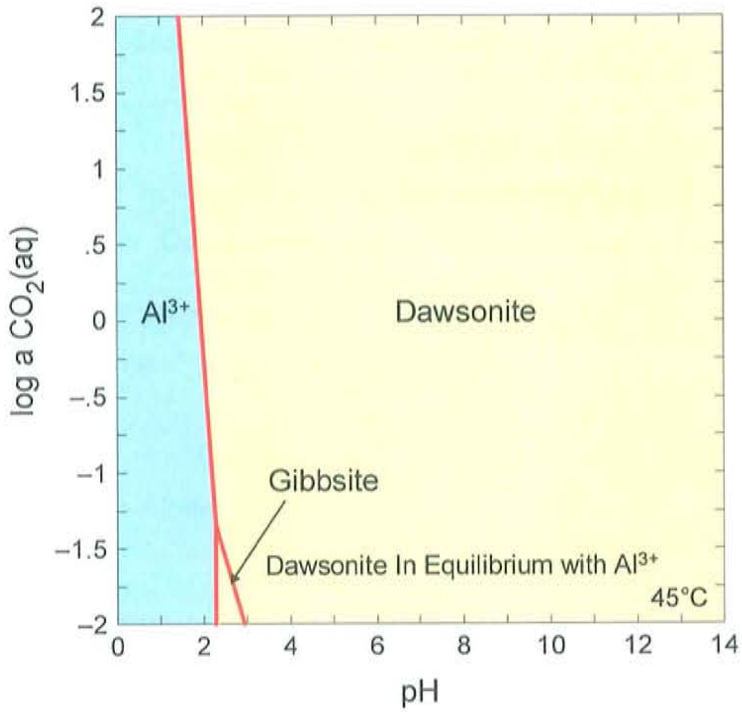

Figure 3-5-23: Dawsonite stability diagram (pH vs. log CO_2(aq)) with prescribed Al^{3+} activity.

Figures 3-5-22 and 3-5-23 demonstrate that dawsonite is stable at pH values ranging from approximately 3.0 up to 14.0 at 45°C. A transition from gibbsite is noted at relatively low $CO_{2(aq)}$ activities (10^{-2} to $10^{-1.2}$). Dawsonite stability increases with increasing $CO_{2(aq)}$ and Al^{3+} activities (Figure 3-5-22 and 3-5-23). Temperature has a profound effect on the stability of dawsonite. Figures 3-5-24 through 3-5-27 provide simulation results that illustrate the influence of increasing temperature on dawsonite precipitation.

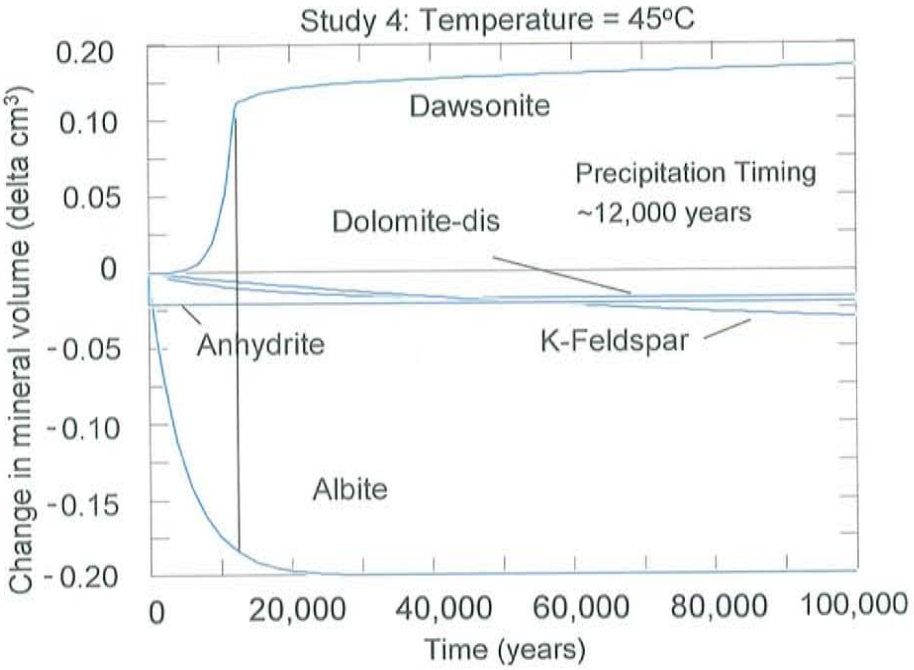

Figure 3-5-24: Reaction path model of the Shattuck Sandstone at T = 45 °C.

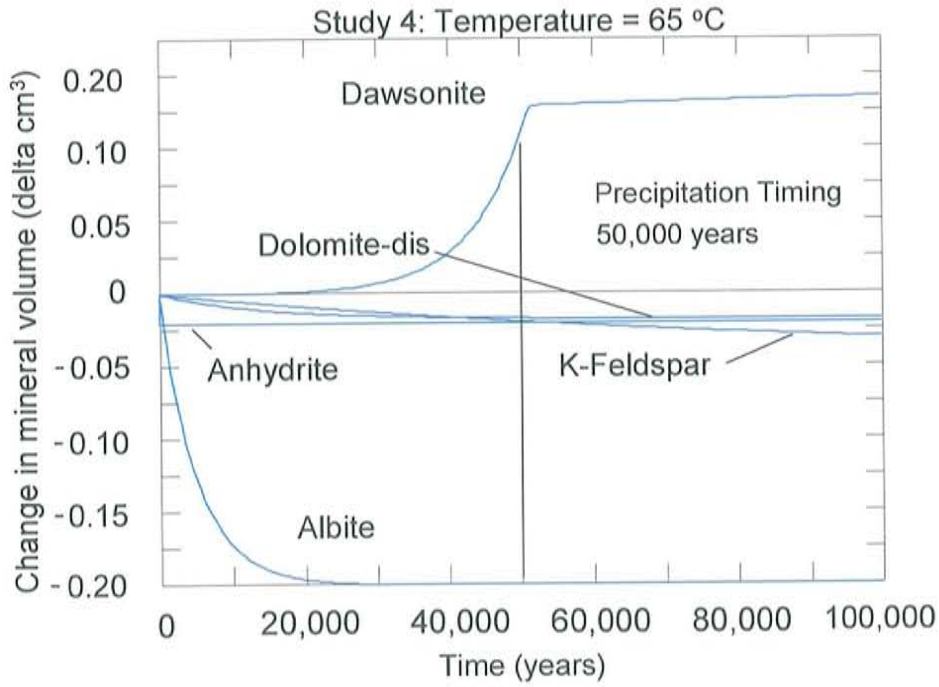

Figure 3-5-25: Reaction path model of the Shattuck Sandstone at T = 65 °C.

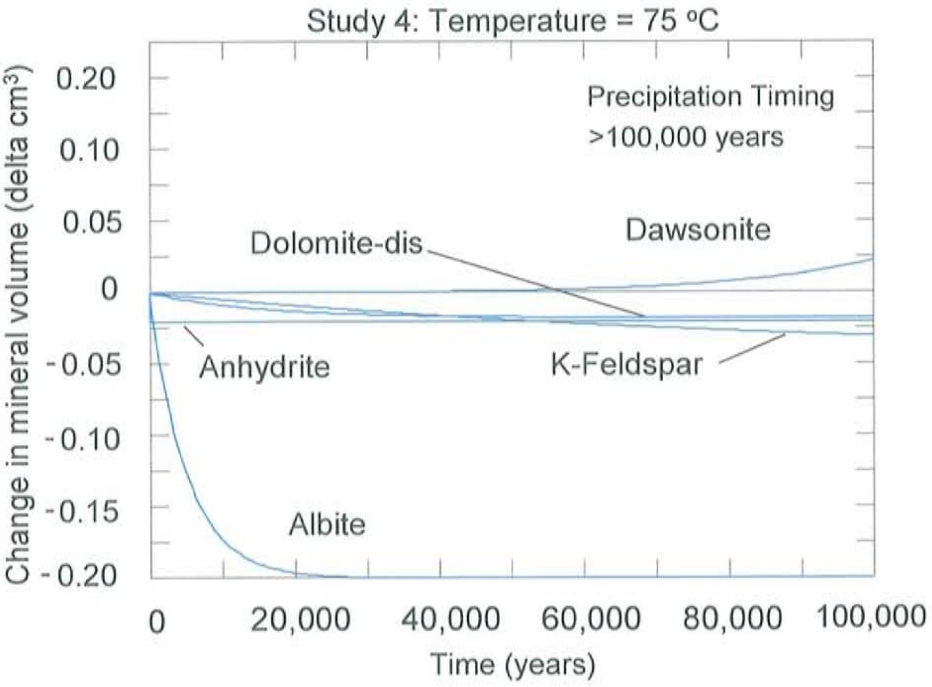

Figure 3-5-26: Reaction path model of the Shattuck Sandstone at T = 75 °C.

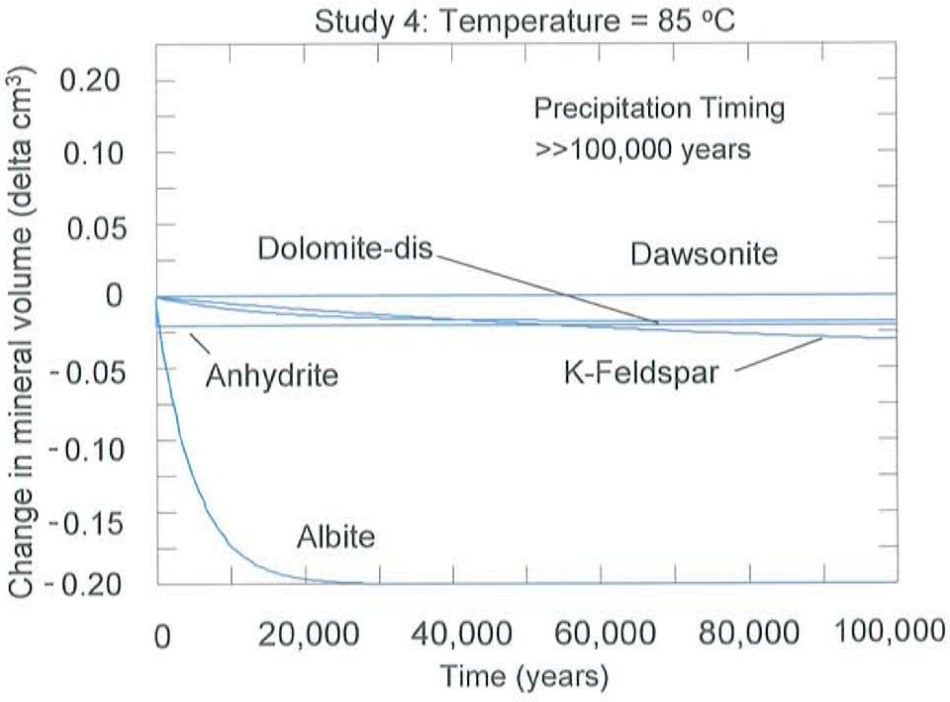

Figure 3-5-27: Reaction path model of the Shattuck Sandstone at T = 85 °C.

As temperature increases from 45°C (Figure 3-5-24) to 65°C (Figure 3-5-25), dawsonite precipitation timing increases by approximately 38,000 years (to ~ 50,000 years). At a temperature of 75°C, dawsonite precipitation diminishes greatly (Figure 3-5-26). After 100,000 years simulation time, an increase in dawsonite mineral volume of 0.025 cm^3 is observed. This is much less than the 0.12 cm^3 change that resulted in the 45°C simulation. The 85°C simulation demonstrates no increase in dawsonite mineral volume during the 100,000-year simulation period (Figure 3-5-27).

These reaction path simulations indicate reduced dawsonite precipitation as temperature is increased within the system. The cause of this decrease in dawsonite precipitation may be explained by temperature stability diagrams for dawsonite. TACT, a module in Geochemist's Workbench™ was used to construct temperature stability diagrams. Brine compositions from Shattuck Sandstone were prescribed in TACT, and a temperature range of 0°C to 200°C was applied. The Shattuck Sandstone brine composition refers to the case with injected CO_2, thus these diagrams are created with certain exceptions (e.g., variable pH, Al^{3+}, etc.). Stability limits were calculated based on the equilibrium constants for a given temperature. Figures 3-5-28 through 3-5-31 show temperature stability diagrams for various Al^{3+} concentrations in Shattuck Sandstone brine (Table 3-5-1).

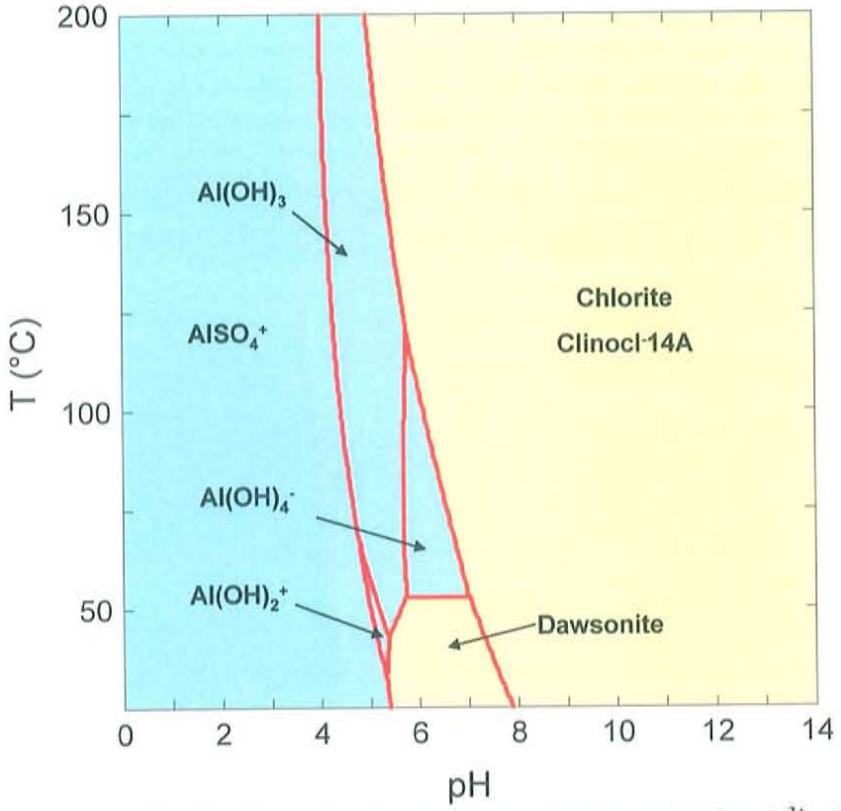

Figure 3-5-28: Temperature stability diagram for the Shattuck Sandstone brine (log Al^{3+}=-10).

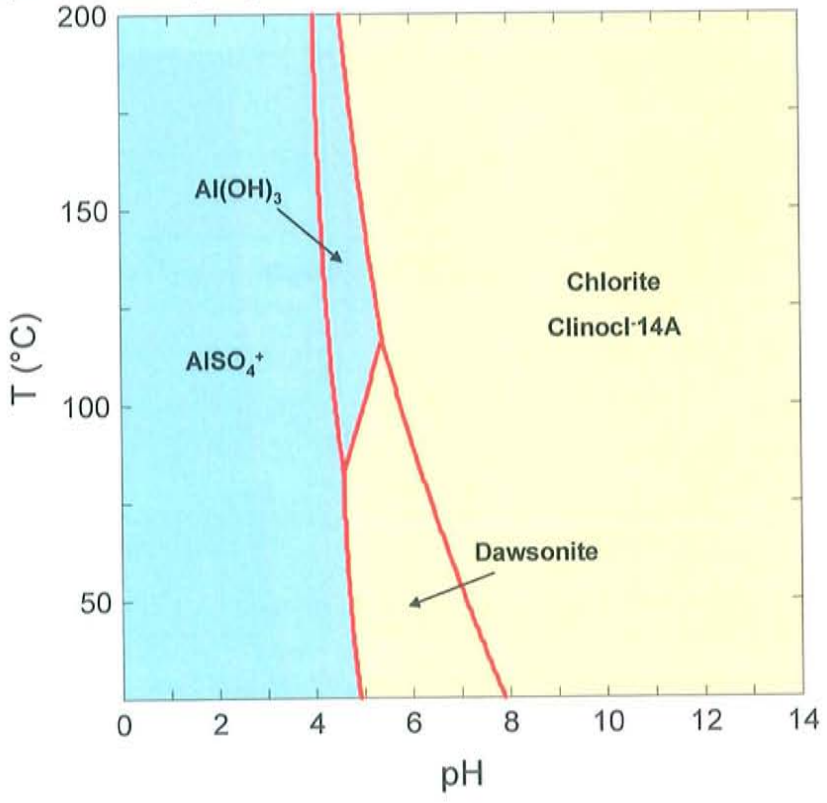

Figure 3-5-29: Temperature stability diagram for the Shattuck Sandstone brine (log Al^{3+}=-8).

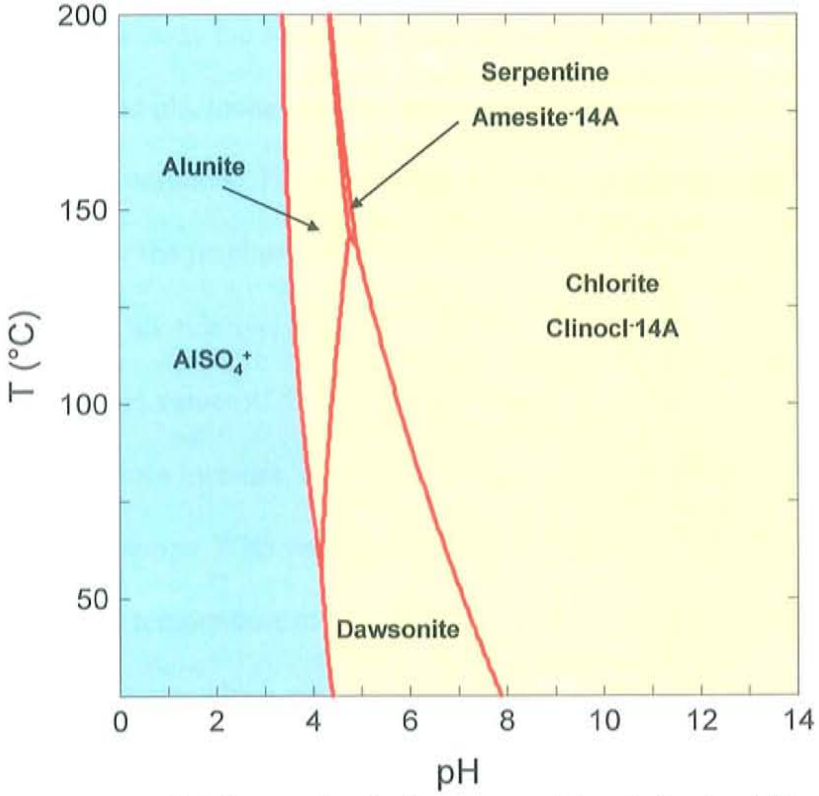

Figure 3-5-30: Temperature stability diagram for the Shattuck Sandstone brine (log Al^{3+}=-6).

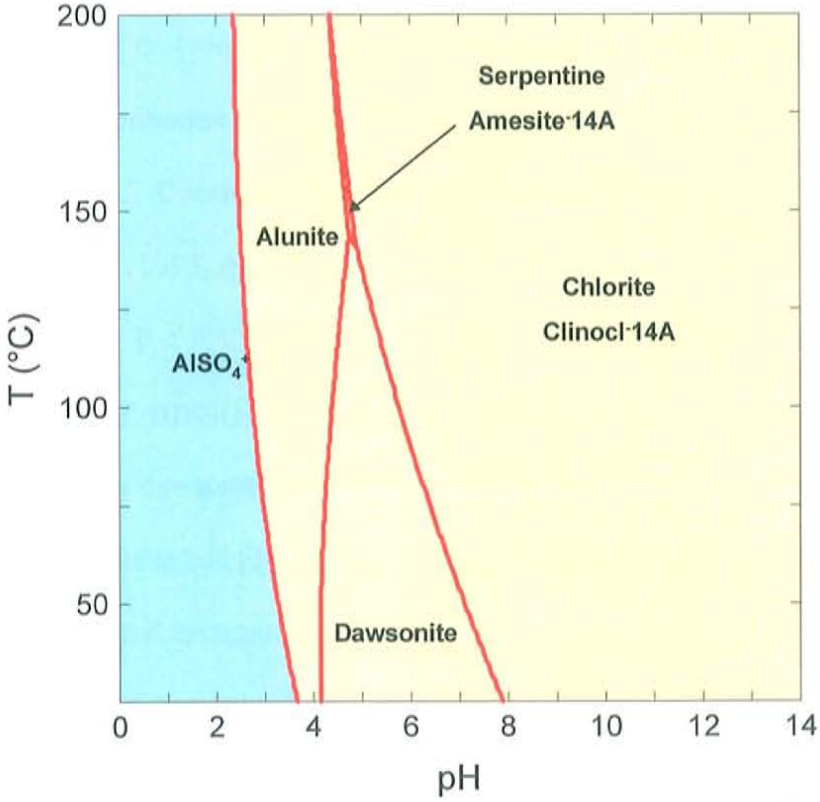

Figure 3-5-31: Temperature stability diagram for the Shattuck Sandstone brine (log Al^{3+}=-4).

These diagrams illustrate the stabilities of certain species and minerals as a function of temperature and pH, including the evolution of dawsonite stability as Al^{3+} concentrations increase in solution. The dissolution of aluminum silicates increases Al^{3+} in solution as suggested by the reaction path simulations (Figures 3-5-28 through 3-5-31). When Al^{3+} concentrations are relatively low (prior to aluminum silicate dissolution), dawsonite is stable from pH values of 5.3 to 8.0 and temperatures up to approximately 55°C. As Al^{3+} concentrations increase, dawsonite becomes stable at lower pH values (~ 4.0) and at higher temperatures. With very high Al^{3+} concentrations (log Al^{3+}= -4), dawsonite is stable up to a temperature of approximately 145°C. At this temperature, dawsonite stability is constrained by a very narrow pH range ($5.0 < pH < 5.4$). pH is constrained in these temperature stability diagrams due to the prescribed aluminum (Al^{3+}) concentrations. As aluminum increases in solution dawsonite stability related to pH as increases. The stability of dawsonite indicated by these temperature stability diagrams suggests that dawsonite formation under natural conditions is probably limited to temperatures below 100°C. Consistent with this are results of the diagenetic study performed by Baker et al. (1995) that showed dawsonite formation occurred in relatively low temperatures ($25°C < T < 75°C$) in basins of eastern Australia Palandri (2004).

3.6 TIMING OF PLUME DISSOLUTION AND MIGRATION

A detailed study of dawsonite precipitation with respect to the West Pearl Queen Reservoir case study has been completed. To constrain the likelihood of separate-phase CO_2 trapping, the timing and extent of the CO_2 plume dissolution and migration following injection must be determined.

The numerical flow and transport simulator, TOUGH2 (Pruess and Moridis, 1999), was used to examine the timing of the separate-phase CO_2 plume specific to the West Pearl Queen Reservoir. Details concerning the CO_2 equation of state (EOS) used in this study can be found in Cole (1999), who assembled the EOS algorithm. Two-dimensional numerical meshes were developed similar to those of a previous numerical modeling study of the West Pearl Queen Reservoir (Pawar et al., 2003). A sensitivity analysis was formulated, as explained in Appendix A. Permeability values of the Shattuck Sandstone and the overlying Seven Rivers Formation were varied to examine possible separate-phase CO_2 residence times within the reservoir. (Appendix A). Results of the separate-phase CO_2 timing study reveal that the vertical permeability of the Shattuck Sandstone and the Seven Rivers Formation are the controlling parameters. Simulations based on low vertical permeabilities (simulation 4) for the Seven Rivers Formation resulted in long separate-phase CO_2 residence times (900 years) and a smaller horizontal plume extent (322 m) (Appendix A). Residence times within the Seven Rivers Formation ranged between 4 years in the high-permeability case (simulation 1) to 900 years in the low-permeability case (simulation 4). Separate-phase CO_2 residence times within the Shattuck Sandstone ranged from 1 year in the high-permeability case (simulation 1) to 70 years in the low-permeability case (simulation 4).

3.6.1 FRINGE MINERALIZATION TIMING VERSUS PLUME MIGRATION TIMING

Dawsonite precipitation times within the West Pearl Queen Reservoir vary from less than 2 years up to >100,000 years. The primary control for dawsonite formation is the dissolution rate constants for aluminum silicates, as previously discussed. No evidence exists that provides dawsonite precipitation timing in natural geologic settings.

Error induced by the large discrepancies among kinetic rate constants causes significant uncertainty in the evaluation of dawsonite precipitation times. Due to the large variation in the predicted precipitation timing, it is very difficult to make an accurate evaluation of fringe mineralization trapping for the West Pearl Queen Reservoir pilot injection test.

3.6.2 KINETIC REACTION RATE UNCERTAINTIES

The primary uncertainty associated with the timing of dawsonite mineralization pertains to the dissolution rates of available aluminum silicate minerals to provide aluminum ions (Al^{3+}) in solution, and the mineralization (precipitation) reaction rates associated with the formation of dawsonite. Kinetic dissolution reaction rates of aluminum silicate minerals in previous studies associated with reactive transport models of CO_2 vary over approximately 4 orders of magnitude (1×10^{-17} moles/cm^2-sec. to 1.62×10^{-13} moles/cm^2-sec.) (See Table 3-5-5 (a) and (b)). Furthermore, dawsonite precipitation reaction rates vary over 5 orders of magnitude (1.0×10^{-16} moles/cm^2-sec. to 1.38×10^{-11} moles/cm^2-sec.) (See Table 3-5-5 (a) and (b)).

Previously cited kinetic studies used for the parameterization for the current study (Gaus et al., 2003, Xu and Pruess, 2001, and Johnson et al., 2001) cited Blum and Stillings, 1995, for the source of the aluminum silicate (potassium feldspar and albite) dissolution kinetic rate data. Further research into the source of these dissolution kinetic rate data indicated kinetic reaction rates were in fact determined by Stillings and Brantley (1995) through steady-state dissolution batch reactions using sieved feldspar powders with particle sizes ranging between 75 and 150 μm (Stillings and Brantley, 1995). Molar feldspar dissolution reaction rates were calculated in these studies from the following relationship:

$$R_j = \frac{Q \cdot C_j}{A_t \cdot M_t \cdot \nu_j},$$ Eq. 3-6-1

where R_j = the feldspar dissolution rate at time t (moles feldspar $cm^{-2}s^{-1}$) calculated from component j (Si, Al, Na, Ca, or K), Q = the flow rate, and C_j = steady-state concentration of component j (mole/L). A_t is the specific surface area (cm^2/g) at time t and is based on the following linear time-dependent relationship for

$$A_t = \left(\frac{A_f - A_i}{T} \right) \cdot t + A_i,$$

A_f = final specific surface area (cm^2 / g)

increase in surface area: A_i = initial specific surface area (cm^2 / g)

T = total duration of the steady-state experiment (hrs.)

t = time of sample collected (hr.)

Eq. 3-6-2

This equation assumes that the surface area changes linearly with time. Additionally, correction of time-dependent decrease in mass is estimated from silica (Si) concentrations by the following relationship.

$$M_t = M_i - \left(\frac{\sum_t C_{Si,t}}{\nu_{Si}} \cdot F \right),$$

M_t = sample mass at time t (grams)

M_i = initial sample mass (grams)

$C_{Si,t}$ = cumulative moles of Si leached from the feldspar by time t

ν_{Si} = the stoichiometric coefficient of Si in the formula unit

F = the feldspar formula weight

Eq. 3-6-3

The estimated error associated with kinetic reaction rates of feldspar dissolution in the Stillings and Brantley (1995) study was reported as being between 12 and 27 percent.

Dawsonite kinetic reaction rates have not been confirmed or studied, thus, kinetic reaction rates for dawsonite have typically consisted of assumed intermediate kinetic reaction rates between those of calcite and dolomite (Gaus et al., 2003) or between those of calcite and magnesite (Johnson et al, 2001). Detailed laboratory analyses relating to kinetic reaction rates of dawsonite formation are needed to parameterize reactive transport models accurately.

3.7 CONCLUSIONS AND IMPLICATIONS

If we assume that silicate dissolution and dawsonite precipitation follow the timescales observed in Gaus et al. (2003) (Table 3-5-7), then dawsonite precipitation may cause PFM in certain reservoirs. However, based on parameterized batch experiments within the West Pearl Queen Reservoir, a better estimate of reactive surface areas provide a more accurate dawsonite precipitation timing in excess of 100,000 years and indicate that entrapment of the supercritical CO_2 plume will depend on the permeability of the Shattuck Sandstone and the permeability of the overlying Seven Rivers Formation. Table 3-7-1 summarizes results for separate-phase CO_2 residence times within the West Pearl Queen Reservoir simulated in TOUGH2-EOSCO2 (Appendix A). The term "separate-phase CO_2 residence times" is defined as the time scale in which separate-phase CO_2 remains in a particular reservoir or geologic compartment. Simulations with varying vertical and horizontal permeabilities resulted in very different residence times for the Shattuck Sandstone and the Seven Rivers Formation. Simulations 1 through 3 (Table 3-7-1) depicted much lower residence times (time at which separate-phase CO_2 mass fraction approaches zero in the vicinity of CO_2 injection) in both the Shattuck Sandstone and Seven Rivers Formation. Simulation 4 displayed the greatest residence times in each unit due to decreased permeabilities in the Seven Rivers Formation (Table 3-7-1).

Separate phase CO_2 residence times

Simulation	Shattuck Sandstone Time (years)	Seven Rivers Formation Time (years)
1	1	4
2	1	4
3	1	4
4	70	900

Note: Simulation 4 parameters
Shattuck Sandstone: $k_h = 4.0 \times 10^{-16}$ m^2, $k_v = 2.0 \times 10^{-17}$ m^2
Seven Rivers Fm.: $k_h = 2.0 \times 10^{-18}$ m^2, $k_v = 2.0 \times 10^{-19}$ m^2
Mineralization trapping likely

Table 3-7-1: Summary of separate-phase CO_2 residence times within the West Pearl Queen Reservoir.

Low permeabilities result in longer residence times of the separate-phase CO_2 and thus an opportunity for dawsonite mineralization to reduce porosity and permeability for further trapping. Dawsonite precipitation timescales on the order of 2 years (Table 3-5-3) are then much less than those for separate-phase CO_2 plume migration out of the Shattuck Sandstone (Table 3-7-1). In the scenario of low-permeability cap rock units and arkosic sandstone targets as in the West Pearl Queen Reservoir, fringe mineralization may play a significant role for plume entrapment. However, the West Pearl Queen Reservoir contains a feldspar-poor cap rock that shows a dissolution-dominated regime with respect to CO_2-rich brines (Figures 3-5-15 and 3-5-21). Sealing integrity of this unit degrades in time via dissolution of anhydrite and dolomite.

One of the most uncertain points in this study is the timing of dawsonite precipitation due to differing kinetic rate constants of aluminum silicate minerals and dawsonite. Kinetic dissolution reaction rates of aluminum silicate minerals obtained from previous studies associated with reactive transport models of CO_2 vary over approximately 4 orders of magnitude (1×10^{-17} moles/cm^2-sec. to 1.62×10^{-13} moles/cm^2-sec.) (See Table 3-5-5 (a) and (b)). Furthermore, dawsonite precipitation

reaction rates vary over 5 orders of magnitude (1.0×10^{-16} moles/cm^2-sec. to 1.38×10^{-11} moles/cm^2-sec.) (See Table 3-5-5 (a) and (b)). Future studies concerning the timing of dawsonite precipitation or any active mineralization process in the context of CO_2 sequestration should include detailed rate studies including both laboratory batch experiments and flow-through experiments to constrain kinetic reaction rates, specific surface areas, and transient (non-equilibrium) conditions. Data from such analyses should then be used to calibrate reactive transport simulations of active sequestration sites. Prior kinetic reaction rate studies for feldspar dissolution reaction rates utilized sieved powder material masses in steady-state dissolution laboratory experiments that potentially could overestimate dissolution reaction rates of feldspar minerals. Permeability changes due to mineralization may be used to calibrate reactive transport models. Ultimately, permeability changes on the core-scale may be used to predict changes on the well and basin scales. This methodology should be used in the evaluation of potential CO_2 repository sites.

These results suggest important implications for possible CO_2 sequestration in other geological settings. Some geologic settings where CO_2 plume trapping through fringe mineralization may apply include the following:

- Reservoirs which include feldspar-rich shales as cap rock units
- Dipping arkosic sandstone reservoirs with updip feldspar-rich shale traps
- Reservoirs with temperatures less than 100 °C (ideal for dawsonite formation)
- Arkosic sandstone reservoirs with moderate permeability

All of these reservoirs have some characteristics that promote long residence times for separate-phase CO_2. Reservoirs with feldspar-rich minerals would likely exhibit increased cap rock integrity by mineralization, unlike the West Pearl Queen Reservoir. Dipping arkosic sandstone reservoirs with updip feldspar-rich shale traps would likely provide similar increased rock integrity scenarios. Adequate characterization of potential reservoirs, detailed laboratory geochemical experiments, and CO_2 flow and transport modeling may all be used in conjunction to assess the possibility of CO_2 plume trapping through mineralization.

Important results of this study include:

- Conditions for natural dawsonite formation include temperatures below 100°C and increased dissolved CO_2 mainly due to magmatic sources or hydrocarbon generation.

- Dawsonite precipitation is strongly coupled to the dissolution of aluminum silicates which provides Al^{3+} in solution.

- Published feldspar kinetic reaction rates are based on steady-state dissolution laboratory experiments that utilized sieved powder feldspar samples, which may overestimate actual dissolution reaction rates and in turn will affect the amount of aluminum (Al^{3+}) ions in solution and dawsonite stability.

- Dawsonite precipitation time varies over ~ 3 orders of magnitude dependent on kinetic rate constants of aluminum silicate minerals and dawsonite.

- CO_2 plume trapping through fringe mineralization may occur within reservoirs that exhibit long separate-phase CO_2 residence times and abundance of feldspar-rich minerals (e.g. arkosic sandstones). The name coined for this process is "Plume Fringe Mineralization (PFM)" which may be a significant process in geologic CO_2 sequestration.

- Significant short-term porosity and permeability changes due to mineralization may influence flow heterogeneities such as redirecting flow paths of separate-phase CO_2 (profile control).

CHAPTER 4:

CONCLUSIONS AND FUTURE RESEARCH

The increase of global mean temperature over the last several hundred years has heightened awareness concerning global greenhouse gas emissions. Carbon dioxide emissions are of particular concern due to the increased abundance of this gas in the atmosphere since the industrial revolution. Curtailing anthropogenic CO_2 emissions is one solution. Technologic advances in fuel cells and renewable energy sources have been made, but the ultimate economic impact of changing to such technologies is currently uncertain. Sequestering carbon in multiple forms is another option, and was the main focus for this study.

4.1 GOALS

Major goals of this study included the evaluation of potential sequestration capacities of surface and subsurface mineralization processes (above-ground mineralization versus "solubility trapping"). We considered surface mineralization approaches (summarized by Bond et al., 1999 and 2001), direct subsurface injection of CO_2 as well as bicarbonate-rich brines, and examined the carbon capacities of these methods. The Permian Basin was chosen as the case study for the comparison. Conservative estimates of carbon precipitated as a solid form (calcium and magnesium carbonate) were calculated using produced waters as the source of divalent calcium and magnesium ions. These estimates of surface mineralization carbon capacity were

compared to potential subsurface storage potential via direct CO_2 injection in oil and gas reservoirs.

Compelling results are associated with both surface mineralization approaches (Bond et al., 2003 and 2004) and direct subsurface injection approaches. With regard to direct subsurface injection, significant physical and chemical effects may be induced by the injection of any fluid that differs from the resident formation fluid. Brine in the vicinity of the supercritical CO_2 plume becomes enriched with dissolved $CO_{2(aq)}$, possibly promoting various chemical reactions with reservoir minerals. Experimental and model results suggest rock porosities and permeabilities will be subject to the effects of significant dissolution and/or mineralization, ultimately leading to possible changes in reservoir hydrodynamics. Timing of mineralization and dissolution reactions is of particular importance for prediction of ultimate plume migration and sequestration.

4.2 MAJOR HYPOTHESES

We hypothesized that "Plume Fringe Mineralization" (PFM) will follow subsurface injection of CO_2 for sequestration into suitable types of reservoirs. We define PFM as mineralization that occurs at the interface between the separate-phase CO_2 plume and resident groundwater, where waters are enriched with dissolved CO_2. Flow rates, chemical kinetic relationships, reservoir heterogeneity and other conditions will determine whether a CO_2 plume will migrate or be trapped in place by PFM.

The second major hypothesis of this study was that sequestration by surface mineralization may be conducted at the surface for risk-free sequestration, with brines such as produced waters supplying the required cations.

The carbon capacities of such surface mineralization will be highly dependent upon the divalent cation concentrations of basin brines, the magnitude of ionic strengths in these brines, and the volume of brine produced.

4.3 MAJOR OBJECTIVES AND SUMMARY OF RESULTS

The first major objective of this study was to examine and compare surface mineralization capacities to dissolved CO_2 capacities in subsurface waters, with the Permian Basin as a case study. Based on Permian Basin brine composition and volume data from waters produced with oil and gas, we estimated that approximately 3 million metric tonnes of CO_2 could be stored (above surface) in carbonate form. Other calculations, in which estimated brine volumes and compositions are used to determine CO_2 solubility, suggest that approximately an additional 0.6 million tonnes of anthropogenic CO_2 may be stored in the subsurface as dissolved CO_2.

The second major objective was to analyze and quantify reactive processes, especially PFM, associated with direct injection of supercritical CO_2 in a typical sandstone reservoir. Kinetic reaction path modeling and reactive transport modeling techniques were used to examine possible changes in porosity and permeability of the reservoir. Two major tasks were carried out, in order to achieve this objective.

The first task included the development of hydrogeochemical models for evaluation of reaction paths and ultimate reservoir fate due to mineralization and dissolution reactions. A depleted oil and gas reservoir (West Pearl Queen Reservoir) undergoing a CO_2 pilot injection study was selected as a representative case example for study. Reservoir mineralogy, brine composition, and supercritical CO_2 injection rates for the West Pearl Queen Reservoir were available through ongoing sequestration research

projects at Los Alamos and Sandia National Laboratories. Based on reservoir thermodynamic conditions (temperature and pressure), equilibrium dissolved CO_2 concentrations in brine were calculated. Hydrogeochemical kinetic reaction path simulations were designed with dissolved CO_2 concentrations and reservoir mineralogy. A low-flow reservoir was assumed, with cases of local thermodynamic and chemical equilibrium.

Results of these kinetic reaction path and reactive transport simulations indicated marked changes in brine chemistry and reservoir mineralogy. Precipitation of dawsonite greatly influenced porosity within the CO_2 plume fringe. Decreases in reservoir porosity values on the order of 2 to 4 percent were predicted in the Shattuck Sandstone. However, dawsonite precipitation timing could not be constrained due to inconsistencies between literature values for the mineral kinetic rate constants and uncertainty in mineral surface areas. Previous reaction path modeling and reactive transport simulations relating to CO_2 sequestration cite kinetic dissolution reaction rates of aluminum silicate minerals that vary over approximately 4 orders of magnitude (1×10^{-17} moles/cm^2-sec. to 1.62×10^{-13} moles/cm^2-sec.) (See Table 3-5-5 (a) and (b)). The variation of kinetic reaction rates produces a variation of predicted dawsonite precipitation timing of approximately 3 orders of magnitude (less than 2 years up to approximately 12,000 years). Limited numbers of studies relating to feldspar dissolution kinetic reaction rates currently exist and the studies that are currently cited are based on steady-state batch dissolution reactions pertaining to sieved feldspar grains that range between 75 and 150 μm.

Additionally, dawsonite precipitation reaction rates have yet to be determined through laboratory experiments and currently are determined to be intermediate between those for calcite, dolomite, and magnesite (Gaus et al., 2003, Johnson et al, 2001).

The second major task involved the examination of CO_2 plume trapping through Plume Fringe Mineralization (PFM), specifically in the context of arkosic sandstone reservoirs. The origin, thermodynamic stability, and likely natural settings of dawsonite were examined. Results of this analysis indicated several possible reservoir settings ideal for CO_2 plume trapping. Reservoirs that promote long separate-phase CO_2 residence times have the highest potential for CO_2 plume trapping. Naturally dawsonite-prone reservoirs include low-temperature (typically less than 130°C) reservoirs with sources of CO_2. Common reservoirs of this type include deep magmatic or hydrocarbon-rich sources.

4.4 DISCUSSION AND CONCLUSIONS

Carbon sequestration by surface mineralization is feasible with produced waters as a cation source. The carbon capacities of surface mineralization are highly dependent upon the divalent cation concentrations of basin brines, the magnitude of ionic strength in those brines, and the volume of brine produced for a given basin. Furthermore, with regard to separate phase CO_2 injection, flow rates, chemical kinetic relationships, reservoir heterogeneity, and other conditions will determine whether a CO_2 plume will migrate or be trapped in place by PFM, which will affect the fate of the CO_2 injected.

Reactive transport processes and kinetic reaction paths of an actual CO_2 pilot injection test have been established. A process we call CO_2 Plume Fringe

Mineralization (PFM) has been examined in the context of the sodium-hydroxyl-aluminum carbonate, dawsonite. Porosity and permeability changes within an arkosic sandstone reservoir were predicted based on parameters obtained in an actual CO_2 pilot injection test. Major results associated with this research include:

(1) Surface mineralization is possible with produced waters as cation sources. For the case of the Permian Basin, approximately 3 million metric tonnes of carbon (equivalent to ~57 % of the emissions from the six electric coal-fired power plants that operate within the Permian Basin, or the emissions from ~1 very large electric power plant) can be stored as carbonates assuming 100% efficiency in use of the divalent cations of produced waters. The ability for produced waters to store additional carbon in a dissolved form, as dissolved CO_2, is much less (~0.6 million metric tonnes) due to increased ionic strengths in the brines. Nevertheless, it would be pointless not to maximize the storage capacity by simply resaturating the brines (that have already been used as cation sources) with CO_2 before injection.

(2) Kinetic reaction path models and reactive transport models indicated marked changes in porosity (4% decrease) resulting from CO_2-brine-mineral interactions, particularly dawsonite mineralization. Exact timing of dawsonite formation is still unknown, however, due to the ambiguities in kinetic rate constants of important minerals, such as the aluminum silicates (albite and K-feldspar) as well as dawsonite.

(3) Kinetic reaction rates of aluminum silicate minerals (feldspar minerals) are cited in the literature to vary over approximate 4 orders of magnitude (1×10^{-17} moles/cm^2-sec. to 1.62×10^{-13} moles/cm^2-sec.) (See Table 3-5-5 (a) and (b)). Furthermore, these kinetic reaction rates are based on a limited number of laboratory experiments which do not replicate actual in-situ reactive flow processes associated with CO_2 sequestration.

The results of this research provide useful information for policymakers as technologies and governments move closer to large-scale deployment of sequestration. Results from reaction path and reactive transport modeling can be used to predict reservoir reactivity when direct supercritical CO_2 injection is used as a sequestration technique. The ability to predict reactive processes induced by CO_2 injection will greatly aid in the selection and design of geologic CO_2 sequestration pilot tests.

Subsequent sequestration pilot testing will then aid in larger-scale sequestration use.

The prediction of porosity and permeability from these results can also be used in applications such as the oil and gas industry, specifically in profile control. Modeling of porosity and permeability will also allow for the evaluation of possible unintended impacts from geologic CO_2 sequestration such as contamination of potable aquifers as a result of pH depression, and possible escape of CO_2 from storage reservoirs.

The prediction of certain mineralization zones, such as dawsonite, in sequestration pilot reservoirs may provide information on diagenetic conditions for certain pore-filling minerals. Research on natural analogues for direct supercritical CO_2 injection, such as natural CO_2 reservoirs (Springerville and Bravo Dome), will benefit from the results on specific reaction paths that were defined in this research.

The capacity comparison that was defined in this research may be beneficial to companies or cooperatives that are considering mitigating carbon. The total amount of carbon that can be stored in a specific region and long-term effects of direct CO_2 injection on reservoir mineralogy must be predicted in order to determine the sequestration feasibility of certain geologic provinces.

4.5 RECOMMENDATIONS FOR FUTURE RESEARCH

KINETIC GEOCHEMICAL EXPERIMENTATION

It is clear that one of the major limitations within this study was the ambiguities in kinetic rate constants for the minerals of concern. Kinetic reaction rate studies (both batch and flow-through laboratory experiments) should be implemented to constrain mineralization and dissolution timing of aluminum silicate minerals and dawsonite. Kinetic reaction rates obtained in the laboratory could then be used to calibrate reactive

transport simulations. Upscaling from the results of laboratory experiments and simulations to the reservoir scale should also be examined. Parameterization of specific surface areas should also be accomplished for potential target reservoirs by means of techniques for surface area quantification, such as the Brunauer-Emmett-Teller (BET) method.

INJECTION TESTS AND IMAGING TECHNIQUES

Ongoing studies of long-term CO_2 core-flooding should include neutron tomographic imaging techniques that allow both 2- and 3-D visualization of porosity without core destruction. This nondestructive imaging technique will allow the precise comparison of certain core regions as a function of CO_2 injected. This will provide useful insight into the mineralization and dissolution processes within potential target reservoirs for direct injection of supercritical CO_2.

GEOCHEMICAL MODELING

Future reaction path and reactive transport models should incorporate the Pitzer equations to calculate ion activity so that error induced by brines of high ionic strength can be minimized. The Pitzer databases, used in this study and others, are valid for very simple systems with only major cations and anions present in solution. Specific minerals (e.g. dawsonite) have yet to be incorporated within these data sets. Completion of these recommendations will greatly improve the accuracy of model results and ultimate interpretations for this and future geologic sequestration sites.

References

Abel et al., (2004). "Reactive Transport Processes Occurring in a CO_2 Pilot Injection Test." Proceedings of the 3rd Annual Conference on Carbon Sequestration, (May 3-6, Alexandria, Virginia) (In Press).

Adenekan, A., T. W. Patzek, et al. (1993). "Modeling of multiphase transport of multicomponent organic contaminants and heat in the subsurface." Water Resources Research **29**(11): 3727-3740.

Aikawa N., M. Yoshida and K. Ichikawa (1972). " Discovery of dawsonite and alumohydrocalcite from the Cretaceous Izumi Group in Osaka Prefecture, southwest Japan. *Journal of the Japanese Association of Mineralogists, Petrologists and Economic Geologists*, **67**, 370-385.

Appelo, C. J. and D. Postma. (1993). Geochemistry, Groundwater and Pollution. Rotterdam, The Netherlands, A.A. Balkema.

Aziz, K. and A. Settari. (1979). "Petroleum Reservoir Simulation." *Applied Science*.

Bachu, S. and J. J. Adams. (2003). Sequestration of CO_2 in geological media in response to climate change: capacity of deep saline aquifers to sequester CO_2 in solution. *Energy Convers. Mgmt,* Elsevier Ltd.: 3151-3175.

Baker, J. C. (1991). "Diagenesis and reservoir quality of the Aldebaran Sandstone, Denison Trough, east-central Queensland, Australia." *Sedimentology* **38**: 819-838.

Baker, J. C., et al. (1995). "Continental-scale magmatic carbon dioxide seepage recorded by Dawsonite in the Bowen-Gunnedah-Sydney Basin System, Eastern Australia." *Journal of Sedimentary Research* **A65**: 522-530.

Benner, S. G., et al. (2001). "Geochemistry of Magnesium Silicate Carbonation in an aqueous medium (carbon mineralization)." Proceedings of the 1st Annual Conference on Carbon Sequestration, (May 7-10, 2003, Alexandria, Virginia).

Bethke, C. M. (2002). The Geochemist's Workbench: A User's Guide to Rxn, Act2, Tact, React, and Gtplot. Illinois: Hydrogeology Program, University of Illinois.

Bond, G.M., et al. (1999). "Enzymatic catalysis and CO_2 sequestration." *World Resource Review*, **11**(4): 603-619.

Bond, G. M., et al. (2001). "Development of integrated system for biomimetic CO_2 sequestration using the enzyme carbonic anhydrase." *Energy and Fuels*, **15**: 309-316.

Bond, G. M., et al. (2002). Capturing and sequestering CO_2 nature's way: biomimetic approaches. *Future Energy Systems and Technology for CO2 Abatement Proceedings*, (November 18-19, 2002, Antwerp, Belgium), 269-276.

Bond, G. M., et al. (2003). "Biomimetic and Geologic Mineralization Approaches to Carbon Sequestration." Proceeding of the 2nd Annual Conference on Carbon Sequestration, (May 5-8, 2003, Alexandria, Virginia).

Bond, G. M., et al (2004). "Biomimetic sequestration of CO2 in carbonate form: role of produced waters and other brines." *Fuel Processing Technology*, (In Press).

Brister, B.S., D. Ulmer-Scholle. (2003). "Interpretation of depositional environments of Upper Seven Rivers Formation from core and well logs, Grayburg Jackson Pool, Eddy County, New Mexico." in The Permian Basin: proving ground for tomorrow's technologies, W.D. Demis, M.K. Nelis, and R,C, Trentham, eds., West Texas Geological Society Publ., No. 00-109.

Brohan, P., et al. (2006). "Uncertainty estimates in regional and global observed temperature changes: a new dataset from 1850". *J. Geophysical Research* **111**: D12106.

Bureau of Economic Geology (2002). "Technical summary: Optimal geologic environments for carbon dioxide disposal in brine formations (saline aquifers) in the United States."

Chang, Y., B. K. Coats and J. S. Nolen. (1998). "A composition model for CO_2 floods including CO_2 solubility in water." *SPE Reservoir Evaluation and Engineering*: 155-160.

Coats, K.H., et al. (1974). "Three dimensional simulation of streamflooding." *Society Of Petroleum Engineers*: 573-594.

Cole, B. S. (1999). An equation of state for multiphase CO_2 and water. Independent Study (M.Sc), New Mexico Institute of Mining and Technology.

Duff, I. S. (1977). "MA28-A set of FORTRAN subroutines for sparse unsymmetrical linear equations." AERE Harwell Report R 8730.

Edwards, A. L. (1972). "TRUMP: A computer program for transient and steady state temperature distributions in multidimensional systems." Springfield, VA. National Technical Information Service, National Bureau of Standards.

Enick, R. M., and S. M. Klara. (1990). CO_2 solubility in water and brine under reservoir conditions. Chemical Engineering Communications, **90**, (1): 23-33.

Fleming, G. W. and L. N. Plummer. (1983). "PITZINPT--an interactive computer program for constructing input data sets to the geochemical simulation program PHRQPITZ." *U.S. Geological Survey Water-Resources Investigations Report* (83-4236): 108.

Garber, R.A., G.A. Grover and P.M. Harris. (1989). " Geology of the Capitan shelf margin-subsurface data from the Northern Delaware Basin." in Harris, P. M., and Grover, G.A., eds., Sub-surface and out-crop examination of the Capitan Shelf Margin, Northern Delaware Basin: SEPM Core Workshop No. 13, 3-272.

Gaus, Irina, et al. (2003). "Reactive transport modeling of dissolved CO_2 in the Cap Rock Base during CO_2 sequestration (Sleipner Site, North Sea)." 2nd Annual Conference on Carbon Sequestration: 1-13.

Gillespie, P. C. and G. M. Wilson. (1982). "Vapor-liquid and liquid-liquid equilibria: water-methane, water-carbon dioxide, water-hydrogen sulfide, water-npentane, water-methane-npentane." Research Report RR-48, Gas Processors Assn. Tulsa, Oklahoma **11**.

Goldbery, R. and F. C. Loughnan. (1977). "Dawsonite, alumohydrocalcite, nordstrandite and gorceixite in Permian marine strata of the Sydney Basin, Australia." *Sedimentology* **24**: 565-579.

Guthrie, G., J. W. Carey, et al. (2000). Geochemical aspects of the carbonation of magnesium silictes in an aqueous medium. First Annual Carbon Sequestration Proceedings, LANL.

Harrington, B.J. (1874). "Notes on dawsonite, a new carbonate." *Canadian Naturalist,* **7**: 305-309.

Ingerbritsen, S. E., W. E. Sanford. (1998). Groundwater in Geologic Processes. Cambridge, United Kingdom, Cambridge University Press.

IPCC (2007). Climate Change 2007: "The physical science basis." Summary for Policy Makers.

Johnson, James W., et al. (2001). "Reactive transport modeling of geologic CO2 sequestration in saline aquifers: the influence of intra-aquifer shales and the relative effectiveness of structural, solubility, and mineral trapping during prograde and retrograde sequestration." UCRL-JC-146932, Lawrence Livermore National Laboratory.

Jones, P.D., and A. Moberg (2003). "Hemispheric and large-scale surface air temperature variations: an extensive revision and an update to 2001." Journal of Climate: Vol. 16, No. 2, 206–223.

Kaszuba, J. P., et al. (2002). "Carbon dioxide reaction processes in a model brine aquifer at 200°C and 200 bars: implications for geologic sequestration of carbon." *Applied Geochemistry* **18**: 1065-1080.

Keene, F. R. (1993). Thermodynamic, Kinetic and Product Considerations in Carbon Dioxide Reactivity. Amsterdam, Netherlands, Elsevier.

Keeling, C.D. and T.P. Whorf. (2003). Atmospheric CO2 records from sites in the SIO air sampling network. In Trends: A Compendium of Data on Global Change. Carbon Dioxide Information Analysis Center, Oak Ridge National Laboratory, U.S. Department of Energy, Oak Ridge, Tenn., U.S.A.

Krumhansl, J.L., et al (2002). "Geological sequestration of carbon dioxide in a depleted oil reservoir." In Proceedings of the SPE/DOE 13th Symposium on Improved Oil Recovery, Tulsa, OK, April 13-17.

Law, D. H.-S. and S. Bachu. (1996). "Hydrogeological and numerical analysis of CO_2 disposal in deep aquifers in the Alberta Sedimentary Basin." *Energy Convers. Mgmt* **37**: 1167-1174.

Lichtner, P. C. (1985). "Continuum model for simultaneous chemical reactions and mass transport in hydrothermal systems." *Geochimica et Cosmochimica Acta* **49**(3): 779-800.

Lichtner, P. C. (1992). "Time-space continuum description of fluid/rock interaction in permeable media." *Water Resources Research* **28**: 3135-3155.

Lichtner, P. C., C. I. Steffel, et al. (1996). "Reactive transport in porous media." *Reviews in Mineralogy*.

Lichtner, P.C. (2000). FLOTRAN Users Guide. Los Alamos, New Mexico, Los Alamos National Laboratory. DRAFT.

Liu, N., et al. (2005). Biomimetic sequestration of CO_2 in carbonate form: role of produced waters and other brines. *Fuel Processing Technology* **86,** 1615-1625.

Malinin, S. D., and N. A. Kurovskaya. (1975). "Solubility of CO_2 in chloride solutions at elevated temperatures and CO_2 pressures." *Geochemistry International* **2**, No. 2: 199.

Malinin, S. D., and N. I. Savelyeva. (1972). "The solubility of CO_2 in NaCl and $CaCl_2$ solutions at 25, 50, and 75° under elevated CO_2 pressures." *Geochemistry International* **9**, No. 1: 410.

McRee, B. C. (1977). "How it works, where it works." *Petroleum Engineer International,* **49**, No. 12, 52.

Medina, M. G., et al. (2000). Comparison of carbonic anhydrase isozymes for use as catalyst in carbon dioxide sequestration process. Proceedings of the Air & Waste Management Association's 93rd Annual Conference & Exhibition (Salt Lake City, Utah, June 18-22, 2000).

Moridis, G. and K. Pruess. (1995). "Flow and transport simulations using T2CG1, a package of conjugate gradient solvers for the TOUGH2 family of codes." Lawrence Berkeley Laboratory Report LBL-36235, Berkeley , CA.

Moridis, G. and K. Pruess. (1998). "T2SOLV: An enhanced package of solvers for the TOUGH2 family of reservoir simulation codes." *Geothermics*, **27,** No. 4, 415-444.

Narasimham, T. N. and P. A. Witherspoon. (1976). "An integrated finite difference method of analyzing fluid flow porous media." *Water Resource Res.* **12**(1): 57-64.

Palache, C., H. Berman, and C. Frondel. (1960). The system of mineralogy of Dana. 7th edition, John Wiley and Sons, New York.

Palandri, J.L. (2004). "Experimental studies of CO2 sequestration: CO2-SO2 injection in ferric iron-bearing sediments." Proceedings of the 3rd Annual Conference on Carbon Sequestration, (May 3-6, Alexandria, Virginia) (In Press).

Pawar, R.J., et al. (2003). "Numerical modeling of CO2 sequestration in a depleted oil reservoir." Proceedings of the 3rd Annual Conference on Carbon Sequestration, (May 3-6, Alexandria, Virginia) (In Press).

Pawar, Rajesh. Personal Interview. (December 2003).

Pitzer, K. S. (1979). Theory: Ion interaction approach Activity Coefficients in Electrolyte Solutions. Boca Raton, Florida, CRC Press.

Pocker, Y., L. Bjorkquist, and D. W. Bjorkquist. (1977). Zinc (II) and cobalt (II) bovine carbonic anhydrases. comparative studies and esterase activity. *Biochemistry* (**16**)18.

Pruess, K., and G. Moridis. (1999). TOUGH2 User's Guide, Version 2.0. Berkley, California, LBL: 197 p.

Pruess, Karsten, et al. (2003). "Numerical modeling of aquifer disposal of CO_2." *SPE Journal*: March, 49-60.

Ren, X. and S. Lindskog. (1992). Buffer dependence of CO_2 hydration catalyzed by human carbonic anhydrase I, *Biochim. Biophys. Acta* **1120**, 81–86.

Smith, J. W., and C. Milton. (1966). "Dawsonite in the Green River Formation of Colorado." *Economic Geology* **61**: 1029-1042.

Span, R. and W. Wagner. (1996). "A new equation of state for carbon dioxide covering the fluid region from the triple point temperature to 1100 K at pressures up to 800 Mpa." *Journal of Physical Chemistry* **25**(6): 1509-1596.

Stauffer, et al. (2003). "Understanding geochemical interactions resulting from CO2 sequestration in a depleted oil reservoir West Pearl Queen Reservoir, Hobbs, NM." GSA Annual Meeting, November 2-5, Seattle, Washington.

Stillings, L. L. and S. L. Brantley. (1995). "Feldspar dissolution at 25C and pH 3: reaction stoichiometry and the effect of cations." *Geochim Cosmochim Acta* **59**:1483-1496.

Stryer, L., (1988). Biochemistry. 3rd edition, W.H. Freeman and Company, New York.

U.S. Energy Information Administration. (2006). Major CO_2 Pipeline Map, Washington, D.C.

U.S. Energy Information Administration. (2006). United States projected CO2 emissions from coal-fired electric power plants, Office of Integrated Analysis and Forecasting, Washington, D.C.

U.S. Energy Information Administration, International Energy Outlook. (2003). Energy Information Administration, Office of Integrated Analysis and Forecasting, Washington, D.C.

Van der Meer, L. G. H. (1993). "The conditions limiting CO_2 storage in aquifers." *Energy Convers. Mgmt.* **34**(9-11): 959-966.

VanderKwaak, J. E., P. A. Forsyth, et al. (1995). "WATSOLV, Sparse Matrix Iterative Solver Package, Users Guide. Waterloo, Ontario, Canada: Waterloo Centre for Groundwater Research, University of Waterloo."

Volkova, A.N., and L. G. Rekshinskaya. (1973). "Dawsonite in the Balakhonska Series of the Kuznetsk Basin." *Lithology of Mineral Resources* 8: 88-93.

Ward, R. F., St. G. Kendall, and P. M. Harris. (1986). "Upper Permian (Guadalupian) facies and their association with hydrocarbons: Permian Basin, west Texas and New Mexico." *American Association of Petroleum Geologists Bulletin* **70**: 239–262.

Wawersik, R., F. M. Orr, et al. (2001). "Terrestrial sequestration of CO_2: an assessment of research needs." *Advances in Geophysics* **43**.

Weir, G., S. White and W. Kissling. (1996). Reservoir Storage and Containment of Greenhouse Gases, II: Vapour-Entry Pressures. Netherlands, Kluwer Academic Publishers: 61-82.

Wellman, T. P. (2002). "Concatenation of a reactive transport model to simulate CO_2 sequestration in geologic media." New Mexico Institute of Mining and Technology, Socorro, New Mexico.

Westrich, H., et al. (2002). "Sequestration of CO_2 in a depleted oil reservoir: an overview." Albuquerque, New Mexico, Geoscience and Environment Center, Sandia National Laboratories.

Wiebe, R. (1941). "The binary system carbon dioxide-water under pressure." *Chemical Reviews* **29**: 475.

Wolery (1983). EQ3NR, "A computer program for geochemical aqueous speciation solubility calculations: user's guide and documentation" UCRL-53414, Lawrence Livermore National Laboratory.

Xu, T., and K. Pruess. (2001). " Modeling multiphase non-isothermal fluid flow and reactive geochemical transport in variably saturated fractured rocks: 1. methodology." *American Journal of Science* **301**: 16-33.

APPENDIX A:

TOUGH2: THEORETICAL FRAMEWORK AND WEST PEARL QUEEN NUMERICAL SIMULATIONS

TOUGH2 SIMULATOR

TOUGH2 can simulate multidimensional (1-, 2-, or 3-D), multiphase, nonisothermal, multicomponent fluid systems in porous and fractured media. TOUGH2 was first developed by Karsten Pruess and others in the early 1990's and was released to the public in 1991. Development of TOUGH2 was intended mainly for applications of geothermal reservoir engineering and nuclear waste disposal. It has since been utilized for many other applications including sequestration of CO_2 in subsurface reservoirs.

Primary thermodynamic variables within TOUGH2 are evaluated under the assumption that local thermodynamic equilibrium exists. The current consensus is that this is generally a good working assumption for most practical cases (Coats et al., 1974). The Gibb's phase rule is used to establish the number of degrees of freedom, f, in a system consisting of NK components which are distributed among NPH phases, or

$$f = NK + 2 - NPH . \qquad \text{Eq. 1}$$

The number of degrees of freedom with respect to saturation are ($NPH - 1$) due to the fact that NPH phase saturations S_β are defined by the relationship

$$\sum_{\beta=1}^{NPH} S_\beta = 1 . \qquad \text{Eq. 2}$$

Thus the total number of primary thermodynamic variables is

$$NK1 = f + NPH - 1 \\ = NK + 1 \qquad \text{Eq. 3}$$

where $NK1$ is equal to the total number of equations per grid block, NK is the number of mass balance equations for each mass quantity within the system, and the "1" denotes the one energy balance equation (Pruess and Moridis, 1999). In this study, four primary variables (P, XCO_2, SCO_2, T) are required to simulate the flow and transport of H_2O and CO_2 in a nonisothermal system, where P is pressure, XCO_2 is the dissolved phase CO_2 mass fraction, SCO_2 is the separate phase CO_2 saturation, and T is temperature. The CO_2 equation of state (EOS) implemented in this study utilizes a persistent variable technique and is further explained below in section CO_2 EQUATION OF STATE (page 100).

TOUGH2 employs an integral finite volume approach to approximate mass and energy conservation equations, while discretizing time using a fully implicit method (Edwards, 1972; Narasimhan and Witherspoon, 1976). A main advantage of using this integral finite volume approach is that it avoids any reference to a global system of coordinates, making regular and irregular grids possible in one, two, and three dimensions. Assuming Darcy's law for a nonisothermal multiphase flow of multicomponent fluids applies, one can express conservation of mass for each component and conservation of thermal energy about a certain flow domain with volume V_n and bounding surface Ω_n as follows:

$$\frac{d}{dt}\int_{V_n} M^\gamma dV = \int_{\Omega_n} \overline{F}^\gamma \bullet \vec{n}\, d\Omega + \int_{V_n} q^\gamma dV \ , \qquad \text{Eq. 4}$$

where γ indicates the particular mass component, M^γ is the mass or energy per unit volume, $\overline{F}^\gamma$ is the mass or heat flux per unit area, $\vec{n}$ is a unit vector normal on the surface

element $d\Omega_n$ pointing inward into V_n, and q^γ is the source or sink with respect to component γ per unit volume (Pruess and Moridis, 1999). The first term in Equation 4 represents the net accumulation or storage term of the flow domain V_n. The second term represents the net flux of mass or energy into the bounded surface Ω_n and the final term represents the source or sink of mass or energy within the flow domain V_n. The mass accumulation term in general form can be written as follows:

$$M^\gamma = \phi \sum_\beta S_\beta \rho_\beta X_\beta^\gamma , \qquad \text{Eq. 5}$$

where ϕ represents porosity, S_β is the saturation of a certain phase β (i.e. liquid, gas, etc.), ρ_β is the density of phase β, and X_β^γ is the mass fraction of component γ in phase β (Pruess and Moridis, 1999). Energy accumulation within the energy conservation equation can be stated as follows (Eq. 6) with energy transport from both the solid material (grains) and fluid (CO_2 and H_2O):

$$M^\gamma = (1-\phi)\rho_r c_r T + \phi \sum_\beta S_\beta \rho_\beta u_\beta . \qquad \text{Eq. 6}$$

In this representation ρ_γ and c_r are grain density and specific heat of the rock, respectively, T is temperature, and u_β is specific internal energy in phase β. The first term on the right hand side of this equation denotes the energy within the solid matrix while the second term represents the energy of the fluid within the pore spaces. Mass fluxes over all phases are assumed to be advection dominated. Diffusional mass fluxes are neglected. Advective mass flux is represented by

$$\overline{F}^\gamma = \sum_\beta X_\beta^\gamma \overline{F}_\beta , \qquad \text{Eq. 7}$$

where $\overline{F}^{\gamma}$ is the mass or heat flux per unit area, X_{β}^{γ} is the mass fraction of component γ in phase β, and $\overline{F}_{\beta}$ is defined as the fluid flux of phase β (Pruess and Moridis, 1999). Fluid fluxes are given by Darcy's law with respect to each phase and is represented by

$$\overline{F}_{\beta} = \bar{u}_{\beta}\rho_{\beta} = -k\frac{k_r}{\mu_{\beta}}\rho_{\beta}(\nabla P_{\beta} - \rho_{\beta}\bar{g}). \qquad \text{Eq. 8}$$

In this equation, $\bar{u}_{\beta}$ is the Darcy velocity in phase β, k is intrinsic permeability, $k_{r\beta}$ is relative permeability to phase β, P_{β} is the sum of the fluid pressure and capillary pressure in phase β, and $\bar{g}$ is gravitational acceleration (Pruess and Moridis, 1999). Permeability must be modified in the presence of a gas phase due to the Klinkenberg effect. As gas pressure decreases, the absolute permeability of the gas phase decreases according to the relationship

$$k = k_{\infty}(1 + \frac{b}{P}), \qquad \text{Eq. 9}$$

where k_{∞} is the permeability at infinite pressure, b is the Klinkenberg parameter, and P is the pressure. Flux of energy is calculated by including both conductive and advective terms,

$$\overline{F}^{\gamma} = -K\nabla T + \sum_{\beta} H_{\beta}\overline{F}_{\beta}, \qquad \text{Eq. 10}$$

where K is effective thermal conductivity of the porous medium accounting for both solids and fluids, and H_{β} is the specific enthalpy in phase β (Pruess and Moridis, 1999).

The first term is equivalent to the conductance of heat and the second term defines the advective heat flow term.

Discretizing the previously explained continuum equations is done using the integral finite difference method (IFD; Edwards, 1972; Narasimhan and Witherspoon, 1976). The numerical approximation of all parameters is considered to be volume average quantities. In the overall governing equation for TOUGH2 (Eq. 4), the term on the left-hand side of this equation without the time derivative, $\int_{V_n} M^\gamma dV$, and the second term on the right hand side of the equation, $\int_{V_n} q^\gamma dV$, are both volume integrals that can be approximated by writing mass and energy accumulation terms as

$$\int_{V_n} M^\gamma dV = V_n M_n^\gamma , \qquad \text{Eq. 11}$$

where M is the volume-normalized extensive property (H_2O, CO_2, or enthalpy) and M_n is the average value of M over the volume V_n. Source or sink terms within the current model can similarly be represented as

$$\int_{V_n} q^\gamma dV = V_n q_n^\gamma , \qquad \text{Eq. 12}$$

where q^γ is the mass or energy source or sink or γ per unit volume and q_n^γ is the average values of q^γ over the volume element V_n (Pruess and Moridis, 1999). The net flux term within equation 3-1-4, $\int_{\Omega_n} \overline{F^\gamma} \bullet \bar{n} d\Omega$, and all other surface integrals can be approximated as a discrete sum of averages over surface segments between neighboring volume elements. Figure 1 is a schematic representation of the surface integral concept.

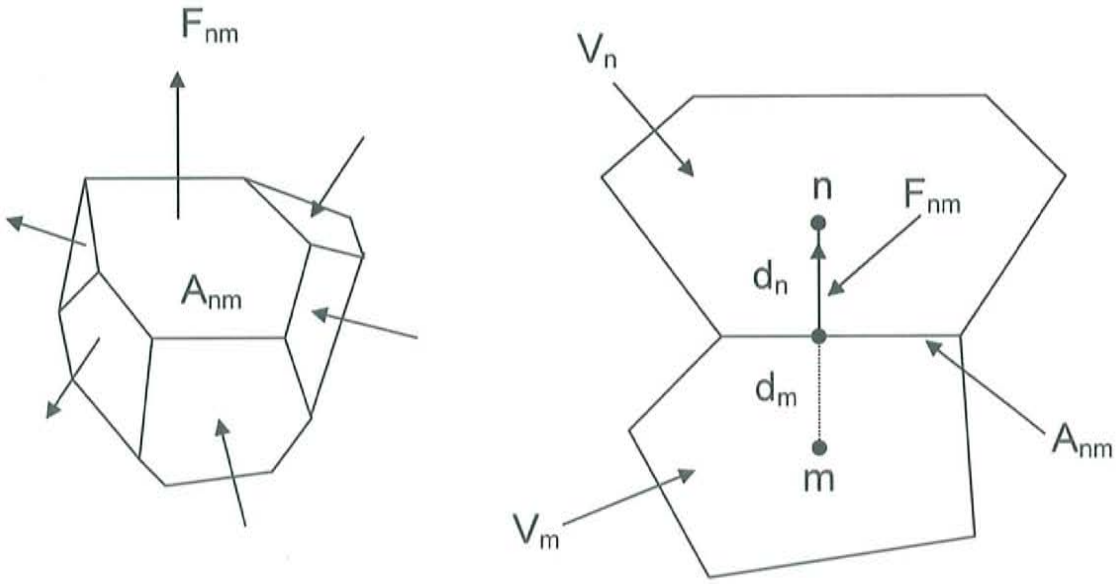

Figure 1: Spatial discretization approaches within the integral finite difference method (after Pruess and Moridis, 1999).

Within Figure 1, V_n and V_m represent volume elements n and m, A_{nm} denotes the surface segment between volume elements n and m, d_n and d_m represent the nodal distance from the centroid of the respective element to the interface between the two elements, and F_{nm} represents the average value of the normal component of $\overline{F}$ over the surface segment A_{nm} between elements n and m. The net flux expression can now be written as

$$\int_{\Omega_n} \overline{F^\gamma} \bullet \bar{n} d\Omega = \sum_m A_{nm} F_{nm}, \qquad \text{Eq. 13}$$

where the summation denotes the total area after summing all of the surface segments (Pruess and Moridis, 1999). The multiphase Darcy flux equation (Eq. 8) can be written in a discretized form following the previous rationale of discretizing space. This discretized phase flux is denoted in terms of averages over parameters for elements V_n and V_m and can be written as

$$F_{\beta,nm} = -k_{nm}\left[\frac{k_{r\beta}\rho_{\beta}}{\mu_{\beta}}\right]_{nm}\left[\frac{P_{\beta,n} - P_{\beta,m}}{d_{nm}} - \rho_{\beta,nm}g_{nm}\right], \qquad \text{Eq. 14}$$

where nm represents those quantities that are evaluated at the interface between volume elements V_n and V_m, d_{nm} is the distance between nodal points n and m and can be defined by $d_{nm} = d_n + d_m$, g_{nm} is the component of gravitational acceleration in the direction of m to n (Pruess and Moridis, 1999). Calculations of quantities at the interface between volume elements require some type of averaging scheme. In this study and studies by Cole (1999) and Wellman (2002), upstream weighting is used for most interface terms. Absolute permeability interface values are calculated using harmonic weighting while the mass density in the gravitational term is calculated using arithmetic averaging. Previous work by Aziz and Settari (1979) has shown that without upstream weighting in multiphase systems convergence to nonphysical solutions may occur. Thus, applying an upstream weighting scheme to multiphase transport of CO_2 is a correct approach.

Substituting these spatially discretized equations for mass and energy accumulation (Eq. 11), source or sink terms (Eq. 12), and net flux (Eq. 13) into the governing equation (Eq. 4) results in a set of first-order ordinary differential equations in time.

$$\frac{dM_n^{\gamma}}{dt} = \frac{1}{V_n}\sum_m A_{nm}F_{nm}^{\gamma} + q_n^{\gamma} \qquad \text{Eq. 15}$$

Discretization of time is a first-order finite difference while the flux and sink source terms on the right hand side of the equation are evaluated at a new time , $t^{k+1} = t^k + \Delta t$ (fully implicit). Discretizing Eq. 15 in time utilizing this fully implicit method results in the following set of coupled non-linear, algebraic equations

$$R_n^{\gamma,k+1} = M_n^{\gamma,k+1} - M_n^{\gamma,k} - \frac{\Delta t}{V_n}\left\{\sum_m A_{nm} F_{nm}^{\gamma,k+1} + V_n q_n^{\gamma,k+1}\right\} = 0 \qquad \text{Eq. 16}$$

where $R_n^{\gamma,k+1}$ are the residuals. Residuals equal to zero are not possible on a finite arithmetic machine, thus a tolerance must be set based on the accuracy of the machine. Each grid block in a model domain has $NEQ = NK + 1$ equations. The total flow system thus contains NEL grid blocks and a total of $NEL \times NEQ$ coupled non-linear equations (Pruess and Moridis, 1999). Unknown variables are the $NEL \times NEQ$ independent primary variables which define the state of the flow system at time t^{k+1}. This system of coupled non-linear equations is solved by Newton/Raphson iteration. At each new time step, primary variable values of the last time step are chosen as the initial guess for the current time step. These primary variables are used in conjunction with the CO_2 equation of state to calculate secondary variables inherent within the mass and energy balance equations. The change in solution residuals are monitored as individual primary variables are incremented. The iteration scheme introduces the index p for the current iteration index and p+1 for the incremented iteration index along with the unknown independent primary variable index $\{x_i;\ i = 1,\ldots, NEL \times NEQ\}$. We can expand the residuals, $R_n^{\gamma,k+1}$, in a first order Taylor series in terms of the aforementioned iteration index to produce

$$R_n^{\gamma,k+1}\left(x_{i,p+1}\right) = R_n^{\gamma,k+1}\left(x_{i,p}\right) + \sum_i \left.\frac{\partial R_n^{\gamma,k+1}}{\partial x_i}\right|_p \left(x_{i,p+1} - x_{i,p}\right). \qquad \text{Eq. 17}$$

Rearranging Eq. 17 to solve for the residuals and the assumed solution $R_n^{\gamma,k+1}\left(x_{i,p}\right)$, we obtain

$$-\sum_i \left.\frac{\partial R_n^{\gamma,k+1}}{\partial x_i}\right|_p \left(x_{i,p+1} - x_{i,p}\right) = R_n^{\gamma,k+1}\left(x_{i,p}\right), \qquad \text{Eq. 18}$$

where the first term on the left hand side of the equation is the Jacobian matrix, $\left(x_{i,p+1} - x_{i,p}\right)$ is the change in the independent primary variables between iteration level p and p+1, $R_n^{\gamma,k+1}$ is the residual at time k+1, and $\left(x_{i,p}\right)$ are the values of the independent primary variables at the previous iteration level p (Pruess and Moridis, 1999). Eq. 18 is evaluated using sparse direct matrix methods (Duff, 1977) or iteratively utilizing preconditioned conjugate gradients (Moridis and Pruess, 1995, 1998). Iteration is continued until a convergence criterion has been met, or

$$\left|\frac{R_n^{\gamma,k+1}}{M_n^{\gamma,k+1}}\right| \leq \varepsilon_1 . \qquad \text{Eq. 19}$$

Once this convergence criterion is met, the converged solution is the assumed solution for the first iteration in the next time step. Size of the initial time step is user specified and for every time step that converges in less than a user-specified number of iterations, the next time step is doubled. When convergence is not achieved at a certain time step within a specified number of iterations (in this case 8), the time step is reduced by a specified factor. Failure solving the linear equations also results in automatic time step reduction (Adenekan et al, 1993).

Boundary conditions and initial conditions are implemented within TOUGH2 by alteration of the grid information and initial conditions data within the input. Dirichlet conditions can be prescribed by the implementation of large volume elements V_n and prescribing desirable primary variables within these cells therefore causing essentially no

change within these variables throughout the simulation period. Neumann conditions (constant flux of mass or energy across boundaries) can also be prescribed over certain cells. The special commonly used Neumann condition of "no flux" can be prescribed by not specifying any flow connections across a boundary.

CO_2 EQUATION OF STATE

Cole (1999) developed a CO_2 equation of state (EOSCO2) at The New Mexico Institute of Mining and Technology that enables the simulation of mass and energy flow in dissolved CO_2 phase, separate phase CO_2 (supercritical CO_2 or gaseous phase CO_2), and a mixture of separate phase CO_2 and water. CO_2 phase determination is solely dependent on the thermodynamic variables of the system in question. Effects of chemical species other than dissolved CO_2 on the thermophysical variables have not yet been defined.

The study completed by Cole (1999) utilized a persistent primary variable method to characterize single phase and multiphase systems. The persistent variables used are: pressure (P), dissolved mass fraction of CO_2 (XCO_2), separate phase CO_2 saturation (SCO_2), and temperature (T). Using a persistent variable method for the calculation of pertinent secondary variables avoids the need to use the variable switching technique employed by many other CO_2 equations of state (Prues and Moridis, 1999 and Weir et al, 1996). Studies utilizing this variable switching technique have reported convergence issues for certain problems (Cole, 1999 and Weir et al, 1996).

Interphase mass transfer between separate phase CO_2 and water is characterized by implementing a source/sink method via changing the Jacobian matrix directly to increase or decrease the dissolved CO_2 in water depending on the thermodynamic conditions. Using the persistent primary variable method in this model allows for separate mass

balancing among the CO_2 components. After each iteration within the Newton/Raphson iteration loop, the potential solubility of CO_2 at the given pressure and temperature is calculated for each volume cell utilizing the extended Henry's law relationship. Potential solubility represents the dissolved CO_2 in solution at equilibrium. Comparing the dissolved CO_2 in solution to the actual dissolved CO_2 within a given volume cell one can determine if the capacity exists for additional dissolved CO_2 storage within solution. If this comparison leads to the actual dissolved CO_2 value exceeding the potential dissolved CO_2 value, a sink in dissolved CO_2 mass will correct the actual value to the potential dissolved CO_2 value and a source term will transfer this excess dissolved CO_2 to separate phase CO_2 mass within the volume element. If dissolved CO_2 values are less than that of the potential dissolved CO_2 value calculated via Henry's law and separate phase CO_2 is present within the volume cell, then additional dissolved CO_2 will be added to the solution. This allows for the appearance and disappearance of phases given certain pressure and temperature conditions (Cole, 1999).

Within the EOSCO2, thermophysical variables are calculated for pure water, separate phase CO_2, and dissolved phase CO_2 mixtures. The following secondary variables are necessary to quantify nonisothermal flow of a multiphase, multicomponent system and are calculated through constitutive relationships within the EOSCO2 module:

- Specific density
- Specific enthalpy
- Dynamic viscosity
- Relative permeability
- Capillary pressure

The EOSCO2 has been tested and deemed valid for pressures ranging from 0.1 MPa to greater than 100 MPa, and for temperatures ranging from approximately 15 °C to greater than 200 °C (Cole, 1999). These thermodynamic conditions encompass most conditions found in sedimentary basins targeted for CO_2 injection. The reader is referred to the study conducted by Cole (1999) for a more detailed discussion of the EOSCO2 used within the current study.

EOSCO2 UPDATES

The previous version of EOSCO2 assumed pure water as the solvent. CO_2 solubility in pure water is approximately 50 percent higher than the solubility of CO_2 within NaCl brine with a weight percent solid of 20 percent (Figures 2 through 4).

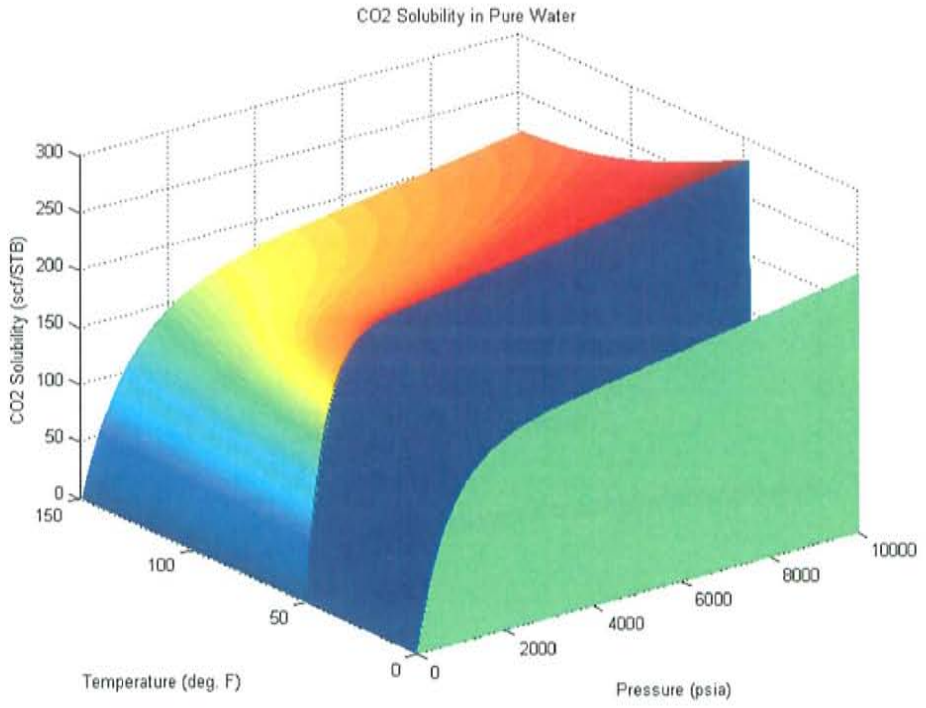

Figure 2: CO_2 Solubility in pure H_2O as a function of temperature and pressure

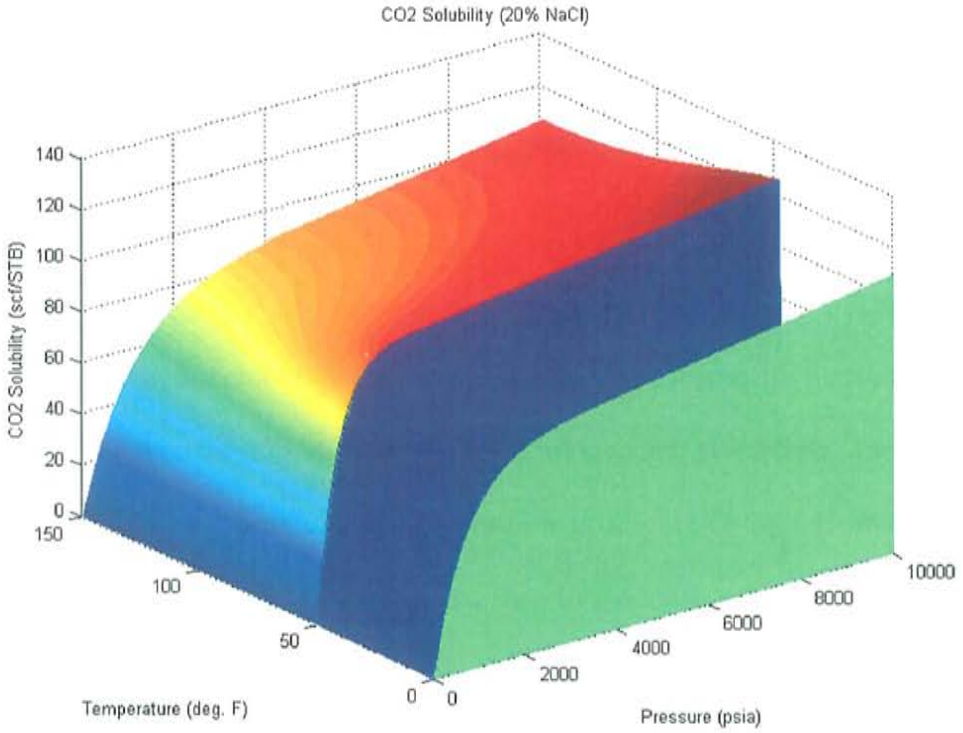

Figure 3: CO_2 solubility in 20 percent NaCl brine as a function of temperature and pressure

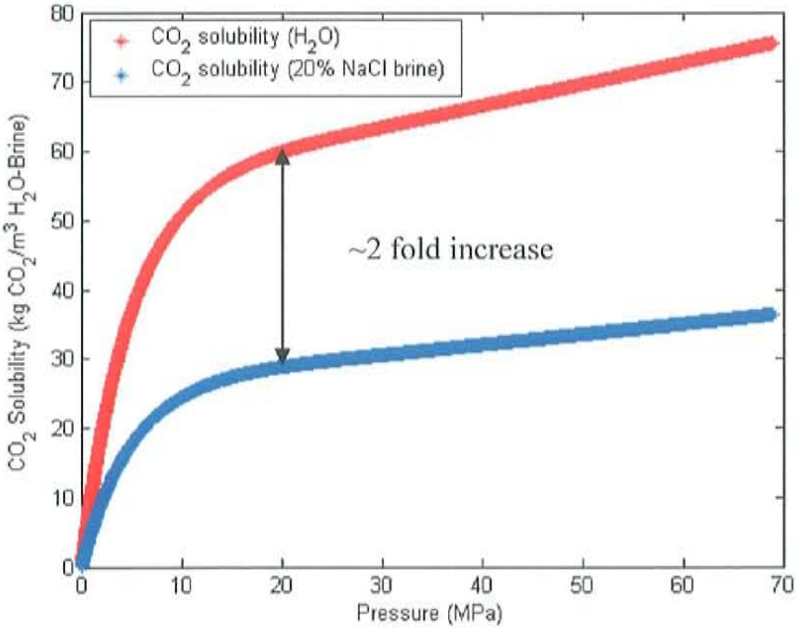

Figure 4: Comparison of CO_2 solubility in 20 percent NaCl brine and pure H_2O

Figures 2 and 3 show effects of temperature and pressure on CO_2 solubility in pure water (Figure 2) and in a 20 percent NaCl brine solution (Figure 3). CO_2 solubility is greatest at low temperatures ($\leq 75\ ^{\circ}F$) and high pressures (≤ 4000 psia) as represented in Figures 2 and 3.

This assumption that the solvent within EOSCO2 is pure water represents a gross overestimation of the amount of dissolved CO_2 in solution at any given time. In most sedimentary basins that have been targeted for possible geologic CO_2 sequestration, the formation waters have very high TDS values and therefore a lower propensity for CO_2 solubility trapping. As discussed previously, EOSCO2 implements a modified Henrys law to calculate the potential dissolved CO_2 within pure water. In the updated EOSCO2 used here, the potential dissolved CO_2 accounting for effects of brine TDS, is evaluated over all of the volume cells after each iteration step within the Newton/Raphson loop. The following details how the solubility effects of NaCl rich brine are addressed over various weight percents on the solubility of CO_2 within EOSCO2.

Chang et al. (1998) performed a study that included the development of a new empirical correlation for the solubility of CO_2 in distilled water as a function of pressure and temperature. The correlation can then be adjusted further for the effects of salinity to obtain the solubility of CO_2 in NaCl brine. This empirical correlation is easily implemented in EOSCO2.

CO_2 solubility in distilled water can be estimated using a piece-wise correlation written as

$$R_{sw} = a \cdot p \cdot \left[1 - b \cdot \sin\left(\frac{\pi}{2} \cdot \frac{c \cdot p}{c \cdot p + 1}\right)\right] \text{ if } p \le p^o$$

$$R_{sw} = R_{sw}^o + m \cdot (p - p^o) \text{ if } p \ge p^o \quad , \qquad \text{Eq. 20}$$

where

$$a = \sum_{i=0}^{4} a_i \cdot 10^{-3i} \cdot T^i , \qquad \text{Eq. 21}$$

$$b = \sum_{i=0}^{4} b_i \cdot 10^{-3i} \cdot T^i \quad 0 \le \mathrm{b} \le 1 , \qquad \text{Eq. 22}$$

$$c = 10^{-3} \cdot \sum_{i=0}^{4} c_i \cdot 10^{-3i} \cdot T^i , \qquad \text{Eq. 23}$$

$$p^o = \frac{2}{\pi} \cdot \frac{\sin^{-1}(b^2)}{c \cdot \left[1 - \frac{2}{\pi} \cdot \sin^{-1}(b^2)\right]} , \qquad \text{Eq. 24}$$

$$R_{sw}^o = a \cdot p^o \cdot (1 - b^3) , \qquad \text{Eq. 25}$$

$$m = a\left\{1 - b\left[\sin\left(\frac{\pi}{2} \cdot \frac{c \cdot p}{c \cdot p^o + 1}\right) + \frac{\pi}{2} \frac{c \cdot p^o}{\left(c \cdot p^o + 1\right)^2} \cos\left(\frac{\pi}{2} \cdot \frac{c \cdot p^o}{c \cdot p^o + 1}\right)\right]\right\} , \qquad \text{Eq. 26}$$

where R_{sw} is CO_2 solubility in scf (standard cubic feet) of CO_2 per STB (stock tank barrel) of water, T is temperature (°F), p is pressure (psia), and the coefficients $\{a_i, b_i, c_i, i = 0...4\}$ are given in Table 1.

	i = 0	i = 1	i = 2	i = 3	i = 4
a_i	1.163	-16.63	111.073	-376.859	524.889
b_i	0.965	-0.272	0.0923	-0.1008	0.0998
c_i	1.280	-10.757	52.696	-222.395	462.672

Table 1: Values of Coefficients in Eqns. 21 to 23

The data used to create this piece-wise correlation originated from solubility data for liquid and supercritical CO_2 in water (Wiebe, 1941). The correlation matches to within +/- 10 scf/STB (+/- 3.3 kg CO_2/m^3 water) for temperatures between 12 °C and 100 °C and pressures up to approximately 69 MPa. Another data set by Gillispie and Wilson (1982) was used to verify the pure water CO_2 solubility. Inconsistencies were present between the Gillispie and Wilson study and Wiebe (1941) particularly at lower temperatures thus; data from Wiebe (1941) were used in correlating the CO_2 solubility at lower temperatures ($\leq$ 29 °C). The correlation of CO_2 solubility in pure water can further be modified to include the effects of NaCl brine with varying weight percents

$$\log\left(\frac{R_{sb}}{R_{sw}}\right) = -0.028 \cdot C \cdot T^{-0.12}, \qquad \text{Eq. 27}$$

where R_{sb} is CO_2 solubility in scf of CO_2 per STB of brine, C is the salinity of brine in weight percent of solid, and T is temperature in (°F). CO_2 solubility decreases due to salinity as a function of temperature (Figure 4).

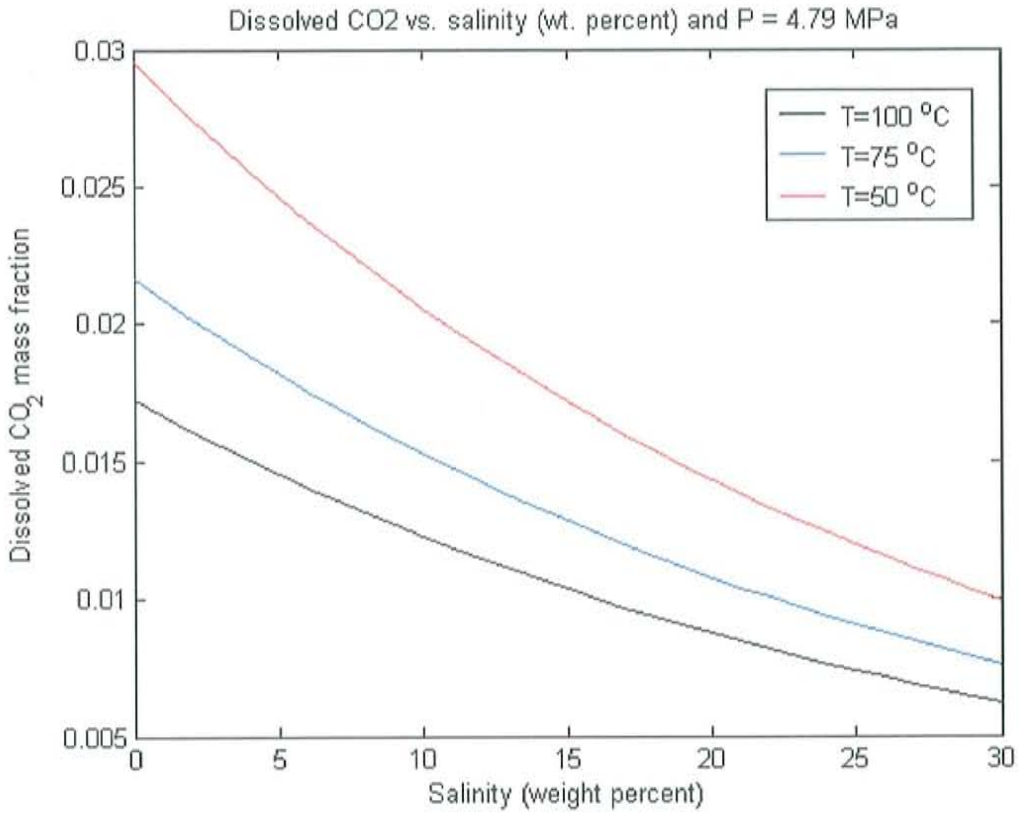

Figure 5: Dissolved CO_2 mass fraction as a function of temperature for several temperatures

Note the gradual convergence of dissolved CO_2 mass fraction as salinity increases. Within very saline aquifers ($\geq\sim$ 25 %), temperature effects on CO_2 solubility become relatively unimportant and the effects of salinity dominate.

Data used within this correlation originated from Malinin and Savelyeva (1972), Malinin and Kurovskaya (1975), and McRee (1977). Equation 27 matches these CO_2 solubility data in NaCl solutions to within +/- 3.3 kg CO_2/m^3 brine (Chang et al., 1998).

In summary, using the empirical correlation of Chang et al. (1998), salinity effects of NaCl brines were incorporated within EOSCO2. The calculation of CO_2 solubility in pure water has already been developed within the interphase mass transfer subroutine utilizing a modified Henrys law relation. Additional modifications were made to include

Equation 27 and correct the potential dissolved CO_2 mass in solution to simulate the depressed CO_2 solubility within NaCl brines. Equation 27 was modified further to accommodate units used within TOUGH2,

$$R_{sb} = F \cdot R_{sw} \cdot \rho_{CO_2\ (STP)} \cdot 10^{-Z \cdot S \cdot (1.8C+32)^{-0.12}},$$
$$\text{where } F = 0.1781942609,$$
$$Z = 0.028, \qquad \text{Eq. 28}$$
$$\rho_{CO_2} = \left[\text{kg/m}^3\right] CO_2 \text{ density at } 60\ ^{\circ}F \text{ and } 14.73 \text{ psia},$$

where R_{sb} is CO_2 solubility in units of kilograms CO_2 per cubic meter of brine. EOSCO2 calculates CO_2 solubility in dissolved CO_2 mass fraction within solution, thus before Eq. 28 is evaluated within EOSCO2, CO_2 solubility in pure water (R_{sw}) must be converted to scf per STB brine first. CO_2 solubility with respect to brine (R_{sb}) is calculated and converted back to dissolved CO_2 mass fraction and utilized as previously discussed in the interphase mass transfer details.

TOUGH2-EOSCO$_2$ SIMULATIONS

Reservoir-scale simulations of CO_2 flow and transport were developed to evaluate the West Pearl Queen reservoir pilot injection test. The TOUGH2 simulator was used for this modeling effort. Numerical grids were generated to replicate the structure of the Shattuck Sandstone in the vicinity of the pilot injection test. This modeling study was intended to follow and extend a previous West Pearl Queen reservoir modeling study by Pawar et al. (2003). Pawar et al. (2003) used cross-well correlation to determine the structure of the Shattuck Sandstone. Figure 6 illustrates the cross-section transect used in Pawar et al. (2003) and in this study.

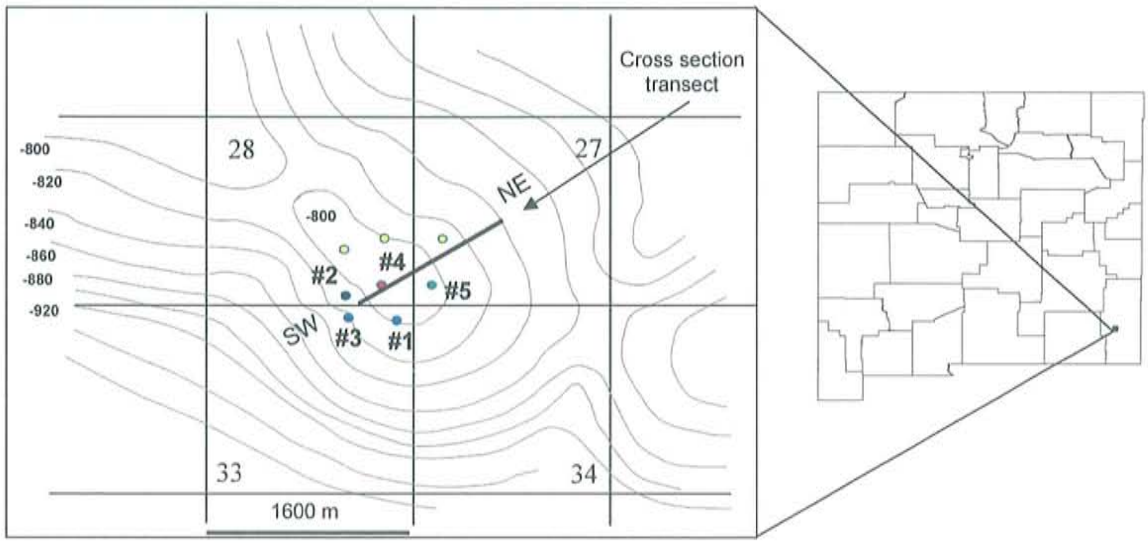

Figure 6: Cross-section transect location map. Contoured depth values are in feet relative to sea level. Large numerics (i.e. 33, 34) are township numbers. Figure adapted from Pawar et al., 2003.

The trend of the cross section is oriented southwest to northeast. Total length of the section is 1,500 meters. Two-dimensional grids of various resolutions (500, 1,000, and 6,000 grid blocks) were generated from digitized cross sections. A constant thickness of 12 meters for the Shattuck Sandstone was assumed for the entire section. Cartesian structured grids were generated in TOUGH2 to replicate the actual structure of the West Pearl Queen reservoir. Figure 7 shows an example of a 1,000 grid block TOUGH2 numerical mesh used in this study.

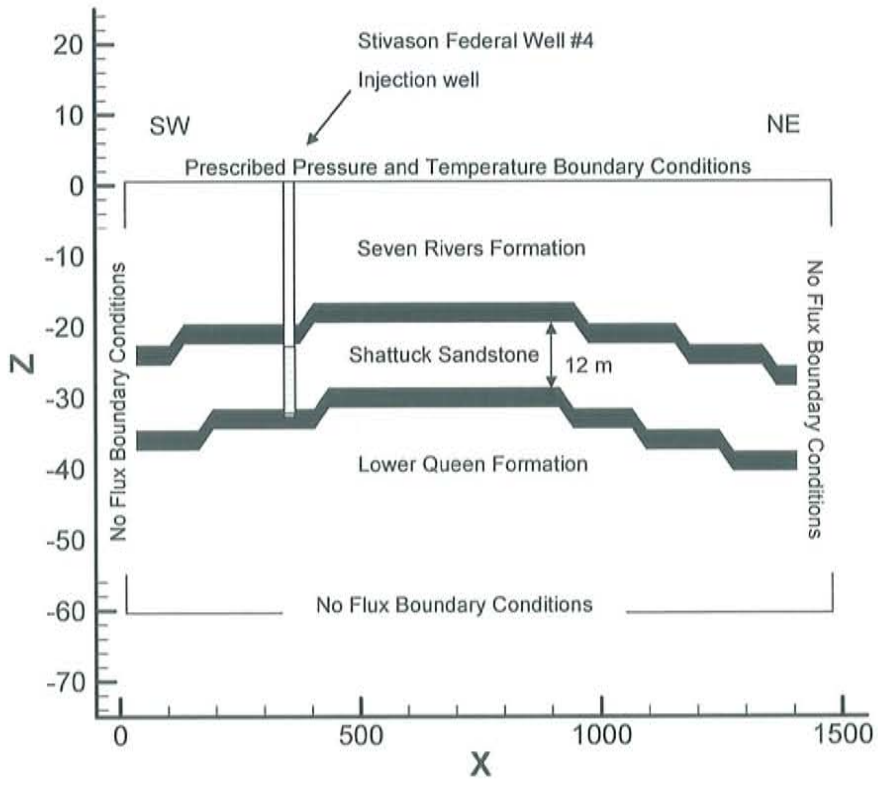

Figure 7: 1,000-grid block TOUGH2 numerical mesh and boundary conditions. Cross-section location is defined in the cross-section location map (Figure 6)

A series of simulations were completed with the 1000-grid block mesh. Homogeneous permeability values for the Shattuck Sandstone were varied for different simulations along with the Seven Rivers Formation and Lower Queen Formation. Permeabilities of the Seven Rivers Formation and the Lower Queen Formation were assigned the same value for convenience. The numerical mesh consisted of 1000 grid blocks, each with a volume of 2,250 m^3 (30m x 25m x 3m), divided into the Seven Rivers Formation, Shattuck Sandstone, and Lower Queen Formation (Figure 7). Dirichlet boundary cells were implemented by assignment boundary cells with very large volume (e.g., 1×10^{50} m^3). Prescribing a very large volume to a cell ensures that the thermodynamic variables within that cell remain unchanged throughout the course of the simulation. Injection of CO_2 in the center of the Shattuck Sandstone (Stivason Federal #4

well) was implemented at a horizontal distance of 375 meters from the southwest boundary of the domain. The top boundary elevation of the model was set equal to 1,371 meters below ground surface. This top boundary elevation corresponded to the actual depth of the West Pearl Queen reservoir. Dirichlet (pressure and temperature) and Neumann (prescribed flux) boundary conditions were applied for these case-study simulations as indicated in Figure 7.

Initial conditions for each simulation were obtained by steady-state, non-CO_2 injection simulations. Pressure and temperature in the top boundary cells were prescribed based on field observations within the Shattuck Sandstone (Pawar, personal communication, 2003). Simulations were run until the entire model domain attained steady-state conditions with pressure and temperature. The results for steady-state initial-condition simulations were then used as initial conditions for CO_2 injection simulations. Isothermal conditions were maintained throughout all CO_2 injection simulations. Initial pressure and temperature distributions (pre-CO_2 injection) are illustrated in Figures 8 and 9.

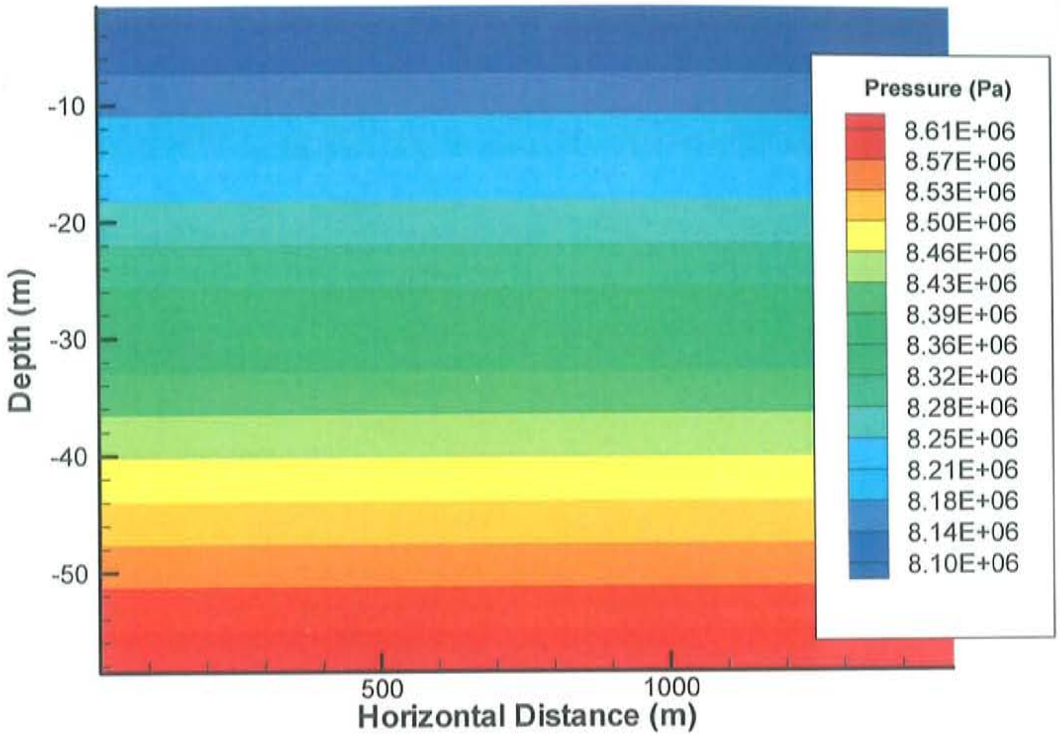

Figure 8: Initial pressure conditions

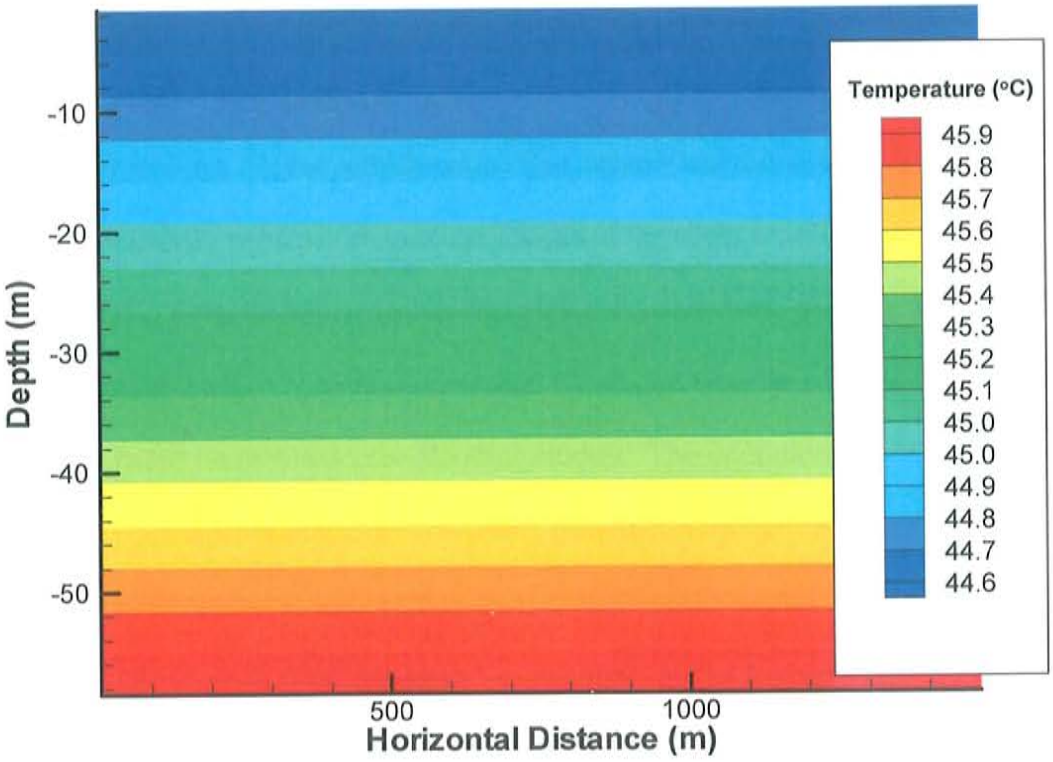

Figure 9: Initial temperature conditions

Rock parameters that were not varied between simulations are:

- Grain density
- Compressibility
- Expansivity
- Thermal conductivity
- Porosity
- Saturation capillary pressure and relative permeability functions

For each different unit (Seven Rivers Formation, Shattuck Sandstone, and Lower Queen Formation) a grain density of 2650 kg/m^3 was defined. Rock compressibility and expansivity were assumed negligible. Thermal conductivity values of all three units were set equal to 1.4 W/(m ^{o}C) for convenience. This value is a reasonable estimation for thermal conductivity values in sedimentary rocks of the upper crust (Ingebritsen and Sanford, 1998). Porosity values for the Shattuck Sandstone were set equal to 0.20, while values for the Seven Rivers and Lower Queen Formation were set equal to 0.15. These values were based on previous core-flooding studies. The saturation capillary pressure and relative permeability functions previously described were implemented.

The residence time of supercritical CO_2 in sedimentary basins is a function of overall geologic heterogeneity, pressure, temperature, and hydrodynamics. As the thermodynamic conditions of a reservoir approach the triple-point of the CO_2 phase diagram, residence times decrease. This decrease is due to the phase change from

supercritical CO_2 to gaseous CO_2. In the case of the West Pearl Queen reservoir, pressure and temperature are relatively well defined. As ambient flowrates within a reservoir increase, residence times of supercritical CO_2 decrease. Flow of undersaturated formation water into the vicinity of supercritical CO_2 induces interphase mass transfer between supercritical CO_2 and dissolved CO_2. This mass transfer effectively shortens the residence time of supercritical CO_2. The underpressured condition and subsequently no flow condition of the West Pearl Queen reservoir greatly increase the likelihood for longer residence times. Overall heterogeneity influences residence times to a greater degree. Sealing integrity of cap rock formations can greatly influence supercritical CO_2 residence times. Permeability values of injection intervals also influence residence times. To assess the time scales over which supercritical CO_2 might remain within the West Pearl Queen reservoir, the horizontal (k_h) and vertical (k_v) permeability assigned to the Seven Rivers/Lower Queen Formations and Shattuck Sandstone were varied between simulations. Table 2 summarizes the permeabilities used for each individual simulation. Homogeneity within each different unit was assumed.

	Shattuck Sandstone		Seven Rivers/Lower Queen	
Simulation	k_h (m^2)	k_v (m^2)	k_h (m^2)	k_v (m^2)
1	1×10^{-13}	1×10^{-14}	2×10^{-15}	2×10^{-17}
2	2×10^{-14}	2×10^{-15}	2×10^{-15}	2×10^{-17}
3	5×10^{-15}	5×10^{-16}	6×10^{-16}	2×10^{-17}
4	4×10^{-16}	2×10^{-17}	2×10^{-18}	2×10^{-19}

Table 2: Summary of horizontal (k_h) and vertical permeabilities (k_v) assigned to each unit of the model for each simulation

For each simulation, supercritical CO_2 is injected in the model through one injection node at a constant rate for 53 days the duration of the actual pilot test injection.

The total mass of supercritical CO_2 injected was approximately 2×10^6 kg of CO_2 which related to a constant CO_2 mass injection rate of 0.455 kg/s. Each simulation was run to a total time of 10,000 years. The simulation time-scale of 10,000 years was used based on maximum residence times found in the subsequent simulations. All simulations were performed on a UNIX-based platform with a Compaq digital Fortran 90 compiler. CO_2 mass balance errors within all simulations remained under 5 percent.

Results of the simulations completed include the distribution and extent of the supercritical CO_2 plume at various times, the residence time of supercritical CO_2 within the Shattuck Sandstone, the distribution of the dissolved CO_2 mass fraction through time, and the amount of CO_2 stored within solution (solubility trapping). The maximum horizontal extent of the supercritical CO_2 plume within the Shattuck Sandstone ranged from 260 meters (Table 2, Figure 10) to 433 meters (Table 2, Figure 11).

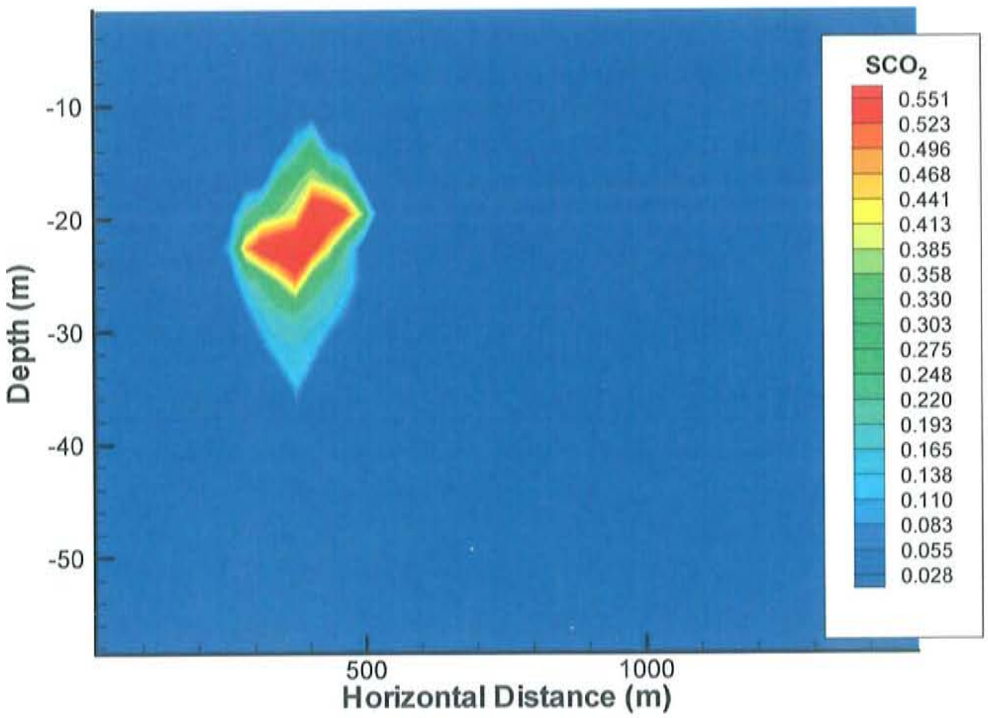

Figure 10: Minimum horizontal extent of supercritical CO_2 (simulation 3, 260 meters).

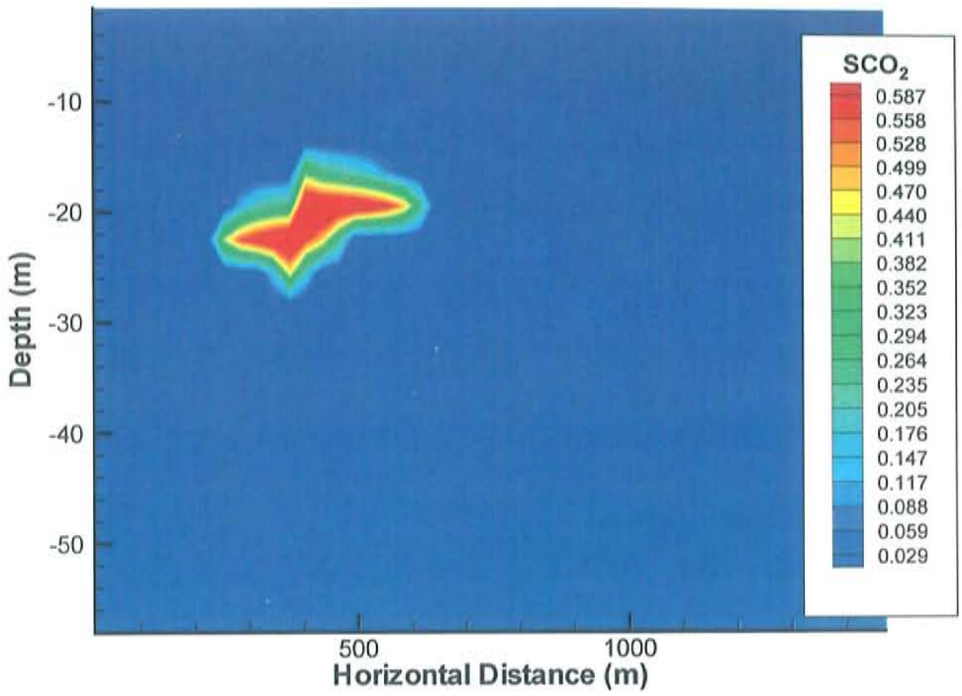

Figure 11: Maximum horizontal extent of supercritical CO_2 (simulation 1, 433 meters).

The residence time of supercritical CO_2 within the Shattuck Sandstone is clearly controlled by the vertical permeability of the overlying Seven Rivers Formation. Table 3 summarizes maximum horizontal extents and residence times of supercritical CO_2 plumes. Simulation 4 (Table 2) resulted in the greatest residence times for both the Shattuck Sandstone and the Seven Rivers Formation (Table 3).

Simulation	Shattuck Sandstone	Time (years)	Seven Rivers Formation	Time (years)
1	433 m	1	416	4
2	337 m	1	311 m	4
3	260 m	1	250 m	4
4	360 m	70	322 m	900

Table 3: Summary table of maximum horizontal extents and residence times of supercritical plumes for various simulations.

Residence times of the supercritical CO_2 plumes within the Seven Rivers vary from 4 years in simulation 1 to 900 years in simulation 4 (Table 3). Again, residence time is ultimately controlled by the vertical permeability within the Seven Rivers Formation.

The extent and residence time of the dissolved CO_2 phase in the proximity of the Shattuck Sandstone is important to determine the likelihood of reactions occurring within the reservoir. Gravity segregation of the denser CO_2-rich brine plays an important role in the transport of CO_2 within the reservoir. Brine density increases as the CO_2 mass fraction in the brine increases. The increases in brine density due to CO_2 mass fractions were less than 1 percent throughout all simulations. This slight increase in brine density caused CO_2-rich brine to migrate downward as depicted in Figures 12, 13 and 14.

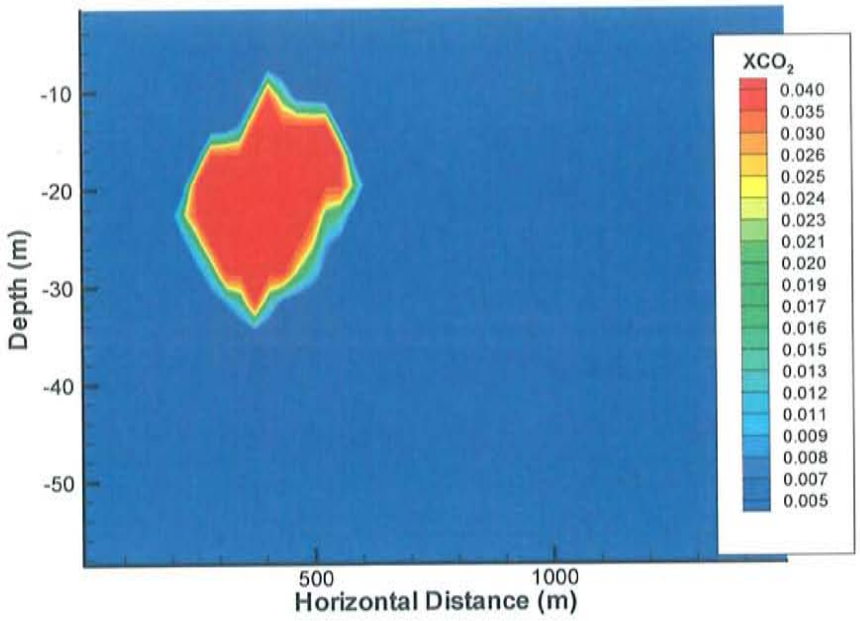

Figure 12: Mass fraction of dissolved-phase CO_2 after 2 years – Simulation 2

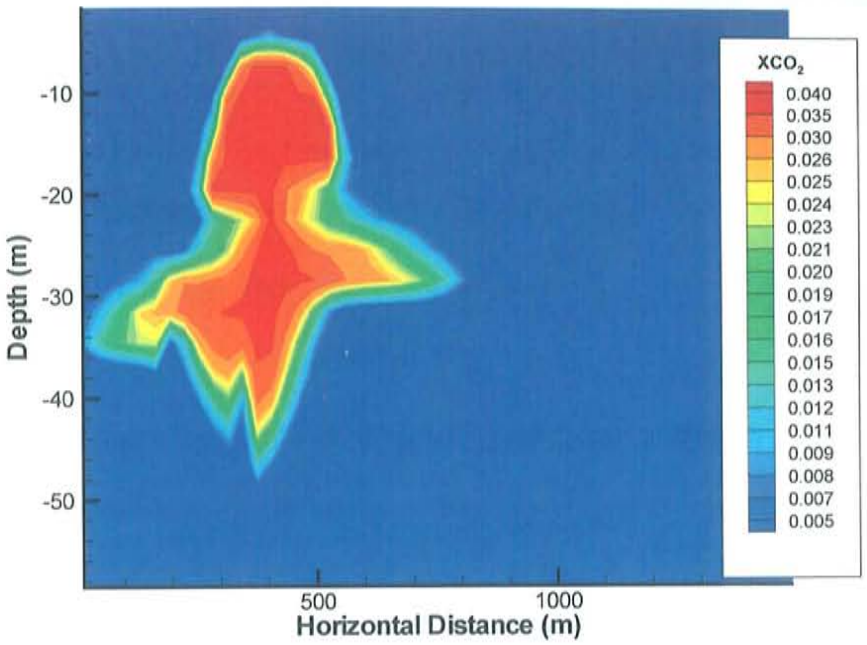

Figure 13: Mass fraction of dissolved-phase CO_2 after 900 years – Simulation 2

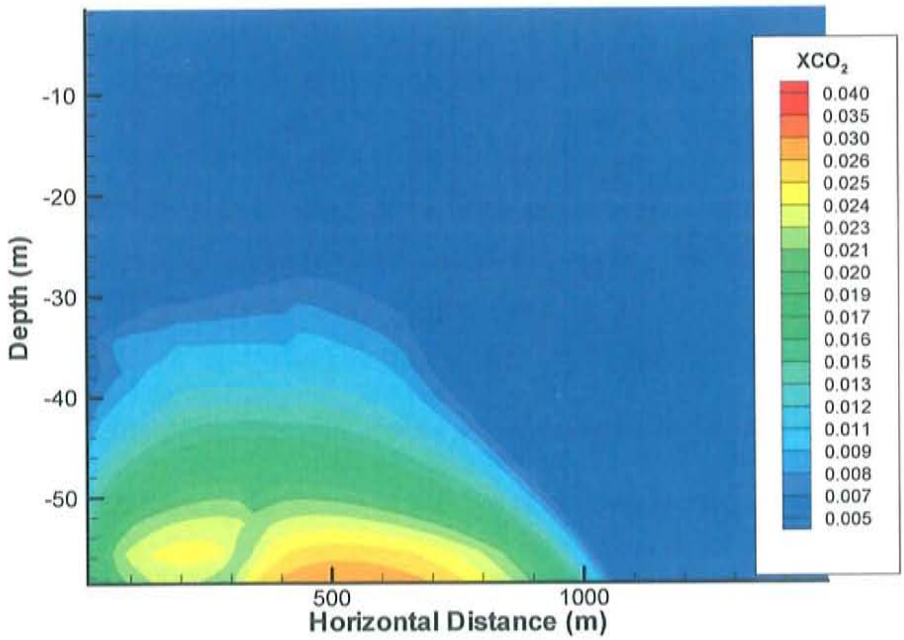

Figure 14: Mass fraction of dissolved-phase CO_2 after 10000 years – Simulation 2

Preferential downward migration is seen in some areas (Figure 13) at the interface between the Shattuck Sandstone and the Lower Queen Formation. This preferential migration can be attributed to permeability contrasts between the different units. A finer numerical mesh (6,000 grid blocks) was generated to examine if these effects were a product of the grid coarseness. Preferential migration was still observed within the higher-resolution mesh.

Residence times of increased dissolved CO_2 mass fractions within the Shattuck Sandstone are relatively long. Table 4 summarizes dissolved CO_2 residence times for the Shattuck Sandstone and the Seven Rivers Formation. Times vary from approximately 6,200 years in simulation 1 to 10,000 years in simulation 4 (Table 4).

	Shattuck Sandstone	Seven Rivers Formation
Simulation	Time (years)	Time (years)
1	6200	2000
2	9400	3000
3	9400	4000
4	10000	10000

Table 4: Residence times of dissolved CO_2 mass fractions in the Shattuck Sandstone and Seven Rivers Formation.

The main factor controlling dissolved CO_2 mass fraction residence times is the vertical permeability of the Shattuck Sandstone. Residence times of increased CO_2 dissolved mass fractions in the Seven Rivers Formation ranged from 2,000 years in simulation 1 to 10,000 years in simulation 4 (Table 4).

Simulation results suggest significant amounts of CO_2 can be stored as a dissolved phase. Over the simulation time period, separate-phase CO_2 is converted to dissolved CO_2, controlled by the CO_2 solubility of formation fluid. Because of solubility

limitations, CO_2 mass is predominantly represented by the separate-phase. At the end of injection, CO_2 starts to dissolve within the reservoir fluid, and continues to dissolve until maximum solubility is attained. Plots of total CO_2 mass partitioned among separate and dissolved phases as a function of time are illustrated in Figures 13 and 14. In simulations with lower permeabilities (simulation 4, Table 3, Figure 14), more CO_2 mass is stored within the separate-phase than in simulations with higher permeabilities (simulation 1, Table 3, Figure 13). The conversion of separate-phase CO_2 into the dissolved phase occurs rapidly in the higher-permeability case (2,000 years) compared to the low permeability case (> 10,000 years). With higher permeabilities, the separate-phase CO_2 plume migrates upward much faster, allowing for more interaction with fluid with low CO_2 concentration. This allows more CO_2 to dissolve in solution and thus decreases the amount of separate-phase CO_2 mass within the model domain.

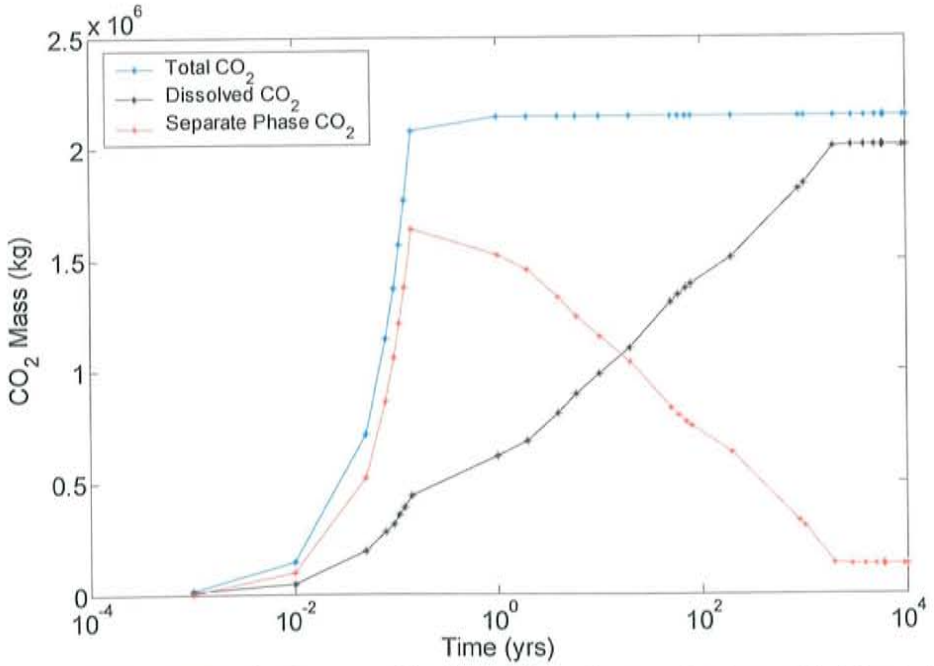

Figure 15: CO_2 mass partitioning between dissolved CO_2 and separate-phase CO_2 (simulation 1).

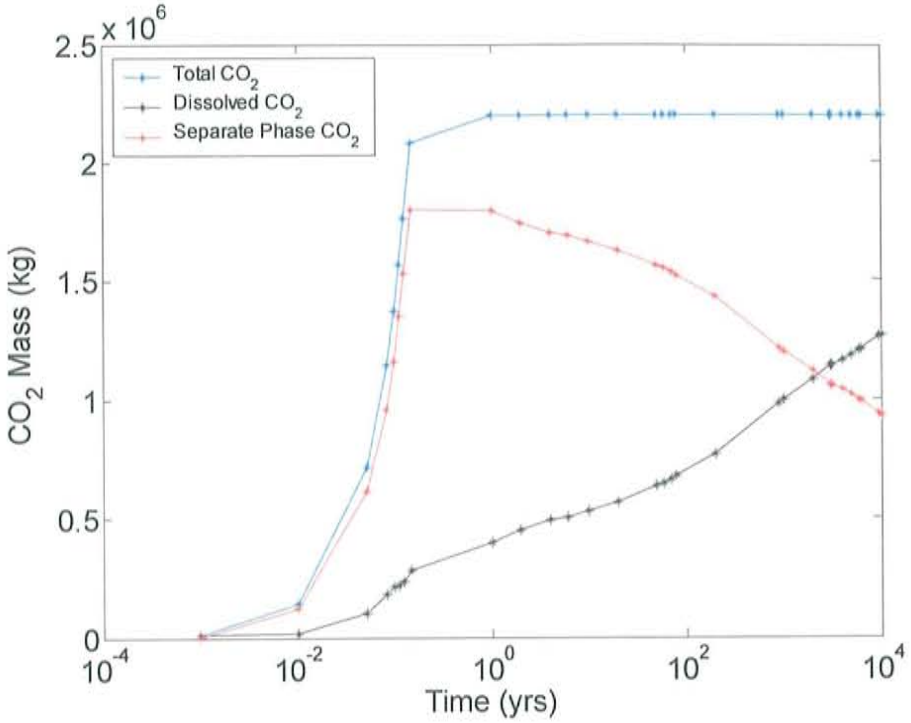

Figure 16: CO_2 mass partitioning between dissolved CO_2 and separate-phase CO_2 (simulation 4).

In summary, results of the TOUGH2-EOSCO2 modeling analyses show that the residence time of separate-phase CO_2 within the West Pearl Queen reservoir is controlled primarily by the vertical permeability within the Shattuck Sandstone and the Seven Rivers Formation. Residence times within the Shattuck Sandstone varied between 1 and 70 years while residence times within the Seven Rivers Formation ranged between 4 and 900 years. Significant solubility trapping (> 90 percent total CO_2 injected) is seen in simulations of higher permeability. Due to the underpressured nature of the West Pearl Queen reservoir, migration of separate-phase CO_2 is vertically-dominated. Downward migration of the dissolved CO_2 mass fraction occurs due to the greater density of CO_2-saturated waters compared to CO_2-poor waters.

These simulation results suggest that trapping of the separate-phase CO2 plume could occur within the West Pearl Queen reservoir in areas where the Seven Rivers vertical permeability is lower than 2 × 10-18 m2. Separate-phase CO2 residence times are in excess of 70 years in simulation 4 (Table 3). Geochemical modeling results suggest that dawsonite precipitation could decrease porosity by several percent in this time span. This porosity reduction would likely decrease permeability enough to enhance trapping of the separate-phase CO_2. However, timing of dawsonite precipitation is uncertain, mainly due to ambiguity in kinetic rate constants and specific surface parameters for various silicate minerals and dawsonite. Further studies should be conducted to constrain these uncertainties.

APPENDIX B:

FLOTRAN THEORETICAL FRAMEWORK

FLOTRAN SIMULATOR

The numerical reactive transport simulator FLOTRAN was developed by Peter Lichtner of Los Alamos National Laboratories in the mid 1990's (Lichtner, 2000). FLOTRAN simulates thermal, hydrologic, and chemical processes in variably saturated, nonisothermal, porous media. Simulations up to three (3D) spatial dimensions can be implemented. FLOTRAN can simulate multiphase systems including components of water and air along with multicomponent reactive chemical transport involving aqueous, gaseous and mineral species (Lichtner, 2000). Currently, an equation of state for CO_2 has not been implemented in the FLOTRAN simulator.

FLOTRAN applications include feasibility testing of Yucca Mountain, radionuclide contaminant transport processes at the Hanford site, and reactive transport processes within the Nevada Test Site (NTS). This study utilizes FLOTRAN, in conjunction with TOUGH2-EOSCO2, to predict important reactive transport processes related to the disposal of CO_2 within the subsurface. The following provides an overview of the version of FLOTRAN used in this study. The reader is referred to Lichtner et al. (1996) and Lichtner (2000) for a more detailed description of FLOTRAN.

FLOTRAN actually consists of two modules that when coupled sequentially can simulate reactive flow and transport of a multicomponent system. The FLOW module solves the mass and energy conservation equations for water and air while TRANS solves

mass conservation equations for multicomponent systems. TRANS considers the following types of reactions when calculating mass conservation for multicomponent systems.

- Homogeneous aqueous speciation reactions
    - Local equilibrium or kinetic based
- Heterogeneous gaseous speciation
    - Local equilibrium based
- Mineral precipitation/dissolution
    - Kinetic based
- Ion-exchange and sorption reactions
    - Local equilibrium

Aqueous speciation reactions can either be prescribed using kinetic reaction rates or through local equilibrium. Gaseous speciation and ion-exchange and sorption reactions are prescribed following local equilibrium only. Precipitation and dissolution reactions are purely kinetic based.

FLOW and TRANS each can be executed in standalone mode or together in coupled mode. The coupled transient mode sequentially couples the FLOW module to TRANS by passing flow velocities of liquid and gas phases, saturation, pressure, and temperature to TRANS after each iteration. TRANS then calculates porosity and permeability changes due to geochemical reactions and passes these variables to FLOW which then recalculates the flow field and primary variables. In steady-state mode, FLOW calculates the steady-state flow field and associated primary variables and passes the pertinent variables to TRANS (Lichtner, 2000).

FLOW MODULE

The module FLOW solves the mass and energy conservation equations for multiphase, nonisothermal conditions. The simplified system of single phase pure liquid is utilized for this study, but future modifications of FLOW will include a CO_2 equation of state. The equation of state for pure water allows for a temperature range of 1-1200 °C and pressures below 16.5 MPa. FLOW utilizes a fully implicit formulation similar to TOUGH2, using a variable substitution approach. For a single phase liquid, nonisothermal system, the three primary variables required are; p_l (pressure of liquid phase), X_a (mole fraction of air), and T temperature. Spatial discretization of the model domain is carried out essentially identical to that in TOUGH2 whereby an integrated finite difference scheme is utilized based on a block-centered grid (Lichtner, 2000).

The solution of mass and energy conservation equations at each grid block is obtained by using an incomplete factorization with an acceleration using GMRES (generalized minimum residual). This solver package was used throughout this study.

A multiphase version of Darcy's law utilizing pertinent relative permeability relationships is used and includes capillary, viscous, and gravity forces. In multiphase (air-water) systems, diffusion of air vapor is included. Energy transfer within FLOW can include heat conduction and convection.

Boundary conditions are implemented utilizing Dirichlet (constant primary variables) or Neumann (constant flux) type conditions. Neumann conditions are prescribed given a surface area of one side of the model domain. Dirichlet conditions are implemented using source/sink terms within the boundary cells.

TRANS MODULE

The reactive transport code TRANS solves multicomponent, multiphase, nonisothermal, reactive mass transport in multiple dimensions. Transport of both gas and liquid are possible including both advective and diffusive processes. Pure gas phase transport in not currently implemented.

Chemical species within TRANS can be partitioned among the aqueous, gaseous, or mineral phases. To account for mass transfer between each of these phases, TRANS assumes that a set of independent aqueous species can fully describe the chemical system (Wellman, 2002). TRANS implements a procedure in which mass action relations can be derived through conservation of mass. The implementation of this form requires the casting of chemical reactions in terms of different sets of species which include primary species and basis species. The number of primary species (N_p) is defined as the difference between the total number of species (N) and the number of reactions within the system (N_R):

$$N_p = N - N_R . \qquad \text{Eq. 1}$$

The prescribed primary species within a system must be represented within the aqueous phase. Gases and mineral species are defined within the secondary species. The reactions within TRANS for aqueous, gaseous, and mineral reactions can be written in the following form.

$$\sum_{j=1}^{N_c} \nu_{ji}^{l} A_j \rightleftharpoons A_i^{l} \ldots (i = 1, \ldots N_l),$$

$$\sum_{j=1}^{N_c} \nu_{ji}^{g} A_j \rightleftharpoons A_i^{g} \ldots (i = 1, \ldots N_g), \qquad \text{Eq. 2}$$

$$\sum_{j=1}^{N_c} \nu_{ji}^{m} A_j \rightleftharpoons M_i \ldots (i = 1, \ldots N_m),$$

where $\nu_{ji}^{l,g,m}$ is the stoichiometric reaction matrix which is defined as a matrix that denotes the number of moles of the jth primary species in one mole of secondary species. In other terms, it represents the stoichiometry between a certain primary species and its subsequent secondary species. A_i^{l}, A_i^{g}, M_i represent these subsequent secondary species (Wellman, 2002). Reacting minerals ($M_i \ldots (i = 1, \ldots N_m)$) are defined as heterogeneous reactions due to reactions taking place between mineral and aqueous species. Homogeneous reactions are defined as reactions that take place solely in the aqueous sense. The mass transport of these chemical species can be modeled using equilibrium reactions (mass action equations) or kinetic rate relationships. In both scenarios the chemical species are represented using the stoichiometric reaction coefficient ratio equations as presented (Eq. 2). The number of secondary species is equal to the sum of the total aqueous primary species, gaseous species (i.e. $CO_{2(g)}$, $O_{2(g)}$, etc.), and mineral species (Eq. 3).

$$N_{\text{sec}} = N_{aq} + N_g + N_{\text{min}} \qquad \text{Eq. 3}$$

MASS TRANSPORT EQUATIONS

Utilizing the above reaction formulation one can define mass transport equations based on the balance of solute flux entering and exiting the representative elemental volume (REV) along with the change in solute concentration within the REV and any

contributions from homogeneous and heterogeneous chemical reactions taking place within this volume (Lichtner, 1992). The general case of a liquid only transport system by advection, diffusion, and dispersion are considered in this case. Following the formulation of the mass transport equations presented by Lichtner (1985) the mass transport equation for multicomponent, multiphase system (solid-liquid) is:

$$\frac{\partial}{\partial t}(\phi C_j)+\frac{\partial J_j}{\partial x}=-\sum_{m=1}^{M}\nu_{ji}^{m}I_m-\sum_{i=1}^{N_{rev}}\nu_{ji}^{rev}I_i^{rev}, \qquad \text{Eq. 4}$$

for the *j*th primary species with concentration C_j, where ϕ is porosity, C_t is the total concentration for the *j*th primary species, J_j is the flux of the jth primary species, M is the total number of minerals reacting within the system, I_m is the reaction rate for the mth mineral, and ν_{ji}^{rev} is the matrix of stoichiometric reaction coefficients of the chemical reactions. Concentrations for aqueous complexes C_i^{rev} are calculated through mass action equations (Eq. 5).

$$C_i^{rev}=K_i\gamma_i^{-1}\prod_{j=1}^{N}(C_j\gamma_j)^{\nu_{ji}}, \qquad \text{Eq. 5}$$

where K_i is the specific equilibrium constant for the equilibrium reaction, γ_i, γ_j are the activity coefficients of the aqueous complexes (*i*) and primary species (*j*), respectively, N is the total number of reactions, and ν_{ji} is the stoichiometric reaction coefficient for the reaction in question. The change in volume fraction of reacting minerals can be described by a mass transfer equation,

$$\frac{\partial \phi_m}{\partial t}=\bar{V}_m I_m, \qquad \text{Eq. 6}$$

where ϕ_m is the volume fraction of the mth mineral in the system, $\overline{V}_m$ is the molar volume of the mth mineral, and I_m is the rate of the mth mineral reaction. The flux term within Equation 4 corresponds to the combined flux terms of advection, diffusion, and dispersion and is given by

$$J_j = -\phi D \frac{\partial C_j}{\partial x} + uC_j, \qquad \text{Eq. 7}$$

where D is the diffusion-dispersion coefficient and u denotes the Darcy fluid velocity. Considering a single-phase liquid system, the Darcy fluid velocity can be defined by Darcy's equation,

$$u = -\frac{k}{\mu_l} \nabla (p_l - \rho_l g z), \qquad \text{Eq. 8}$$

where k is the intrinsic permeability of the porous medium, μ_l is the dynamic viscosity of the liquid phase, p_l is the pressure of the liquid phase, ρ_l is the density of the liquid, g is the gravitational acceleration, and z is the vertical distance.

The effect of mineral precipitation on porosity can be examined through an equation that relates the total porosity of the system to the mineral volume fraction of all active minerals within the system.

$$\phi = 1 - \sum_{m=1}^{M} \phi_m \,, \qquad \text{Eq. 9}$$

where ϕ is the total porosity, M is the total number of reacting minerals within the system, and ϕ_m is the mineral volume fraction of the mth mineral. This relationship between the porosity of the system and the mineral volume fraction of the reacting minerals creates the bridge between the chemical and hydrologic regimes of this

inherently coupled system. After each time step, the porosity is updated over the domain and the mass transport equations and flux equations are then updated to represent the current total porosity of the system.

Mass action equations that describe mineral reactions are very similar to the aqueous reacting solute species, but concentration is not obtained through these equations because the activities of minerals are set equal to unity. Mineral mass action equations can be written as follows

$$K_m \prod_{j=1}^{M} (C_j \gamma_j)^{\nu_{jm}} = 1, \qquad \text{Eq. 10}$$

where K_m is the equilibrium constant for the heterogeneous mineral reaction m, M is the total number of heterogeneous mineral reactions, and ν_{jm} is the stoichiometric reaction coefficient for the mth mineral reaction. The previous equations presented (Eq. 4 to 10) are the necessary equations needed to fully describe the transport of solute species in a multicomponent reactive system.

CHEMICAL REACTIONS

The mass action equations presented within the previous sections can be utilized through the assumption of local equilibrium within the system. The assumption of local equilibrium is taken as a good assumption for most work performed on geochemical scenarios where the fluid and rock of a specified system are thought to be in thermodynamic equilibrium. Lichtner et al. (1996) describes local equilibrium as the state at which the kinetic rate constant approaches infinity within a system that is open allowing for transport of matter across the boundaries of the system. Using the assumption of local equilibrium and the mass action equations along with all of the

thermodynamic information stored within databases, allows for the full representation of chemical reactions through equilibrium chemistry. TRANS houses two databases, one that encompasses equilibrium constants at 25 °C and one that houses equilibrium constants at various temperatures particularly from 0 °C to 300 °C. These thermodynamic databases are founded from the EQ3/6 database by Wolery (1983). TRANS uses a Mayer-Kelly function to interpolate between temperatures given by

$$\log K(T) = \frac{a_2}{T^2} + \frac{a_1}{T} + a_o \ln T + a_1 + a_2 T, \qquad \text{Eq. 11}$$

where a_1 and a_2 are constants and T is the temperature (°C). Activity coefficients that enter the previous equations ($\gamma_{i,j}$) are calculated using the extended Debye-Huckel formulation

$$\ln \gamma_{i,j} = -\frac{z_{i,j}^2 A\sqrt{I}}{1 + Ba_{i,j}\sqrt{I}} + bI, \qquad \text{Eq. 12}$$

where z is the ionic charge on the particular species, I is the ionic strength of the solution, and A, B, $a_{i,j}$, b, are constants inherent within the formulation. Using the extended Debye-Huckel equation, equilibrium constants at specified temperatures, and the mass action equations give the necessary fundamental equations needed so that concentrations can be defined for aqueous species in solution.

CHEMICAL KINETICS

Solving the transport equations presented earlier in this section requires knowledge pertaining to the reaction rates for kinetically controlled reactions, specifically both homogeneous reactions and heterogeneous reactions. Following the formulation devised by Lichtner et al. (1996), kinetic expressions of both homogeneous and

heterogeneous reactions are presented here. Homogeneous reactions involving only aqueous species require that the reaction rate I_i^{rev} be obtained. The rate of a kinetic homogeneous reaction is given by the difference between the forward and backward reaction rates,

$$I_i^{rev} = k_i^f \prod_{\nu_{ir} \le 0} (\gamma_i C_i)^{-\nu_{ir}} - k_i^b \prod_{\nu_{ir} \ge 0} (\gamma_i C_i)^{\nu_{ir}}, \qquad \text{Eq. 13}$$

where $k_i^{f,b}$ are the forward and backward rate constants for the reversible reaction. As the system reaches equilibrium the equilibrium constant for the reaction (K_i) and the kinetic rate constants ($k_i^{f,b}$) are related by

$$K_i = \frac{k_i^f}{k_i^b} = Q_i, \qquad \text{Eq. 14}$$

where Q_i denotes the ion activity product and can be defined by

$$Q_i = \prod_{i=1}^{N} (\gamma_i C_i)^{\nu_{ir}}. \qquad \text{Eq. 15}$$

Heterogeneous reactions can be described by considering the following. A solid phase (mineral) interacts with an aqueous phase solution according to

$$\sum_{j=1}^{N_c} \nu_{jm} A_j \rightleftharpoons A_{\min}, \qquad \text{Eq. 16}$$

where ν_{jm} is the stoichiometric reaction coefficient for the reaction, A_j is the jth aqueous species, and $A_{\min}$ is the solid mineral phase of the reaction. The reaction rate corresponding to the above reaction can be formulated by

$$I_m = -k_m s_m \left[\prod_i (\gamma_i C_i)^{n_i} \right] (1 - e^{-A_m / RT}),$$
$$= -k_m s_m \left[\prod_i (\gamma_i C_i)^{n_i} \right] (1 - K_m Q_m), \qquad \text{Eq. 17}$$

where k_m is the kinetic rate constant, s_m is the specific mineral surface area, and n_i is a constant. A_m is defined as the affinity of the reaction and can be calculated by

$$A_m = -RT \ln K_m Q_m, \qquad \text{Eq. 18}$$

where R is the gas constant, T is the temperature, K_m is the equilibrium constant for the heterogeneous reaction, and Q_m is the ion activity product for the reaction. The affinity factor, A_m, is a measure of how far from equilibrium the system is with respect to the specific reaction. The relationship between the affinity factor, A_m, and the reaction rate, I_m, can be summarized by the following relationships:

If $A_m > 0$ then $I_m < 0$

If $A_m < 0$ then $I_m > 0$

If $I_m < 0$ then dissolution occurs

If $I_m > 0$ then precipitation occurs

If a specific mineral is not present A_m is zero

Rate expressions are defined utilizing this formulation for each actively prescribed mineral within the system.

The solution to the transport equations within the previous section is obtained using very similar techniques as those in TOUGH2. TRANS implements an integral finite volume scheme to discretize the spatial domain and implements various solution

algorithms to obtain a numerical approximation to the system of non-linear partial differential equations that describe the transport of chemical mass. Solution algorithms available within TRANS include:

- Implicit
- Explicit
- Operator-splitting

Two different solvers are available within TRANS, including a tri-diagonal solver and the conjugate gradient solver WATSOLV (Van der Kwaak et al., 1995). The operator-splitting algorithm is used for larger problems, specifically large 2D and 3D problems, while the implicit finite difference algorithm is sufficient for 1D and small 2D problems (Lichtner, 2000).

In summary, TRANS solves multicomponent-multiphase, non-isothermal, reactive mass transport equations for multiple dimensions. In this study TRANS is utilized to simulate mineralization and dissolution of reactive mineral phases and solute transport related to CO_2-rich brine occurring in CO_2 injection scenarios.